

Dissertation
submitted to the
Combined Faculties for the Natural Sciences and for Mathematics
of the Ruperto-Carola University of Heidelberg, Germany
for the degree of
Doctor of Natural Sciences

presented by
Manas Mukherjee, MSc
born in: Durgapur, India
Oral examination: 15.12.2004

The mass of ^{22}Mg
and
a concept for a novel laser ion source trap

Referees:

Prof. Dr. H.-Jürgen Kluge

Prof. Dr. Andreas Wolf

The mass of ^{22}Mg and a concept for a novel laser ion source trap:

Clean and high-quality radioactive ion beams can be prepared by combining ion trap and resonance laser ionization techniques. A feasibility study for such a laser ion source trap has been carried out which shows enormous improvement in the beam emittance, purity, and in addition allows for a variation of the ion beam time structure.

Direct high-precision mass measurements around mass number $A = 22$ are of utmost importance. First, the masses of the superallowed β -emitter ^{22}Mg and its daughter ^{22}Na are needed to test the conserved-vector-current (CVC) hypothesis and the Cabibbo-Kobayashi-Maskawa (CKM) matrix unitarity, both being predictions of the Standard Model. Second, to calculate the reaction rate of $^{21}\text{Na}(p, \gamma)^{22}\text{Mg}$ the involved masses are required very accurately. This rate is needed in order to extract an upper limit on the amount of a characteristic γ -radiation emitted from classical nova bursts which has been searched for but not yet detected. At the triple trap mass spectrometer ISOLTRAP at ISOLDE/CERN, the masses of ^{21}Na , ^{22}Na , and ^{22}Mg have been measured with relative uncertainties of better than 1.5×10^{-8} . This solved a conflict between two available mass values for ^{22}Mg . The mass measurements as well as their impact are discussed. In addition a vivid description of the present ISOLTRAP setup along with the standard experimental procedure is described. Special emphasis has been made on the development of a carbon cluster ion source for absolute mass measurements at ISOLTRAP.

Die Masse von ^{22}Mg und ein Konzept für eine neuartige Laser-Ionenquelle:

Reine radioaktive Ionenstrahlen mit hoher Strahlqualität können präpariert werden, indem man Ionenfallen mit der Laser-Resonanzionisationstechnik kombiniert. Eine Machbarkeitsstudie für eine solche Laser-Ionenfallenquelle, die eine deutliche Verbesserung der Emittanz und darüber hinaus eine variable zeitstruktur des Ionenstrahls ermöglicht, wurde durchgeführt.

Direkte, hochpräzise Massenmessungen um die Massenzahl $A = 22$ sind von besonderem Interesse: Erstens wird die Masse des übererlaubten β -Emitters ^{22}Mg und seiner Tochter ^{22}Na zum Test der Vectorstromerhaltungs (CVC)-Hypothese und der Unitarität der Quarkmischungsmatrix (CKM) - beides Vorhersagen des Standardmodells - benötigt. Zweitens sind die Massenwerte wichtige Parameter, um die Reaktionsrate $^{21}\text{Na}(p, \gamma)^{22}\text{Mg}$ zu berechnen. Diese Rate wird benötigt, um eine obere Grenze für die charakteristische γ -Strahlung, die in klassischen Nova-Bursts emittiert wird, zu extrahieren. Diese Strahlung wurde zwar gesucht, aber bisher noch nicht beobachtet. Mit dem Dreifallen-Massenspektrometer ISOLTRAP wurden die Massen von ^{21}Na , ^{22}Na , und ^{22}Mg mit einer relativen Massengenauigkeit von besser als $1,5 \times 10^{-8}$ gemessen. Dies löste einen Konflikt zweier vorhandener Massenwerte für ^{22}Mg . Die Massenmessungen und ihre Konsequenzen werden vorgestellt. Ein besonderes Augenmerk wurde auf die Entwicklung einer Kohlenstoff-Cluster-Laserionenquelle für absolute Massenmessungen bei ISOLTRAP gelegt.

Contents

1	Introduction	1
2	Complimentary techniques for the production and separation of radionuclides	3
2.1	The in-flight separation technique	3
2.1.1	The SHIP technique	4
2.1.2	The Fragment Separator technique	5
2.2	The isotope separator on-line (ISOL) technique	5
2.2.1	The laser ion source trap	7
	Principle of a laser ion source trap	8
	Simulation studies and the RFQ trap design	10
	Efficiency estimation	14
	Radial and longitudinal cooling	15
	Beam extraction and emittance	16
2.3	Other techniques	17
3	The triple trap mass spectrometer ISOLTRAP	19
3.1	Principles of the ISOLTRAP mass spectrometer	21
3.1.1	An RFQ trap for cooling and bunching	22
	Buffer gas cooling	25
3.1.2	Ideal Penning trap	26
3.1.3	Real Penning trap	29
	Electric field imperfections	29
	Misalignment	30
	Magnetic field instabilities and imperfections	30
	Storage of more than one ion	32
3.1.4	Excitation of the ion motion and the cyclotron resonance de- tection technique	32
	Dipolar excitation	33
	Quadrupolar excitation	34

	Viscous damping in a Penning trap	35
	Mass-selective buffer gas centering	37
	Time-of-flight ion cyclotron resonance technique	37
3.2	Experimental setup of ISOLTRAP	39
3.2.1	Production of radioactive beams at ISOLDE	40
3.2.2	ISOLTRAP RFQ cooler and buncher	43
3.2.3	Ion transport between the RFQ cooler and buncher and the Purification Penning Trap	44
3.2.4	The Purification Penning Trap	45
	Space charge effect	46
3.2.5	The mass spectrometer section	48
	Ion transfer section between the two Penning traps	50
	The Precision Penning Trap	51
	The time-of-flight drift section	52
3.2.6	Off-line ion sources	54
	Surface ion source	54
	Previously used carbon cluster ions source	55
	Present carbon cluster ion source	56
3.2.7	The beam diagnostic system	58
3.2.8	Control system	60
3.3	Experimental mass measurement procedure at ISOLTRAP	61
3.3.1	Time sequence for single measurement cycle	61
3.3.2	Cleaning processes	63
3.3.3	Magnetron phase lock mechanism	63
3.3.4	Tuning of the trap parameters	66
	Capture timing to the Precision Trap	66
	Magnetic-field optimization	67
	Electric-field optimization	68
3.4	Determination of the systematic uncertainty and data analysis	69
3.4.1	Determination of the systematic uncertainty	70
3.4.2	ISOLTRAP's standard analysis procedure	72
3.5	Performance of the ISOLTRAP spectrometer	74
3.5.1	Absolute mass measurements	75
3.5.2	Accuracy	75
3.5.3	Efficiency	75
3.5.4	Half-life	76
3.5.5	Resolving power	76
3.5.6	Applicability	79

4	Mass evaluation around $A = 22$	81
4.1	General theory	83
4.1.1	Consistency of data	85
4.1.2	Applicability to our data	85
4.2	The mass evaluation	86
4.2.1	Least-squares adjustment results	87
4.2.2	Discussion	89
4.3	Physics implication	91
4.3.1	Contribution to test the CVC hypothesis	91
4.3.2	Present status of the CKM unitarity	93
4.3.3	Contribution to nuclear-astrophysics	95
5	Conclusions	99

List of Figures

2.1	Production of radioactive atoms.	4
2.2	Layout of the SHIP facility at GSI/Darmstadt.	5
2.3	Layout of the fragment separator at GSI/Darmstadt.	6
2.4	Schematic of a surface ion source.	6
2.5	Periodic table of elements	7
2.6	Yield of the rare earth elements using a surface ion source.	8
2.7	Schematic of a typical LIST setup.	9
2.8	The LIST RFQ trap and associated ion-optics	11
2.9	Probability of an atom within laser illuminated volume	13
2.10	Radial ion distribution in the LIST cooler and buncher	14
2.11	Radial and longitudinal cooling time	15
2.12	Emittance ellipse of the extracted ion bunch	16
2.13	Types of isotope separator on-line	17
2.14	Generic IGISOL setup	18
3.1	Overview of the ISOLTRAP setup	22
3.2	Principle of an RFQ cooler and buncher	23
3.3	Stability diagram for an RFQ trap	24
3.4	Buffer gas cooling in an RFQ trap	25
3.5	Penning trap configurations	26
3.6	Eigen motions in a Penning trap	28
3.7	Magnetic-field drift over with time	31
3.8	Configurations for applying azimuthal RF excitation	33
3.9	The effect of azimuthal quadrupolar RF excitation	35
3.10	Buffer gas centering in a Penning trap	37
3.11	Principle of TOF ICR	38
3.12	Radial energy gain and theoretical line shape for a TOF-ICR	39
3.13	Photo of the ISOLTRAP setup	40
3.14	The layout of the ISOLTRAP setup	41
3.15	The beam lines at ISOLDE hall	42

3.16	A Photograph of the RFQ cooler and buncher	42
3.17	The deceleration electrode of the RFQ cooler and buncher	43
3.18	The principle of a pulsed cavity	45
3.19	The Purification Penning Trap	46
3.20	Space charge effects in the Purification Trap	48
3.21	The spectrometer section	49
3.22	The Precision Penning Trap	51
3.23	The electric potential and magnetic field in the TOF section	53
3.24	Design of the combined ion source	55
3.25	Different components of the cluster laser ion source.	56
3.26	Incident angle vs absorbed energy	56
3.27	Sketches of the previous and present cluster laser ion source.	57
3.28	Time-of-flight signal of different carbon cluster fragments	58
3.29	New channeltron detector design.	59
3.30	Layout of the control system.	60
3.31	The time pattern for a measurement cycle	62
3.32	Magnetron phase lock mechanism scheme	64
3.33	Theoretical plots for magnetron phase lock mechanism	64
3.34	TOF resonances for different magnetron phases	66
3.35	Trapped ion counts vs delay time	67
3.36	Magnetic field optimization	68
3.37	Electric field optimization	69
3.38	Mass dependent systematic uncertainty	70
3.39	B-field dependent systematic uncertainty	71
3.40	Residual systematic uncertainty	71
3.41	^{22}Mg TOF resonance	73
3.42	$^{22}\text{Na}^+$ z-class analysis	74
3.43	^{68}Cu low-lying nuclear level scheme	76
3.44	Isomeric state resolution of ^{68}Cu	77
3.45	In-trap decay spectroscopy	78
4.1	Z-class analysis for $^{22}\text{Mg}^+$	82
4.2	AME mass excesses as compared to the ISOLTRAP values	88
4.3	Comparison of the mass excesses of ^{22}Mg from different groups	89
4.4	Information flow diagram	90
4.5	Comparative Ft -values	92
4.6	CKM unitarity	95
4.7	Hot & cold reaction paths	96

List of Tables

2.1	Parameters for the LIST RFQ trap	12
3.1	Typical parameters for the RFQ cooler and buncher of ISOLTRAP .	43
3.2	Performance of the ISOLTRAP RFQ cooler and buncher	44
3.3	Typical parameters for the Purification Trap of ISOLTRAP	47
3.4	Typical parameters for the Precision Trap of ISOLTRAP	52
3.5	Magnetic susceptibilities of trap materials	52
3.6	Parameters for the ISOLTRAP time-of-flight section	53
4.1	Production characteristics of the radioactive nuclides	81
4.2	Input parameters for mass evaluation by least-squares analysis	83
4.3	Outcome of the least-squares analysis	88
4.4	Overview of CKM unitarity	95

Chapter 1

Introduction

According to our present knowledge of the universe, nature exhibits its forces in four different forms. In descending order of their strengths, they are namely, the strong, the electromagnetic, the weak, and the gravitational interactions. The ultimate quest in physics is to find one theory to describe all four interactions among the fundamental particles. Till date, only the strong and the weak interactions can be described by what is known as the “Standard Model” of particle physics. The Standard Model predictions have so far being tested in many different experiments in diverse fields of physics. Still there are avenues where it needs to be tested. Specially because it failed to explain some fundamental questions like the origin of mass for the fundamental particles like quarks.

In addition, our understanding about the very origin of the universe and its existence is rather poor. Questions like: Why is matter more than antimatter? What are dark matter and dark energy? How are the elements formed?, are still unanswered. These questions are closely related to our understanding of the interactions among the basic building blocks of our universe. Of particular interest here is the question of nucleosynthesis, a main research field in nuclear astrophysics. Important parameters to answer these fundamental questions are the masses of short-lived radionuclides.

The strong and the electroweak interactions decide over the stability of a compound system like a nucleus formed out of neutrons and protons which are in turn made of three generations of quarks and leptons as prescribed by the Standard Model. The electromagnetic interaction is mediated by photons, strong interaction by gluons and weak interaction by W^- and Z -bosons. To form a nucleus out of neutrons and protons a part of the total mass of the constituents converts to energy and is lost from the system. This is known as the binding energy. Thus, the binding energy of a nucleus reveals the nature of the interactions responsible for binding the constituents together. For an β -unstable nuclide, the released energy during the decay throws light on the nature of the weak interaction which is responsible for such decays.

The binding energy of a nuclide can be derived by measuring the mass of it since proton and neutron masses are very precisely known. Similarly, decay energies and reaction Q -values can be derived from the measured masses of the participat-

ing nuclides. To perform any test of the Standard Model it is required to measure the mass differences with extremely high precision ($\sim 10^{-8}$) since the effects are very small compared to the measured masses which are in the order of about $100 \text{ GeV}/c^2$. The tests of the Standard Model predictions, where high-precision mass measurements on radioactive nuclides can contribute to, are the conserved-vector-current (CVC) hypothesis and the Cabibbo-Kobayashi-Maskawa (CKM) matrix unitarity [Har2003]. For the CVC hypothesis tests the required derived parameter is the so called ft -value for superallowed nuclear β decays. The corrected statistical rate factor F depends on the Q value for these decays and hence on the mass differences. The up-down quark mixing element of the CKM matrix is dependent on the universal Ft value derived from all the superallowed β decays. So the unitarity of this matrix is dependent on the measured mass differences of the participating nuclides.

The ISOLTRAP experiment situated at ISOLDE, CERN is dedicated to perform mass measurements on radioactive nuclides which are produced by the ISOLDE facility. Over the years there has been continuous development to push the limits of the accuracy further down and to increase the overall efficiency so as to access very exotic or shorter-lived nuclides. All along this developmental path new techniques have emerged which now find application in other fields, like radioactive ion beam preparation. One example is the installation of a buffer-gas-filled linear radiofrequency quadrupole trap [Her2001] now known as RFQ cooler and buncher which boosted the efficiency and also improved the emittance of the radioactive beam at ISOLTRAP. Such a device can also be used at the target-ion source system of ISOLDE along with stepwise laser ionization in order to produce high purity radioactive beams with low emittance which will help many present experiments that suffer badly from contaminations.

The major part of the work presented here concerns the mass measurements performed on the radionuclides $^{22}\text{Mg}^+$ and its β -decayed daughter nuclide $^{22}\text{Na}^+$ which facilitate the test of the CVC hypothesis and the CKM matrix unitarity. In addition, the mass of ^{21}Na was measured which along with the mass of ^{22}Mg provide the reaction Q -value for the $^{21}\text{Na}(p, \gamma)^{22}\text{Mg}$ reaction. This measurement has implication in the understanding of nucleosynthesis in classical nova bursts [Bis2003].

Chapter 2 describes and compares different possibilities for the production of radioactive nuclides. Special emphasis is made here on the description and the feasibility study of a Laser Ion Source Trap (LIST) that will provide high-purity and low-emittance radioactive beams. A thorough description of the ISOLTRAP setup, consolidating all its development over the last five years is given in Chapter 3. It includes description of the experimental principles, individual components, experimental procedure, data analysis, and systematic uncertainty determination. Chapter 4 explains the measurements performed in the low mass region around mass number $A = 22$. The adopted mass evaluation procedure and its outcome are vividly described in this chapter along with their twofold physics implications. The present status of the CVC hypothesis and the CKM unitarity tests in view of our results forms one part while the contribution towards the understanding of nucleosynthesis in classical nova forms another part of it.

Chapter 2

Complimentary techniques for the production and separation of radionuclides

Radioactive ion beams of energies ranging from a few 10 keV to the relativistic regime are produced at different radioactive ion beam facilities. Heavy-ion central collision, near the energy of the Coulomb barrier, results in fusion and is the mechanism for the production of heavy, super-heavy, and neutron-deficient medium-mass nuclides at GSI [Hof2000], JINR [Org2004], RIKEN [Mor2003a], ANL [Dav1992] etc.. At energies above the Fermi domain, projectile fragmentation is the tool for the production of exotic nuclei over the entire periodic table up to the heaviest projectile available as it is done at GSI [Gei1992], MSU [Mor2003b], RIKEN [Kub1992]. Medium-mass neutron-rich nuclei can also be produced by neutron, energetic-proton, or heavy-ion induced fission for example at ISOLDE [Kug2000], TRIUMF etc.. Figure 2.1 summarizes the nuclear reactions for the production of radionuclides. In the following, three major techniques for the separation of radionuclides will be discussed. A feasibility study done within this work on a new type of ion source related to the on-line isotope separators will be discussed in greater details. Complementarity of these techniques is obvious as the separation method is associated with the production mechanism.

2.1 The in-flight separation technique

The heavy-ion fusion reactions, leading to the production of the heavy and super-heavy elements (SHE), the projectile fragmentation forming products up to the heaviest projectile available, and the heavy-ion fission, resulting in the neutron-rich medium-heavy nuclides, are the nuclear reactions where in-flight separation technique is the tool to perform the separation of the reaction products. For the first case, the products are separated according to their velocities by magnetic and electric fields. Such a Wien filter is in use for over three decades now, for the search and production of the super-heavy elements at GSI/Darmstadt called SHIP (Separator

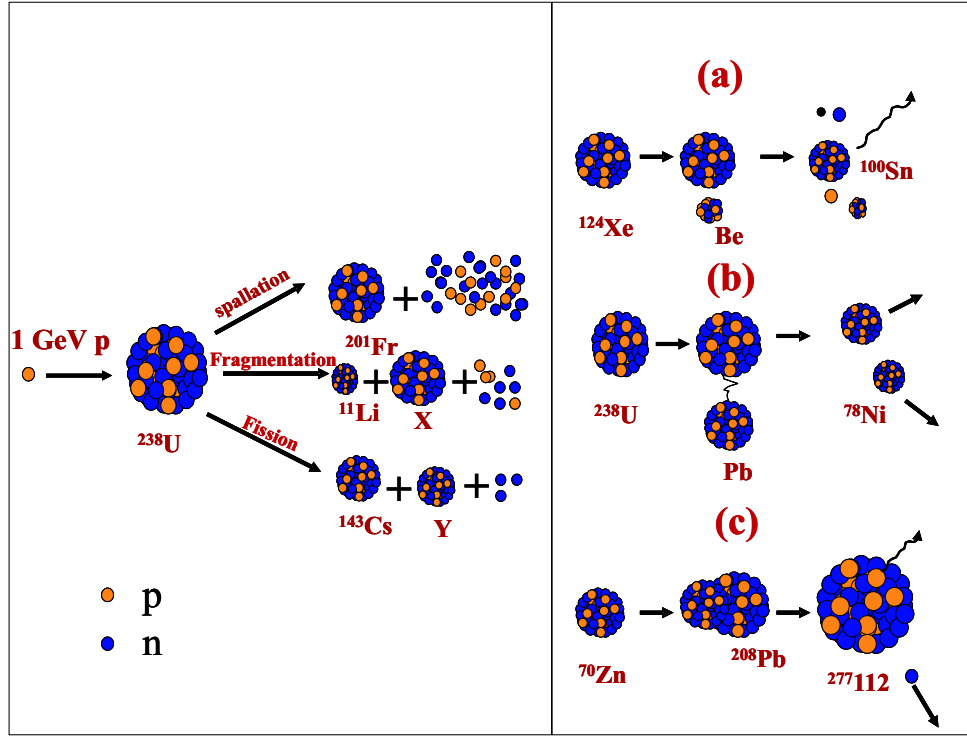


Figure 2.1: Diagram of (left) the proton induced reactions, and (right) the heavy-ion induced (a) fragmentation, (b) Coulomb dissociation, and (c) fusion reactions.

Heavy Ion Reaction Products). Other types of in-flight separators are operated, for example, at Berkeley/California and at Dubna/Russia. Reaction products at relativistic energies are isotopically separated by magnetic dipoles. An example is the FRS (FRagment Separator) at GSI which is relatively new but has been very successful in exploring nuclides far from the valley of stability which were not accessible by other techniques. A vivid review of the SHIP separator along with its developmental history can be found in [Hof2000]. The FRS technique is reviewed in [Gei1992] and [Mün1992]. Here, only the basic concepts of the above two techniques will be discussed with the SHIP and the FRS at GSI-Darmstadt as examples.

2.1.1 The SHIP technique

Ion beams at an energy of 5-7 MeV/u ranging from $u=50$ to $u=150$ impinge on a thin target ($\sim 1 \text{ mg/cm}^2$) to undergo fusion evaporation reactions forming a compound nuclei which recoils out of the target while evaporating a few neutrons. The limitation in the target thickness arises from the energy loss of the ion beam in the target, which results (using thicker targets) in an energy distribution that is too wide for either the production of the fusion products or their in-flight separation. The products with energies of a few 100 keV/u are then focused by magnetic quadrupole

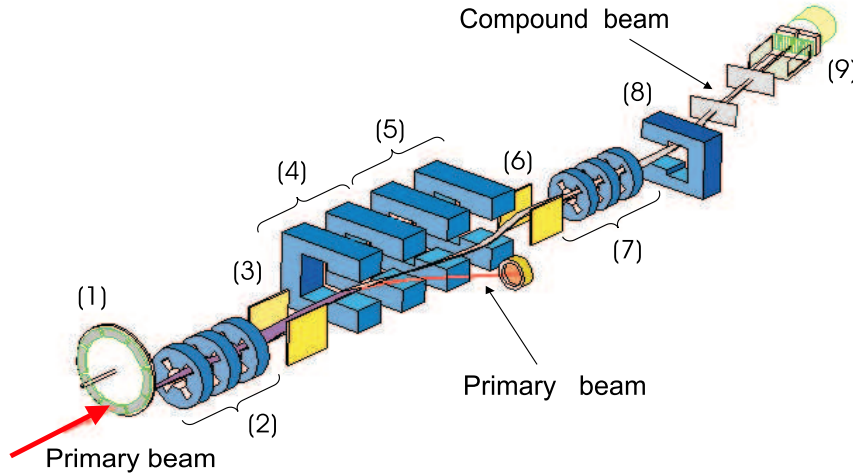


Figure 2.2: Layout of the Separator Heavy Ion reaction Product facility used for the production of the heavy and super-heavy elements situated at GSI, Darmstadt. The components are (1) the rotatable target wheel, (2,7) the magnetic quadrupoles for beam focusing, (3,6) electric dipoles, (4,5) pairs of magnetic dipoles, (8) the final magnetic dipole separator, and (9) a detector setup. (3,4) and (5,6) form two pairs of Wien filter or velocity filter as explained in the text.

triplets and are separated from the primary beam by a combination of magnetic and electric dipole pairs as shown in Figure 2.2. Ions belonging to only one velocity class are selected by the SHIP filter which in turn depends on the reaction channel one is interested in.

2.1.2 The Fragment Separator technique

Figure 2.3 shows the lay-out of the FRS at GSI serving as example for the fragment separator technique. The relativistic heavy ions up to uranium, delivered by the heavy-ion synchrotron SIS18, are impinged on a target “Ta” to produce projectile fragments or fission fragments almost at the same energy as that of the primary beam. These fragments are then separated as shown in Figure 2.3 by two dipole magnets placed before the focal planes F1 and F2 according to their mass-to-charge ratio $\frac{A}{Z}$ and by magnetic triplets focused at the degrader plane F2. At high energies these ions are fully stripped of their electronic charge, equal to their nuclear charge. Hence in the degrader they lose energy proportional to their nuclear charge. This finally helps in the isotope selection after the degrader by another set of two dipole magnets placed before F3 and F4.

2.2 The isotope separator on-line (ISOL) technique

Proton beams with energies around 1 GeV or light-ion beams with a few 100 MeV/u hit a thick target of elements up to the heaviest target material uranium to undergo

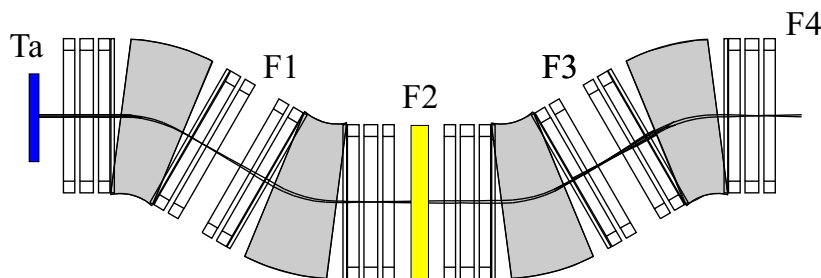


Figure 2.3: The layout of the GSI fragment separator for radioactive beams at relativistic energies. “Ta” is the target where the relativistic primary beam impinges to create secondary beams which are then focused by magnetic triplets at focal planes F1, F2, F3, F4 and mass separated by magnetic dipoles (denoted by filled areas). A degrader is placed at the second focal plane for nuclear charge selection (Courtesy W. Martin).

nuclear fission, fragmentation or spallation. The radioactive products in the target matrix are evaporated out by properly heating the matrix. Chemically reactive elements or compounds like gaseous fluorine are sometime applied to the target in order to produce molecular compounds like fluorides with high vapor pressure and to extract the chemically selected atoms as fast as possible. The atoms are ionized in an ion source using different ionization technique like surface, plasma, or laser ionization, before they are electrostatically accelerated to energies ranging from 10 to 100 keV.

The chemical selectivity is in most cases not sufficient to deliver mono-isotopic beams, hence it is necessary to perform selective ionization in the ion source which is attached directly to the target as shown in Figure 2.4. The plasma and the surface ion sources were the two most common ion sources, until recently the highly selective RILIS (Resonance Ionization Laser Ion Source) [Klu1985] came into operation [Kös2003]. In the plasma ion source the ionization is performed by the formation

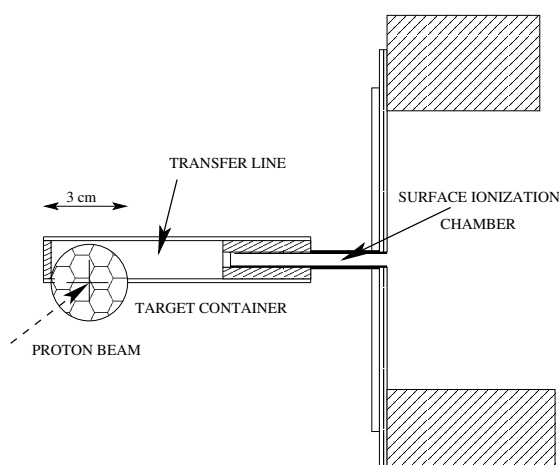


Figure 2.4: Schematic diagram of a surface ion source showing the essential parts common for other ion sources connected directly to the radioactive beam production target.

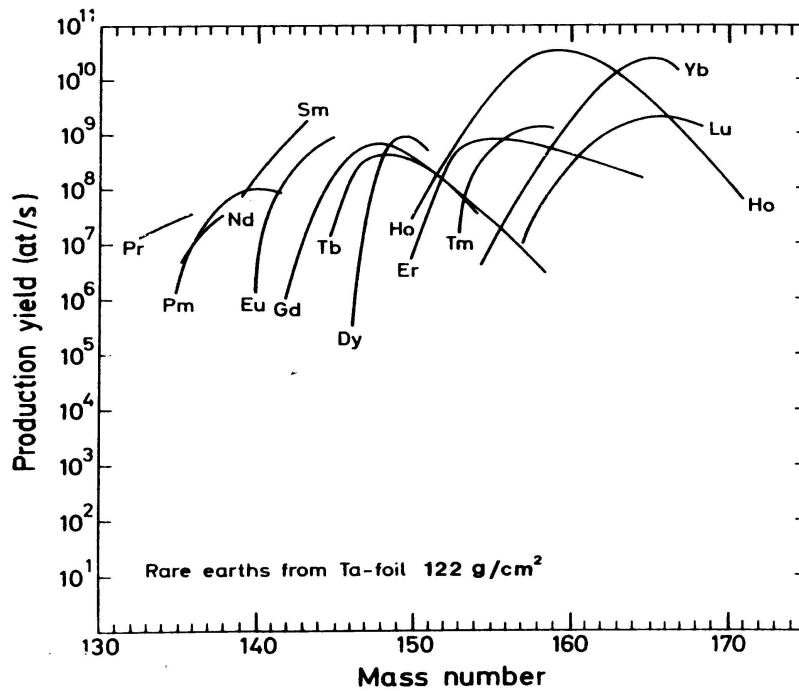


Figure 2.6: The production yields of different radioactive nuclides in the rare earth element region produced by a 1 GeV proton beam impinging on a tantalum foil target [Bjø1986].

background due to surface ionization. In some cases this can be avoided by proper choice of target and ion source material. For example, for the production of Yb at ISOLDE, a Ta powder target can be used in combination with a hot tungsten surface ionizer [Bjø1986]. This results in suppression of all other lanthanides by two to three orders of magnitude relative to Yb because of their longer delay on the surface of the Ta powder grains as compared to Yb. However this kind of selectivity holds only for a few elements. An extreme example for the opposite case is the production of radionuclides of the rare earth elements as shown in Figure 2.6. Here, a tantalum foil target is bombarded by a proton beam [Bjø1986]. Since the chemical properties of the rare earth elements are quite similar, a large number of rare earth nuclides are simultaneously produced and ionized on a hot tungsten surface. The use of RILIS with a standard target unit can enhance in such a case the production of a given isotope to some extent, but cannot suppress the huge isobaric background. To overcome this problem, to drastically decrease the beam emittance, and to have variable temporal ion bunch length the LIST was proposed [Bla2003c, Wen2004] as an advanced RILIS [Klu1985].

Principle of a laser ion source trap

The basic principle of the LIST as laid out in the Figure 2.7 is to repel electrostatically all the surface ions defusing out of the integrated target-ion-source chamber and to use this unit as a radioactive atom source only. The emerging atoms are then

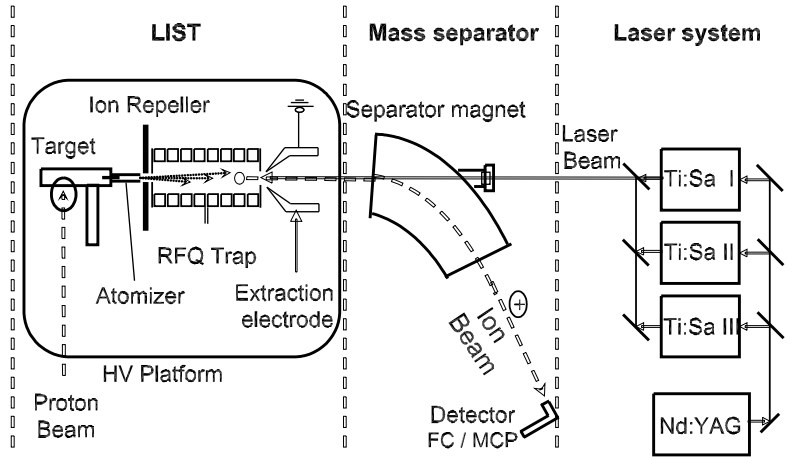


Figure 2.7: Schematic diagram of a typical laser ion source trap (LIST). Apart from the proposed laser setup, the components inside the rounded box show the upgrade needed from Resonance Ionization Laser Ion Source to LIST. Compared to Figure 2.4, here the surface ionization source is called atomizer. The repeller and the radiofrequency quadrupole trap adds to that unit. Details are given in the text.

subjected to resonance laser ionization inside a buffer gas filled linear RFQ (radio-frequency quadrupole) ion trap. The presence of the repelling potential suppresses all surface ionized ions, thereby getting rid of isobaric interferences in the required radioactive ion beam. Since the ionization is done via a multi-step resonant excitation, it is highly selective. The mono-isotopic ions thus formed are cooled and bunched inside the RFQ ion trap which is now well studied as beam preparatory device. Such devices are also known as RFQ coolers and bunchers in many low-energy radioactive beam facilities particularly for experiments on Penning trap mass measurements [Her2001, Nie2001]. They are based on the principle of a linear Paul trap [Pau1953, Pau1989] where the transversal confinement of the ions is achieved by the application of an alternating voltage 180 degrees out of phase for the adjacent poles as sketched in Figure 2.8. To trap the ions along the longitudinal direction, the four rods are segmented and proper DC voltages are applied to them in order to have a potential distribution along the traps axis similar to the one plotted in Figure 2.8.

Figure 2.7 shows the schematic diagram of a laser ion source trap, including the separator magnet and laser system. The first region of Figure 2.7, where the selective ionization takes place, is depicted in Figure 2.8 in more detail. Proton bunches with an energy of about 1 GeV and $5 \mu\text{C}$ charge impinge on a thick target to produce different radioactive atoms. They are then evaporated out of the target matrix to be further transported by diffusion to the atomizer, which was previously termed as surface ionizer, towards the RFQ. The atomizer is a small tube made of a high-temperature-material because of the required thermal stability. It is resistively heated to a temperature of about 2000°C so that the atoms do not stick on the surface of the atomizer. The isotope under investigation as well as unwanted species

such as isobars, atoms or ions of other mass number, or molecules diffuse out of the orifice of the atomizer tube, some as surface-ionized species, some as neutral atoms or molecules. The ions are rejected by a repeller, *i.e.* an electrostatically repelling electrode, and only the atoms can enter the RFQ trap. These radioactive atoms are then selectively ionized by stepwise resonant laser ionization inside the trap which helps to confine them as soon as they are ionized¹. Buffer gas inside the trap thermalize the ions and the axial trapping potential can be used to accumulate the ions and to eject them as ion bunches to be delivered towards the separator magnet. The laser system is a combination of up to three tunable Ti:Sa lasers pumped by a Nd:YAG laser to access a wide range of isotopes [Rau2004]. Important parameters of the LIST are the atomic beam divergence and hence the overlap with the laser field, the cooling time, and the accessibility of exotic nuclides, as well as the ionization efficiency. Based on the experimental data available a feasibility study was performed within this work which will be presented in the following subsections.

Simulation studies and the RFQ trap design

Simulations were performed to study the feasibility of this kind of ion source and to specify the optimal design and working parameters for efficient cooling, shortest possible delay time, low emittance, and good overall efficiency. The simulation program used takes into account the motion of the ions in RF and DC fields as well as the beam cooling by buffer gas collision. There are different ways to handle the cooling process whose merits and drawbacks are discussed in [Kim1997]. For the performed Monte Carlo (MC) simulation the Realistic Potential Model [Kim1997, Sch1999] for ion-neutral collision was used. The MC simulation accounts for the collisions by using statistical probabilities and the following assumptions were used:

- Ion-ion interactions are neglected compared to ion-neutral gas interactions due to the low density of the ions.
- The collisions of the ions with the neutral gas molecules are considered to be elastic.

Though there are many collision potential models that can be used for the MC simulation like the classical hard-sphere model with constant or variable size etc., the most appropriate one is the Realistic Potential Model. This gives results which are demonstrated to be in good agreement with experimental data. The potential used here is

$$V(r) = \frac{C_{12}}{r^{12}} - \frac{C_6}{r^6} - \frac{C_4}{r^4}, \quad (2.1)$$

¹It should be noted that a LIST does not work for alkaline and noble gas elements. This is not a drawback since, in the first case, surface ionization ion sources work best for alkaline elements and deliver rather pure radioactive beams. In the case of noble gases, efficient laser systems are still missing. Here, however, also pure radioactive beams are obtained by a combination of a plasma ion source with a water-cooled transfer line connecting the target chamber with the ion source.

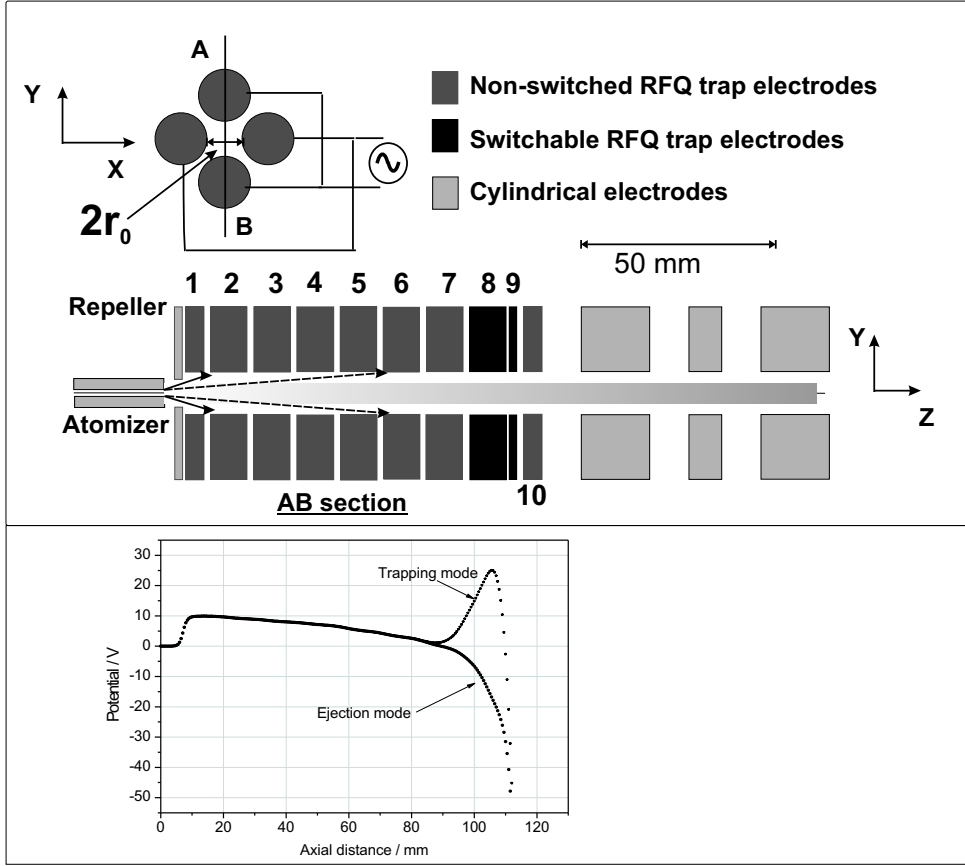


Figure 2.8: Top: To-the-scale drawing of the radiofrequency quadrupole (RFQ) trap assembly for a Laser Ion Source Trap (LIST) along with the repeller and a set of an einzel lens system. The upper part shows the X-Y planer view of the four-rod quadrupole. The lower part shows the AB cut section of it along with the projected areas of the two-component atomic beam as well as the laser illuminated volume in the Y-Z plane. Bottom: The longitudinal potential along the symmetry axis used in the LIST RFQ trap for simulations of ion beam cooling. The 10 eV potential hill is created by the repeller voltage of 12 V. The potential distribution is calculated using the SIMION code [Dah2000] with voltages applied to the segments as compiled in Table 2.1. The voltages are given relative to the potential of the atomizer.

where the C 's are constants.

The inverse fourth power term in distance r accounts for the attraction between the charge of the ion and the electric dipole it induces in the polarizable neutral atom. The coefficient is known very accurately, since it is given by the simple expression

$$C_4 = \frac{1}{2}q^2\alpha, \quad (2.2)$$

where q is the ionic charge and α is the polarizability of the neutral entity [Ell1978]. The inverse sixth power in r accounts for the charge-induced quadrupole plus the

London dispersion attraction [Kim1997]. The coefficient C_6 can often be calculated approximately but it is seldom known as accurately as C_4 . The inverse twelfth power term in r is an empirical representation of the short-range repulsion due to close approach of two atoms [Kim1997].

Table 2.1: Dimensions of the LIST ion beam cooler and buncher and applied voltages relative to the 60 kV at which the ISOLDE target/ion source system is put to. If two values for the voltage are given the first one is for trapping and the second one is for ejection. The gap between two adjacent electrodes is 2 mm.

Element	Dimension (mm)	Applied voltage (V)
inner diameter of atomizer	3	0
length of atomizer	25	0
inner diameter of repeller electrode	6	12
thickness of repeller electrode	2	12
distance between opposite rods $2r_0$ (see Figure 2.8)	12	
length of segmented electrodes : #1	5	9
#2	10	8
#3	10	7
#4	10	6
#5	10	4
#6	10	2
#7	10	0
#8	10	25/1
#9	2	115/0
#10	5	-5

The atomizer in the simulation is a replica of the existing ionizer at the ISOLDE target-ion-source assembly. It is a tube 25 mm in length with an inner diameter of three millimeter. Laser spectroscopic studies with an effusive atomizer heated to a temperature of 1200°C [Mar1967, Wen2002] show, that the atoms effusing out of the source tube can be divided into two distinct components: One is a narrow beam with an opening angle of $\pm 4^\circ$ coming directly from the entrance of the atomizer without undergoing any collisions on the wall. The other one is a broad component with an opening angle of about $\pm 20^\circ$. Figure 2.8 sketches the geometrical divergence of these two atom beam components along with the overlapping laser beam projected in the x-y plane. The opening angle of $\pm 4^\circ$ corresponds to the ratio of the radius to the length of the atomizer. The $\pm 20^\circ$ beam corresponds to the cosine square distribution of the atoms emerging from the end part of the atomizer. The intensity ratio of the $\pm 4^\circ$ component to the $\pm 20^\circ$ component is about 1:6 for the given atomizer geometry. The initial atoms were considered to be at thermal velocities with $T=1200^\circ\text{C}$ which corresponds to nearly 500 m/s. The above mentioned input parameters lead to the optimal design of the RFQ trap whose to-the-scale sketch is shown in Figure 2.8. The dimensions and parameters of its components are tabulated

in Table 2.1. The trapping potential distribution shown in Figure 2.8 is along the axis of the RFQ trap. The results presented here are based on the following realistic assumptions made or parameters taken:

1. Cesium atoms or ions ($A = 133$) were taken as species of interest.
2. Helium was used as buffer gas at a pressure of $P_{\text{He}} = 3 \times 10^{-3}$ mbar.
3. A peak-to-peak radio-frequency (RF) voltage of 135 V at a frequency of 1 MHz on the RFQ trap was considered.
4. A pulsed laser system with a repetition rate of 10 kHz was assumed to deliver light intensive enough to ionize all atoms in a cylindrical volume of 6 mm diameter.
5. Atoms are coming out of the atomizer in two components with opening angles as mentioned before. They are considered to be ionized at random positions inside the RFQ trap within a length of 5 cm from the entrance electrode (#1). This distance corresponds to the flight path of an atom with thermal velocity of ~ 500 m/s in between two subsequent laser pulses of a laser with 10 kHz repetition rate.

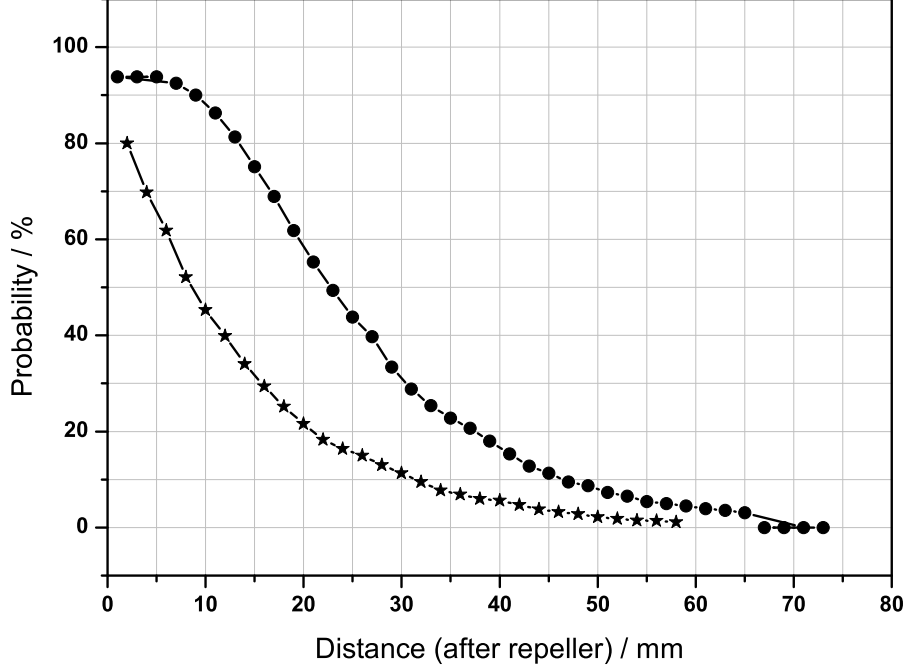


Figure 2.9: The probability of an atom to be within the laser illuminated volume plotted as a function of distance from the potential hill. The origin of the x-axis is 7 mm away from the exit of the atomizer. The filled circles are data points for the narrow atomic beam component (opening angle $\pm 4^\circ$) and the asterisks are those for the broad component (opening angle $\pm 20^\circ$). The solid lines are to guide the eye.

Efficiency estimation

Figure 2.8 shows the schematic of the LIST RFQ trap along with the atomic beam divergences and the laser illuminated volume as used in the simulations. In the simulation 1000 atoms comprising the narrow beam were created with an initial velocity of 500 m/s directed randomly within an opening angle of $\pm 4^\circ$ starting from the entrance of the atomizer. Another 1000 atoms comprising the broad distribution were created with the same velocity as before but having an opening angle of $\pm 20^\circ$ and initial position distributed randomly over the exit area of the atomizer. The atomic beam divergence shown in Figure 2.8 is the divergence in absence of any buffer gas. The simulation takes into account the neutral atom collisions with the buffer gas molecules. Thus, atoms which remain inside the laser illuminated volume within a distance of 50 mm after the potential hill can be ionized by a laser with a repetition rate of 10 kHz. The probability of an atom to be within the laser illuminated volume as a function of the distance from the potential hill, which is 7 mm away from the exit of the atomizer, is shown in Figure 2.9. It is obvious, that atoms from the narrow beam component has higher probability to remain within the laser field for a longer distance than atoms from the broad component. Nevertheless, the calculation shows that they contribute almost equally to the number of ions formed because of the intensity ratio of the two components.

The number of ions produced by resonant laser ionization is calculated in the following way: The overlap distance of 50 mm is divided into 25 blocks of two millimeters each. Atoms are distributed in these blocks according to the probability distribu-

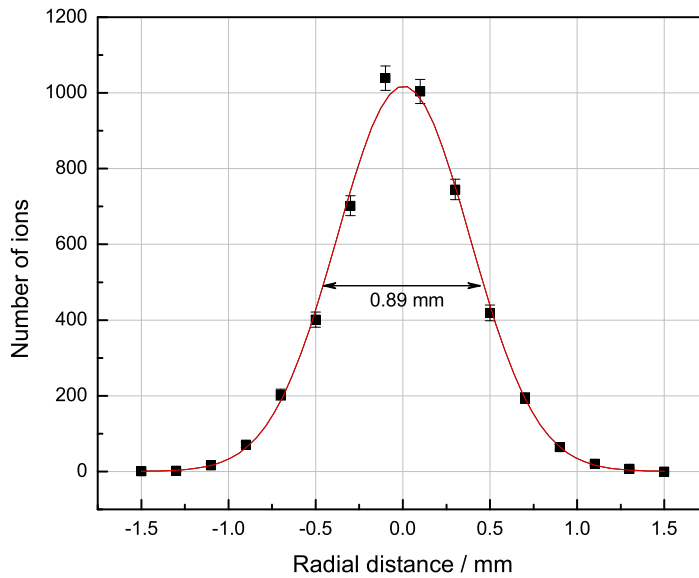


Figure 2.10: Distribution of cooled Cs^+ ions in radial direction after a cooling time of $\tau_{\text{cool}} = 3.15$ ms in helium buffer gas with a pressure of $P_{\text{He}} = 3 \times 10^{-3}$ mbar. The Full-Width-at-Half-Maximum (FWHM) is 0.89 mm. The errors are statistical ones and the fitted solid curve is a Gaussian.

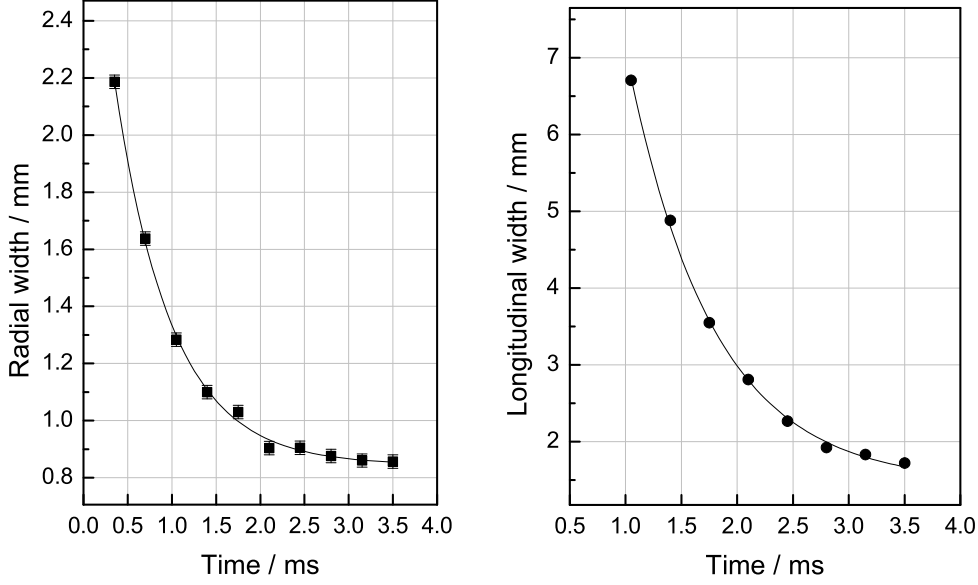


Figure 2.11: Radial and longitudinal Full-Width-at-Half-Maximum (FWHM) of the Cs^+ distribution as a function of cooling time. Helium buffer gas at a pressure of 3×10^{-3} mbar was used. The cooling time constant for the exponential decay are $\tau_{c,r} = 0.67$ ms for radial cooling and $\tau_{c,l} = 0.76$ ms for longitudinal cooling.

tion shown in Figure 2.9. This gives an overall efficiency of $\sim 23\%$ for 100% laser ionization efficiency and, more realistically, $\sim 14\%$ for 60% laser ionization efficiency. Though this efficiency is nearly the same as for a common RILIS, the beam from LIST is free from any surface-ionized nuclide which is a major advantage compared to the conventional RILIS.

Radial and longitudinal cooling

The ion distribution inside the trap was simulated for different periods of trapping (*i.e.* cooling) time. The radial and longitudinal distribution of the ions were fitted with a Gaussian:

$$N = N_{\max} \exp\left(-\frac{(x-x_c)^2}{2\sigma^2}\right), \quad (2.3)$$

where N and N_{\max} are the number of ions at a radial distance x from the center and at the center respectively. x_c is center of the distribution while σ is the standard deviation. The FWHM (full-width-at-half-maximum) of these fits give the measure for the ion beam cooling in either dimensions. For example in Figure 2.10 the FWHM of the ions radial distribution after $\tau_{\text{cool}} = 3.15$ ms is only 0.89 mm. The FWHM were then determined for different cooling times. The results are shown in Figure 2.11. The left diagram gives the radial and the right one the longitudinal FWHM as a function of the cooling time. These plots can be very well described by

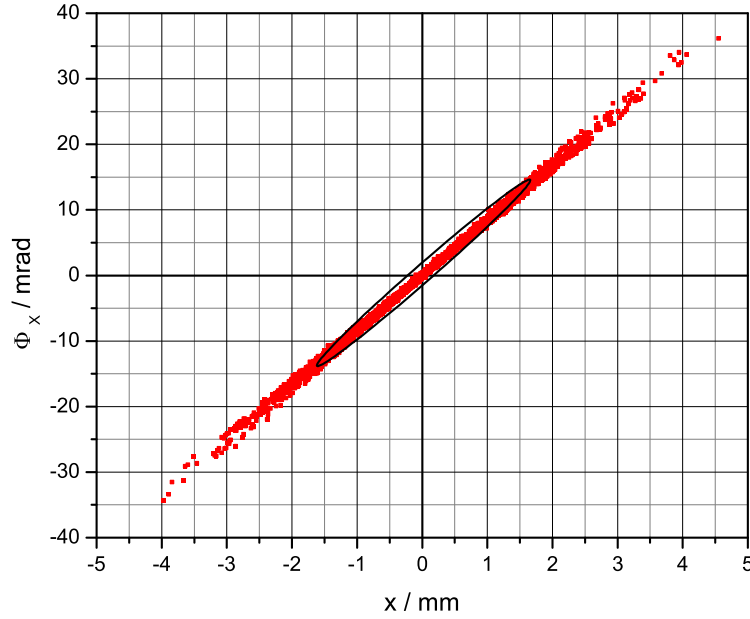


Figure 2.12: Emittance ellipse of the extracted ion bunch after cooling for 3 ms. The solid ellipse shown covers 80% of the total number of ions. The parameters are the same as in Section 2.2.1. The area of the emittance ellipse is $\epsilon_{80\%} \approx 3\pi \text{ mm}\cdot\text{mrad}$.

exponential fits with decay time constants of 0.67 ms for the radial and 0.76 ms for the longitudinal cooling.

Beam extraction and emittance

The ions - after being cooled - are extracted out of the RFQ trap by switching the potential of it's last segment (#8) from 25 V to 1 V and the extraction electrode (#9) from 115 to 0 V (Table 2.1). This gives a smooth ejection potential as shown in Figure 2.8. The einzel lens system comprised of three cylindrical electrodes is set to certain voltage to focus the beam. The position and momentum of all extracted ions are calculated in the field-free region. Figure 2.12 gives the position and angular divergence in the x -direction of each ion at a distance of $\sim 8.5 \text{ cm}$ from the exit of the RFQ trap. The fitted ellipse covers $\sim 80\%$ of the total number of ions. The emittance of the extracted beam is estimated to be $\epsilon_{80\%} \approx 3\pi \text{ mm}\cdot\text{mrad}$. The present beam emittance of ISOLDE is about $10 - 20\pi \text{ mm}\cdot\text{mrad}$ [Wen2003]. Thus, LIST can improve the emittance by about an order of magnitude.

The spread of the ion bunch in the longitudinal direction can be varied widely from a few tens nanoseconds to several microseconds by varying the longitudinal potential. This allows delivery of ions in different modes.

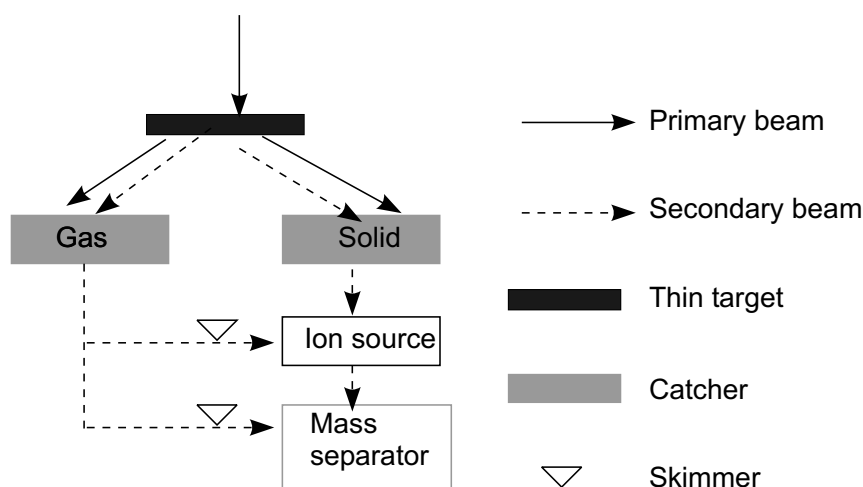


Figure 2.13: Classification of the non-conventional Isotope Separator On-Line (ISOL) techniques (adapted from [Den1997]).

2.3 Other techniques

Due to the production and extraction process it is impossible to deliver radioactive beams of refractory elements with the conventional ISOL technique [Kir2003]. Figure 2.13 shows three different possibilities to overcome this problem. To minimize wall collisions, the use of thin target is a common approach. This is counter productive, since in most of the cases only a fraction of the excitation function of the nuclear reaction can be utilized. After the production, the following methods are adopted:

Solid catcher-ion source method: The hot ions are stopped and neutralized in a foil called catcher. The atoms are then released by heating the catcher and re-ionized in an ion source. This was the approach adopted by the recently shut-down GSI on-line isotope separator. In this case, to have universality in ionization, a forced-electron beam induced arc-discharge (FEBIAD) ions source was used [Kir2003]. Thereafter the ions were extracted out the target/catcher chamber by an electric field through a small extraction hole.

Helium-jet method: To minimize wall collisions and hence loses, the ions in this case are stopped and neutralized in a gas catcher. A constant helium-jet flow transports these atoms into an ion source where they are re-ionized. This approach, being not so successful in enhancing the efficiency beyond 0.4% is almost abandoned except in JAERI [Ich2003] where it is still in use for neutron-deficient isotope production.

Ion guide method: This is the most successful method out of the three non-conventional ISOL techniques for the production of refractory elements. It is similar to the last mentioned approach except here, the non-neutralized ions out of the gas catcher are of importance and hence no ion source is needed.

In the commonly known ion guide isotope separator (IGISOL) method the ions are fast extracted out of the gas catcher by an ion guide technique so that they

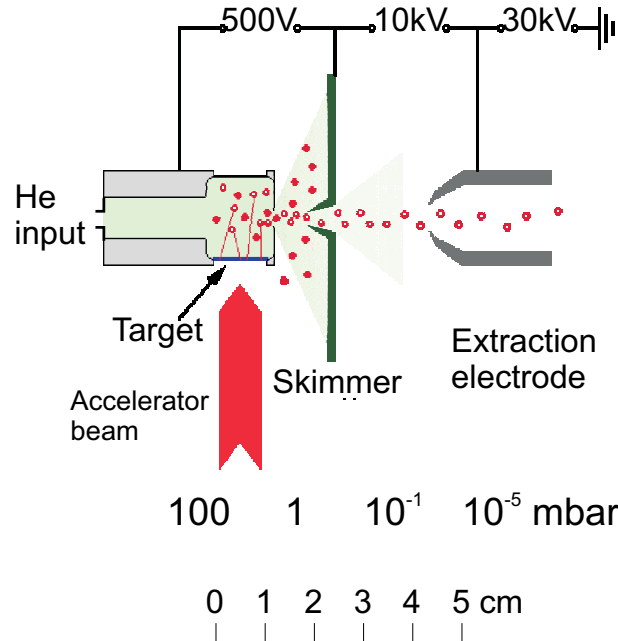


Figure 2.14: The generic Ion Guide Isotope Separator On-Line (IGISOL) setup with the target for production, gas chamber for stopping, nozzle for extraction, skimmer for differential pumping, and the extraction electrode for extracting the radioactive singly charged ions. Typical voltages and the gas pressures are also shown. The open circles denote the radioactive ions and the closed ones are the neutral particles of both neutralized products and buffer gas.

can be still retained in the 1^+ charge state and can then directly be accelerated towards the mass separator. Since the recoil products have high forward momenta and short path to travel through the thin target, they spend almost no time within the target to undergo any chemical reaction. This resulted in the possibility to study neutron-rich fission products of refractory elements like Nb, Mo, Tc, Ru, and Rh. A vivid description of the design, concepts, and usage of the IGISOL technique can be found in [Den1997] and [Äys2001]. Though this technique is now also implemented for heavy-ion induced fusion reactions, here only a brief description of the technique used for light-ion induced fission will be given.

Figure 2.14 sketches the generic IGISOL setup. The primary beam of both light and heavy ions hits a target whose thickness is normally chosen to be equal to the maximum range of the beam in the target. The energetic reaction products are slowed down in the buffer gas, generally helium and in some cases argon. Singly charged ions are then fast transported through a differentially pumped electrode system to the high vacuum section of the isotope separator for further acceleration and separation according to their masses.

The efficiencies so far achieved by the IGISOL technique are 1-10% for proton induced fusion reactions, 0.1-1% for heavy-ion induced fusion reactions, and only .01% for light ion induced fission.

Chapter 3

The triple trap mass spectrometer ISOLTRAP

The mass of an atom is a fundamental property, unique like a fingerprint. It is the sum of the masses of its constituent neutrons, protons, electrons and their binding energies.

While the masses of the stable nuclides are very well known [Wap2003], the precision of the known masses falls off rapidly for the unstable nuclides with respect to β -decay. Apart from the general extension of mass measurement to very short-lived nuclei, nuclear physics demands very accurate determination of the masses of some specific unstable nuclides. Accurate experimental mass values offer stringent tests for different mass models [Lun2003]. They also help to extend these models to very short-lived nuclides that cannot be produced but can reveal general nuclear structure. Deviation of the nuclear binding energies from the smooth trend given by simple liquid drop models unveils nuclear shell structures. Mass differences between the odd and even numbered nuclei show the strength of the pairing force. Strong ground state deformations show up as deviations from the smooth trend of the two neutron separation energies between shell closures. In addition to these necessities, particle physics requires very accurate mass difference determination between radioactive parent and daughter nuclides which undergo superallowed $T = 0$ ($0^+ \rightarrow 0^+$) β -decay. Precise mass values contribute to test the conserved vector current (CVC) hypothesis and to check the unitarity of the Cabibbo-Kobayashi-Maskawa (CKM) matrix [Tow2003]. The binding energy also determines how much energy is available for a nuclear reaction, thus playing a fundamental role in the elaboration of models for stellar evolution and, in case of some explosive events, critical aspects of nucleosynthesis [Bis2003].

Measurements of decay or reaction Q -values (overall energy balances) have been for many decades the only source of mass determinations for most of the radioactive nuclides. The measurements of mass differences in long decay chains linking very short-lived nuclides with a stable one can in principle allow for the determination of mass of the unstable nuclide. This suffers badly from the systematic error propagation along the chain and nuclear energy levels are needed to be known for the unstable as well as for all the subsequent daughters until the stable one. The

Q -value determination from a nuclear reaction needs to have proper target and projectile which can directly lead to the desired nuclide that can be identified and also the kinetic energy can be measured. This is in general not the case for most of the unstable nuclei which are of great importance.

Conventional magnetic mass spectrometers were for the first time used on-line for direct mass measurements at the PS (proton synchrotron) [Thi1975] and at the on-line isotope separator ISOLDE, both at CERN, in the 1970s. Until 1997 these kind of spectrometer was still in use at the on-line separator at Chalk river [Sha1991]. Due to limited resolving power of the spectrometer, simultaneous radioactivity measurement on the unstable nuclide was used to resolve any ambiguity regarding the identification and, in case of isomers, the nuclear state.

Since the last decade new direct mass measurement techniques were developed at different facilities. Time-of-flight mass spectrometers was in use for direct mass measurements on projectile or target fragments at LAMPF/Los Alamos [Vie1986, Wou1987, Wou1988] and is very successfully pursued at GANIL/Caen [Bia1989, Sar2000]. At GANIL time-of-flight mass measurements are also performed at the cyclotron CSS2 [Aug1994, Cha1998] itself which gives longer flight path and hence higher resolution. Since the fragments recoil out without any delay, these techniques are well suited for very short-lived nuclides, but their applicability is restricted to light-nuclei with a typical resolving power of 3000. For heavy-nuclei the major limitation is due to particle identification. At the storage ring ESR at GSI-Darmstadt, both the Schottky and the Isochronous techniques have been implemented successfully for mass measurements on circulating beams of highly-charged ions [Gei2001, Rad1997, Hau2001]. A radio-frequency transmission spectrometer MISTRAL located at ISOLDE also serves for direct mass measurement on very short-lived nuclides [Lun2001].

Since the late 1940s static electric and magnetic fields have been employed for charged particle confinement in small volumes within what is now known as Penning trap and to determine the mass of these trapped particles by their cyclotron frequency $\omega_c = (q/m)B$ measurement (q , m denoting the charge and mass of the particle and B is the amplitude of the external magnetic field) [Hip1949]. Since then different developments in the Penning trap technique have made it the instrument of choice for high-precision mass measurements. This is reflected by the results obtained on electrons, positrons, protons, antiprotons, ^3He and tritium ions, and ionized light molecules such as N_2 and CO [Grä1980, Sch1981, Cor1989, Gab1990, Ger1990, Hag1991, Dyc1992, Dyc1993]. In all cases relative mass uncertainties of better than 10^{-9} have been obtained. Except for the antiproton, these experiments create or release the charged particles from material which is within or very close to the trap. Special techniques, such as narrow-band resonance detection via image currents and cooling by synchrotron radiation or by dissipating the ions' energy in cooled external resistive circuits, are employed. However, these techniques are till now only feasible for light ions with large motional frequencies.

In analytical chemistry Penning traps are widely used, where large molecules are identified with ppm resolution over a broad mass range. Since higher precisions are

not needed in such applications, the ions in the trap are driven to higher motional amplitudes and the image current of a large number of different ion species can be detected and Fourier analyzed [Buc1993]. This technique is known as the FT-ICR (Fourier transform ion cyclotron resonance) method.

A Penning trap mass spectrometer for the investigation of short-lived radionuclides delivered from an on-line mass separator has to fulfill a number of specific requirements. The on-line facilities (see Chapter 2) typically deliver continuous ion beams of some 10 keV energy which need to be retarded to almost thermal energy keeping the emittance to an acceptable value for loading the ions into the traps. Bunching of the so prepared beam is necessary to increase the loading efficiency. To be economic with the available beam time, the preparation techniques have to be efficient, since the delivered intensity goes down further away from the valley-of-stability. The ion cooling and the resonance detection schemes should cover a large accessible mass range to allow fast switching between the different nuclides of interest. To reduce the systematic uncertainties caused by the imperfection in the electric and magnetic field within the trap volume, one has to reduce these imperfections over a large volume. In addition, the ion's kinetic energy should be kept as small as possible.

Fulfilling all these demands a triple trap system has been developed and installed at ISOLDE-CERN. The present setup at the PS-Booster ISOLDE is shown in Figure 3.1. There has been a tremendous development regarding the setup and performance of the ISOLTRAP experiment since 1996 when the full ISOLTRAP setup was described in detail [Bol1996]. In the following a description of the principle used in the ISOLTRAP mass spectrometer, the experimental setup, the mass measurement procedure, and the performance of the present system will be described.

3.1 Principles of the ISOLTRAP mass spectrometer

The ISOLTRAP mass spectrometer is divided according to functionality into three parts as shown in Figure 3.1. The first part is a radiofrequency quadrupole (RFQ) trap [Her2001] for deceleration, cooling, and bunching of the ion beam provided with an energy of 60 keV by the on-line isotope separator ISOLDE [Kug2000]. A gas filled cylindrical Penning trap is the second functional element. Its purpose is the isobaric separation and cleaning of the ion beam via a helium buffer gas cooling technique [Sav1991]. The third component is a hyperbolic Penning trap for high-precision cyclotron frequency measurements and thus mass determination of cleaned and well prepared ions. In the following, principles and properties of a RFQ trap and a Penning trap will be described as far as they are applicable to the ISOLTRAP spectrometer. More detailed description concerning the theoretical aspects of RFQ traps can be found in [Pau1953, Pau1989, Daw1995, Gho1995] and Penning traps in [Bro1986, Bol1990, Kre1991].

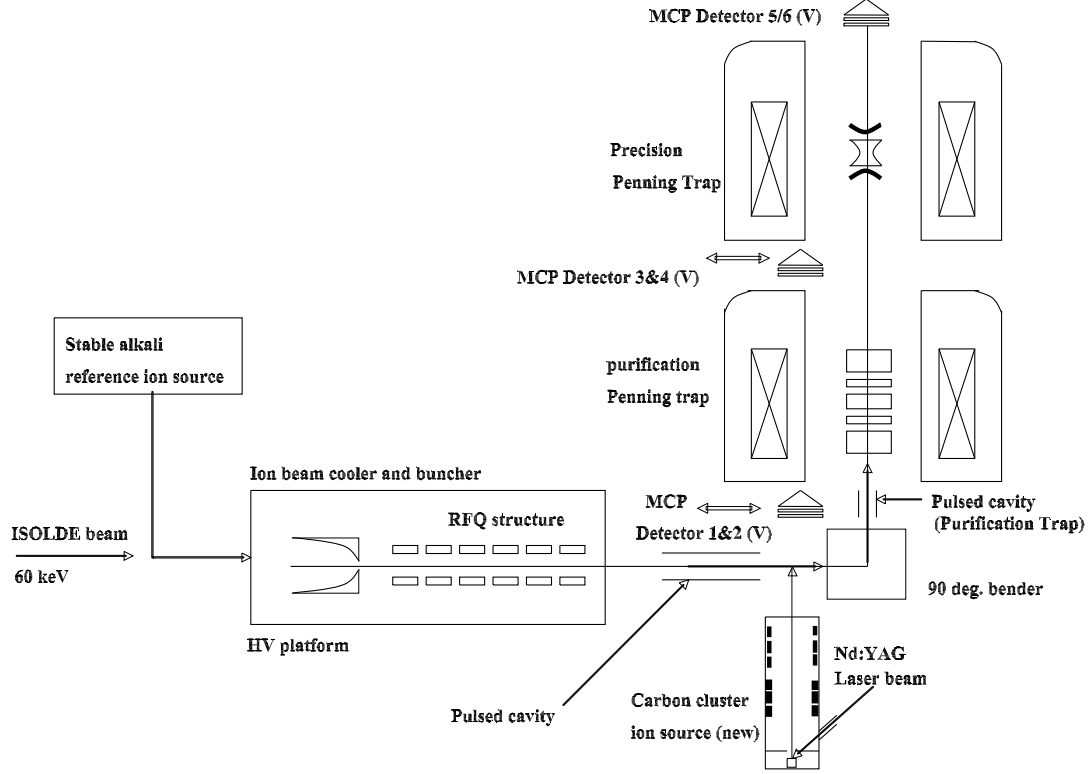


Figure 3.1: A general overview showing the main functional parts of the ISOLTRAP setup.

3.1.1 An RFQ trap for cooling and bunching

An ideal Paul mass filter, as originally designed by Wolfgang Paul and co-workers [Pau1953], consists of four parallel hyperbolic rods where radiofrequency voltages are applied to the opposite pairs of it. The radial confining force is created by the focusing effect of the ideal quadrupolar field varying with time. Similar fields can be created by using circular rods instead of hyperbolic ones but an almost ideal field is only obtained within a small radius compared to the distance between the opposite rods. Furthermore ions can be trapped in axial direction of the device, by use of axially segmented rods and a DC trapping potential applied to the segments, as shown in Figure 3.2. While being trapped, the ions can also be cooled by collisions with an inert buffer gas like helium at room temperature. ISOLTRAP is using such an RFQ cooler and buncher for beam accumulation, bunching, and emittance improvement [Her2001, Kel2002]. The ISOLDE radioactive ion beam is accumulated for a certain time (typically a few ms) so that the ions settle down at the potential minimum of the trap and are ejected as an ion bunch.

In case of an ideal quadrupolar potential, the radial confinement of the ions can be described by the Mathieu equation of motion [Pau1989, Daw1995], which also determine the stability criteria of the ion motion. Due to the strong radial and azimuthal dependence of the axial electric field, the ion motion in the trap can

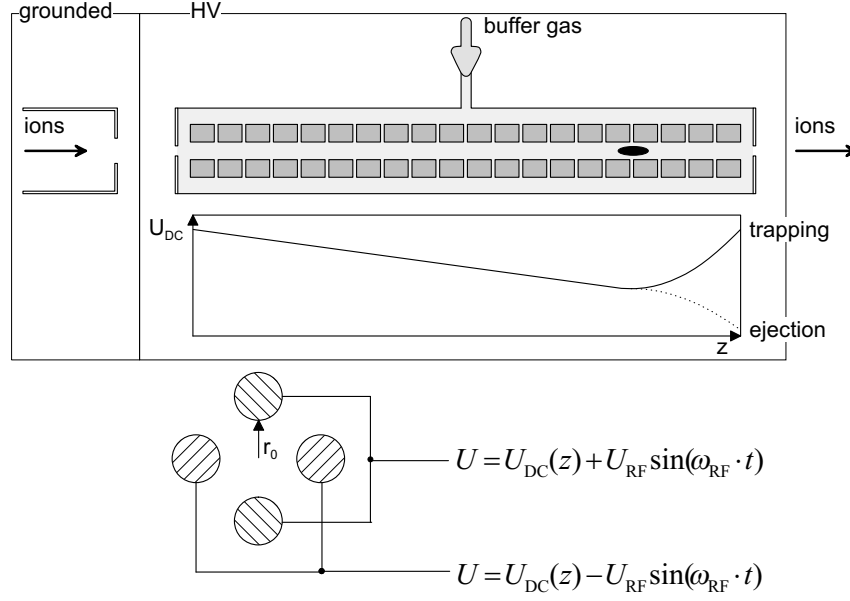


Figure 3.2: Sketch of the segmented radiofrequency ion beam cooler and buncher. A schematic side view together with the electric potential along the symmetry axis is shown in the upper figure. The lower figure shows the four rods and electrical connections to apply RF and DC voltages.

not exactly be described by Mathieu equations but it is still useful to consider the motion similar to that of a particle in a linear superposition of an axial DC field and a quadrupolar RF field. The ion trajectory in the RF field can be simplified to that in a pseudopotential well with depth V_{RF} [Kap1965, Deh1967].

The pseudopotential is generated by applying an RF voltage of amplitude $\pm U_{\text{RF}}$ and frequency ω_{RF} in a configuration as shown in Figure 3.2. The resulting pseudopotential for such an RFQ cooler and buncher can be expressed as

$$V_{\text{RF}}(r) = \frac{qU_{\text{RF}}}{4r_0^2}r^2 \quad (3.1)$$

where $2r_0$ is the distance between the opposite rods and

$$q = 4 \frac{eU_{\text{RF}}}{mr_0^2\omega_{\text{RF}}^2} \quad (3.2)$$

is the relevant Mathieu parameter. The other parameter a (see Figure 3.3) being a function of a DC potential between opposite pair of rods of the same segment, is 0 for an RFQ cooler and buncher. For $a > 0$ the RFQ can be used as a mass filter. e/m is the charge-to-mass ratio of the stored ion. The solution of the Mathieu equation shows that the motion is stable as long as $q < 0.908$, as shown in Figure 3.3(B). In the radiofrequency field, the ions perform a micro-motion at the frequency ω_{RF} of the field and a macro-motion which is the oscillation in the pseudopotential V_{RF} . To a good approximation for $q < 0.6$ [Her2001], its oscillation frequency is

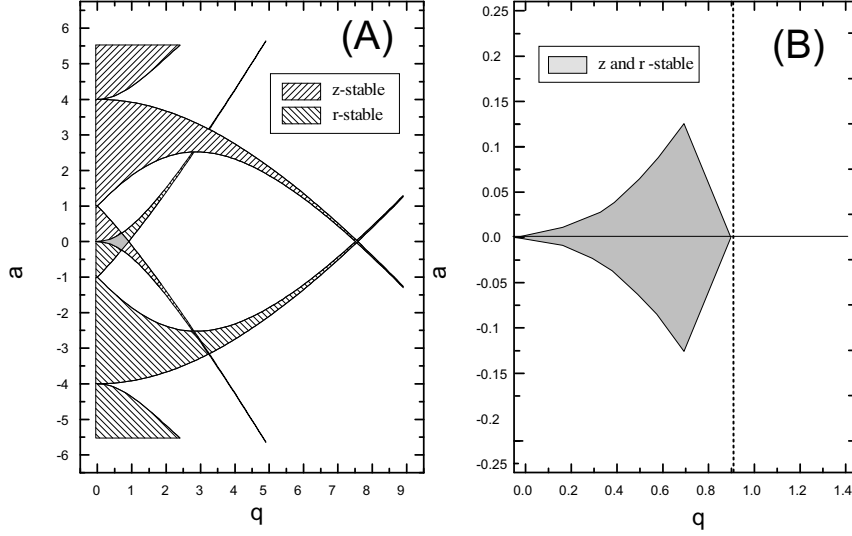


Figure 3.3: The a and q Mathieu parameters for stable ion motion in an radiofrequency quadrupole (RFQ) trap. The radial and axial motions are stable only for certain range of a and q values (A). The first-order stability region for stable motion in three dimensions (B). The ISOLTRAP RFQ cooler and buncher works along the $a = 0$ axis.

$$\omega_m = \frac{q}{\sqrt{8}} \omega_{\text{RF}}. \quad (3.3)$$

As an example, a singly charged ion of mass 39 u confined in an RFQ structure with $r_0 = 6$ mm, $\omega_{\text{RF}} = 2\pi \cdot 1$ MHz, and $U_{\text{RF}} = 80$ V will experience a radial trapping potential depth of about 11 V in which it oscillates with $\omega_m = 2\pi \cdot 196$ kHz [Her2001].

The DC axial potential forms a well at the end of the structure. The potential minimum can be approximated by a parabola and the potential $V_{\text{DC}}(r, z)$ must fulfill the minimal condition. The axis-symmetric quadrupole potential at the minimum is given by

$$V_{\text{DC}}(r, z) = \frac{U_{\text{DC}}}{z_0^2} \left(z^2 - \frac{r^2}{2} \right), \quad (3.4)$$

where z_0 and U_{DC} are the characteristic length and voltage of the axial DC trap. In the region where the axial potential has its minimum, the radial confinement due to the radiofrequency field is maximally counteracted by the repelling part of the DC potential. The overall potential then becomes

$$V_{\text{mod}} = \frac{U_{\text{DC}}}{z_0^2} z^2 + \left(\frac{q U_{\text{RF}}}{4 r_0^2} - \frac{U_{\text{DC}}}{2 z_0^2} \right) r^2. \quad (3.5)$$

Using the parameters given above and $U_{\text{DC}}/z_0^2 = 10$ V/cm², the radial trapping potential well is reduced by about 1.8 V compared to the RF-only case. The minimum RF voltage needed for three dimensional trapping of a charged particle can be derived from Eq. (3.5) and is given by

$$U_{\text{RF},\text{min}} = r_0^2 \cdot \omega_{\text{RF}} \sqrt{\frac{m U_{\text{DC}}}{e 2 z_0^2}}. \quad (3.6)$$

Buffer gas cooling

The stored ions in the RFQ cooler and buncher scatter elastically with the buffer gas atoms and transfer partly their energy to them. After a certain time they come into thermal equilibrium with the buffer gas ($T = 300^\circ \text{ K}$) in the trapping potential minimum.

The cooling mechanism for a large mass difference and a low relative velocity between the ion and the buffer gas atom is well understood by considering a viscous damping force proportional to the relative velocity. It is represented as

$$F = -\delta \cdot m \cdot v, \quad (3.7)$$

where m is the mass of the ion and v the relative velocity with respect to the buffer gas atom. The damping coefficient

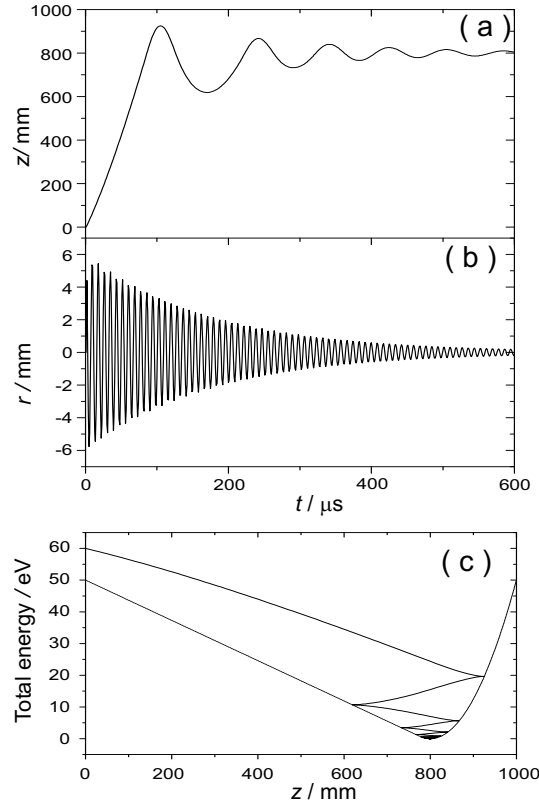


Figure 3.4: Simulation of the cooling and accumulation processes in a linear radiofrequency quadrupole trap: (a) the axial oscillation as a function of time, (b) the radial oscillation as a function of time, and (c) the total axial energy with respect to the axial position (the axial potential is also plotted).

$$\delta = \frac{e}{m} \cdot \frac{1}{\mu} \cdot \frac{p/p_N}{T/T_N}, \quad (3.8)$$

is proportional to the gas pressure p (in fractions of the normal pressure p_N) and inversely proportional to the temperature T (in fractions of the normal temperature T_N) and the reduced ion mobility μ [McD1973].

However, for the understanding of the ion loss mechanism and the final ion temperature a microscopic individual collision model incorporating realistic potentials is necessary. This is already discussed in detail in Chapter 2. Figure 3.4 shows the cooling of an Cs^+ ion simulated with the assumption of a viscous damping force in helium buffer gas where this model is a good approximation.

3.1.2 Ideal Penning trap

An ideal Penning trap is realized by the superposition of a homogeneous magnetic field $\vec{B} = B\hat{z}$ and an electrostatic quadrupole potential $U(\rho, z)$ perpendicular to the magnetic field. It allows to trap charged particles in a small well-defined volume. Moreover, there exists exact solutions to the particle's equation of motion. In the following the equations of motion for an ion stored in a Penning trap will be discussed according to Ref. [Bro1986]. The electrostatic potential can be achieved by the electrode configuration as shown in Figure 3.5 where the trap is formed by two end cap electrodes and one ring electrode, all being hyperboloids of revolution for the ideal case. It can as well be realized by cylindrical electrodes forming the ring, the endcaps, and some correction electrodes to mimic the same quadrupolar potential as in case of an ideal trap configuration.

A voltage difference of U_0 applied between the end caps and the ring electrode produces a quadrupole potential

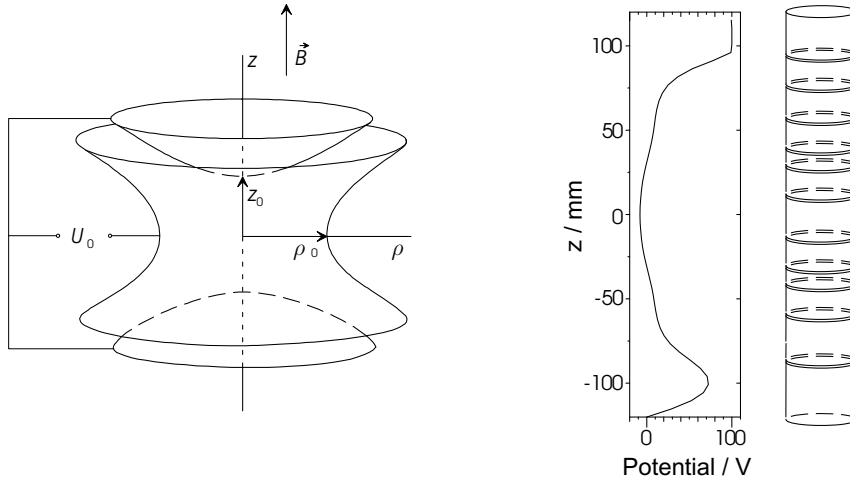


Figure 3.5: Left: Hyperbolic Penning trap configuration with the ring and the endcap electrodes. Right: A cylindrical Penning trap with voltages applied to its different segments to obtain a quadrupolar potential over a small volume.

$$U(\rho, z) = \frac{U_0}{4d^2} (2z^2 - \rho^2). \quad (3.9)$$

The characteristic trap dimension d is determined by

$$4d^2 = (2z_0^2 + \rho_0^2), \quad (3.10)$$

where ρ_0 denotes the inner ring radius and $2z_0$ is the closest distance between the two end caps.

In such an ideal electric and magnetic field configuration the axial motion of the ion is decoupled from the magnetic field. It is a simple harmonic motion

$$\ddot{z} + \omega_z^2 z = 0 \quad (3.11)$$

of an ion with mass m and charge q along the magnetic field axis. Here $2\pi\omega_z$ is the axial frequency expressed as

$$\omega_z = \sqrt{\frac{qU_0}{md^2}}. \quad (3.12)$$

The radial equation of motion is described by

$$m\ddot{\vec{\rho}} = q[\vec{E} + \vec{\rho} \times \vec{B}], \quad (3.13)$$

where $\vec{\rho}$ denotes the radial position of the ion from the trap center at any instant and \vec{E} is the radial component of the electric field and can be derived from Eq. (3.9) as

$$\vec{E} = (U_0/2d^2)\vec{\rho}. \quad (3.14)$$

Writing the radial equation of motion in terms of the pure cyclotron frequency ω_c given by

$$\omega_c = \frac{q}{m}B \quad (3.15)$$

and the axial frequency ω_z results in,

$$\ddot{\vec{\rho}} + \omega_c \hat{z} \times \dot{\vec{\rho}} - \frac{1}{2}\omega_z^2 \vec{\rho} = 0. \quad (3.16)$$

Combining Eq. (3.11) and (3.16), the general equation of motion in Cartesian coordinates can be rewritten as

$$\begin{bmatrix} \ddot{x} \\ \ddot{y} \\ \ddot{z} \end{bmatrix} - \frac{\omega_z^2}{2} \begin{bmatrix} x \\ y \\ -2z \end{bmatrix} - \omega_c \begin{bmatrix} \dot{y} \\ -\dot{x} \\ 0 \end{bmatrix} = 0. \quad (3.17)$$

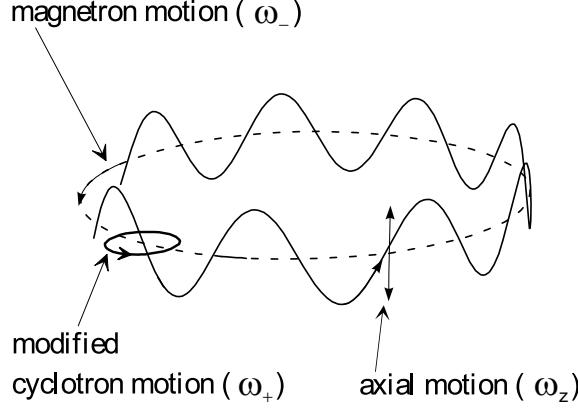


Figure 3.6: Orbit of a charged particle in a Penning trap. The three emendations are shown independently.

It is obvious from Eq. (3.17) that the axial motion is decoupled from the radial motion. The later can be solved by considering a complex variable $u = x + iy$. Thus,

$$\ddot{u} + i\omega_c \dot{u} - \frac{\omega_z^2}{2}u = 0. \quad (3.18)$$

Assuming $u = e^{-i\omega t}$, the characteristic frequencies for the radial motion can be given as

$$\omega_{\pm} = \frac{\omega_c}{2} \pm \sqrt{\frac{\omega_c^2}{4} - \frac{\omega_z^2}{2}}. \quad (3.19)$$

The radial motion for the particle is thus given by

$$u = C_+ e^{-i\omega_+ t} + C_- e^{-i\omega_- t}, \quad (3.20)$$

where C_{\pm} are arbitrary complex constants. Transforming back into the Cartesian coordinates one obtains,

$$\begin{bmatrix} x \\ y \end{bmatrix} = \rho_- \begin{bmatrix} \cos(\omega_- t - \phi_-) \\ -\sin(\omega_- t - \phi_-) \end{bmatrix} + \rho_+ \begin{bmatrix} \cos(\omega_+ t - \phi_+) \\ -\sin(\omega_+ t - \phi_+) \end{bmatrix}. \quad (3.21)$$

The two radial motions are known as the reduced cyclotron motion (due to the presence of the quadrupolar electric field) with eigenfrequency ω_+ and the magnetron motion with eigenfrequency ω_- . The magnetron motion is a slow drift motion caused by the $\vec{E} \times \vec{B}$ field. The three eigen motions of an ion confined in a Penning trap are shown in Figure 3.6.

From Eq. (3.19) it is obvious that the two radial frequencies obey the relation

$$\omega_c = \omega_+ + \omega_-. \quad (3.22)$$

This is the most important equation in context of the ISOLTRAP mass spectrometer, since a direct determination of this sum frequency allows to determine the mass of the ion of interest as long as the magnetic field amplitude B and the charge state q is known¹.

3.1.3 Real Penning trap

A real Penning trap deviates from an ideal one in many respects. Trap imperfections lead to shifts in the eigenfrequencies and hence to systematic uncertainties in the mass determination. Knowledge about these imperfections and their influence is therefore essential for a design of the Penning trap mass spectrometer and to understand the possible systematic uncertainties in mass determination. The most important trap imperfections will be briefly described in the following subsections.

Electric field imperfections

Electric field imperfections are the deviations from the pure quadrupolar field as defined in Eq. (3.9). These imperfections occur due to the geometrical imperfections of the trap construction such as the holes in the endcaps for injection and ejection of the ions or from the unavoidable truncation of the electrodes. Changes from the ideal quadrupolar field are generally expressed in terms of a multipole expansion of the trapping potential. Frequency shifts caused by the octupole and dodecapole contributions have been calculated [Bro1986, Bol1990]. For the sum frequency $\omega_c = \omega_+ + \omega_-$, the frequency shift $\Delta\omega_c^{\text{elec}}$ depends on the amplitudes ρ_+ , ρ_- and ρ_z of the reduced cyclotron, the magnetron and the axial motion and is given by

$$\Delta\omega_c^{\text{elec}} = \Omega_c^{\text{elec}} \left[\frac{3}{2} \frac{C_4}{d^2} (\rho_-^2 - \rho_+^2) + \frac{15}{4} \frac{C_6}{d^4} (\rho_z^2 (\rho_-^2 - \rho_+^2) - (\rho_-^4 - \rho_+^4)) \right], \quad (3.23)$$

with

$$\Omega_c^{\text{elec}} = \frac{\omega_-}{1 - \omega_-/\omega_+} \approx \omega_- \approx \frac{U_0/(2d^2)}{B} \quad (3.24)$$

since, in general, $\omega_- \ll \omega_+$ and $\omega_- \approx (U_0/2d^2)/B$. C_4 and C_6 are the coefficients of the octupole and dodecapole components of the electric field, respectively. From Eq. (3.23) and (3.24) it can be seen that the frequency shifts due to electric field imperfections can be minimized by using a trap with a large characteristic dimension d , a small trap potential U_0 and by omitting or correcting higher multipole terms. In addition it can be reduced by small amplitudes of the ion motion.

The frequency shift $\Delta\omega_c^{\text{elec}}$ is practically mass independent because of the mass independence of Ω_c^{elec} . This kind of frequency shift $\Delta\omega \neq f(m)$ always leads to a systematic uncertainty in the mass determination due to the use of a reference mass

¹Measurements with the ISOLTRAP mass spectrometer are only performed on singly charged ions, thus $q = e$.

m_{ref} to calibrate the magnetic field strength B . The relative mass uncertainty of an ion of mass m_x and cyclotron frequency $\omega_{c,x}$ is

$$\frac{\Delta m_x}{m_x} = \frac{\Delta \omega (m_{\text{ref}} - m_x)}{m_x (\omega_{c,x} + \Delta \omega)} \propto m_x - m_{\text{ref}}. \quad (3.25)$$

Therefore it is desired to have mass references as close as possible, mass doublets are the foremost choice but in most cases they are not available or their masses are known with low accuracy. So the mass reference of choice are carbon clusters C_n (with $n = 1, 2, \dots, 10, \dots$) [Bla2002]. The advantages are obvious: A multitude of reference masses all over the nuclear chart are available which are at most six atomic mass units away from any nuclide of interest (see also Section 3.2.6). Thus, any mass dependent systematic uncertainty which increases with the mass difference between the measured and the reference ion is minimized.

Electric field imperfections can also lead to frequency shifts via the induced image charge of the ions on the trap electrodes. This shift scales inversely to the cube of the trap dimension and hence the effect is supposed to be pronounced for a small trap [Dyc1989]. Since $\Delta \omega_+ = -\Delta \omega_-$ no frequency shift will occur in the ISOLTRAP mass measurement procedure which determines the sum frequency $\omega_- + \omega_+$.

Misalignment

A tilt of the electrostatic field axis relative to the magnetic field axis can give rise to a systematic uncertainty in mass determination as well [Bro1986]. This misalignment shifts all eigenfrequencies. For the sum frequency $\omega_- + \omega_+$ the resulting shift $\Delta \omega_c^{\text{tilt}}$ can be calculated [Bol1990] and is found to be mass independent and, for $\Theta \ll 1$, to be proportional to the square of the tilting angle Θ [Bro1986]:

$$\Delta \omega_c^{\text{tilt}} \approx \frac{9}{4} \omega_- (\sin^2 \Theta). \quad (3.26)$$

Again, the frequency shift is mass independent and hence can give rise to a systematic uncertainty as in Eq. (3.25). Therefore the trap has to be aligned very carefully.

Magnetic field instabilities and imperfections

Accurate mass determination demands an excellent magnetic field homogeneity and temporal stability. Commercial superconducting magnets nowadays can provide a homogeneity of $\Delta B/B < 10^{-8}$ over a volume of 1 cm^3 and the available field stability is $(\Delta B/B)/\Delta T < 10^{-8} / \text{h}$. The magnetic field homogeneity can easily be destroyed if materials with high magnetic susceptibility are introduced into the magnetic field. Such materials can be part of the trap itself. Therefore cares are taken and usually oxygen-free high-conductivity copper and glass ceramics are used as trap materials. Nevertheless their susceptibilities are high enough to see noticeable perturbations in the magnetic field.

Frequency shifts occur if the magnetic field is a function of the even powers of the distance from the trap center [Bro1986]. A stored ion then experiences different average magnetic fields for different motional amplitudes. The lowest order inhomogeneity of interest is a magnetic hexapole component. It creates a frequency shift given by

$$\Delta\omega_c^{\text{magn}} \approx \beta_2\omega_c(\rho_z^2 - \rho_-^2), \quad (3.27)$$

where β_2 denotes the relative strength of the hexapole component of the magnetic field. In contrast to the frequency shifts discussed above, this shift is now proportional to the cyclotron frequency of the stored ion and does not give rise to calibration error provided the motional amplitudes are the same for both ion species. Since this can only be achieved within certain limits, it is still important to construct the trap such that the inhomogeneity is smaller than the aimed mass precision.

Magnetic field instability is another point of concern. As reported and discussed by many experiments [Cor1989, Jhe1992, Bol1992a], the field stability is determined by the magnet itself, ambient magnetic field changes, pressure changes in the helium cryostat and temperature changes of the experimental equipment installed in the magnet bore. The demand for the magnetic field stability is defined by the desired mass precision and by the switching time between the cyclotron frequency measurements of the reference ion and the ion of interest. For ISOLTRAP this has been measured for a long time duration and the resultant magnetic field fluctuation $\delta B/B$ is plotted in Figure 3.7, where day/night fluctuations are superposed by a slow drift of $-2.30(3) \times 10^{-8}/\text{h}$ [Kel2003].

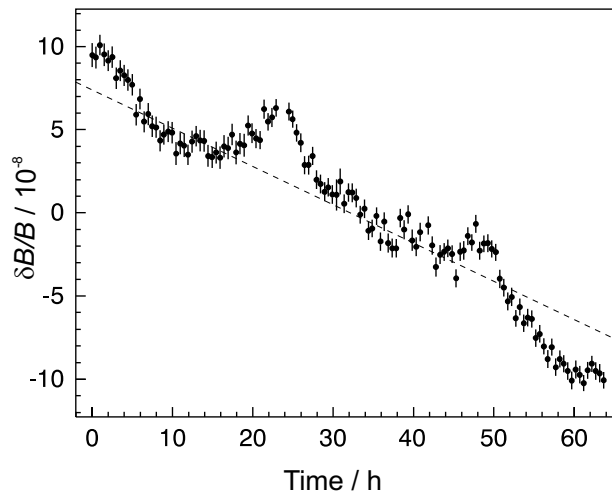


Figure 3.7: Relative change of the magnetic field magnitude in ISOLTRAP’s Precision Trap over a time of more than 60 hours. The steady decrease as well as the superimposed random fluctuations over short time can be observed. The slope of the slow decay is given by the dashed line and is expressed as $\frac{\delta B}{\delta t} \cdot \frac{1}{B} = -2.30(3) \times 10^{-8}/\text{h}$ [Kel2003].

Storage of more than one ion

In the ISOLTRAP experiment the cyclotron frequency is measured for a small number of ions stored at the same time in the trap. This means that the effect of the Coulomb interaction on the ion motion must be taken into account to obtain the proper cyclotron frequency. It has been observed and investigated for both, Paul trap [Jun1987] and Penning trap [Jef1983, Bol1992b, Gab1993]. The effects in a Penning trap will be addressed here.

If the simultaneously stored ions are of the same mass, the driving frequency acts on the q/m center of the stored ion cloud and no frequency shift is observed [Win1975]. It is not the case for stored ions of different species. Such contaminations cause frequency shifts $\Delta\omega_c^{\text{Ch}}$ in the observed resonance. It was found [Bol1992b] that the sign of $\Delta\omega_c^{\text{Ch}}$ depends strongly on the cyclotron frequency difference of the stored species compared to the line-width of the resonances. The shift increases with the total number of stored ions. In case that the unperturbed resonances cannot be resolved, only a single resonance is observed, which is narrower than expected from simple superposition of the individual resonances. The position of the resonance is determined by the average mass of all ions stored in the trap. For large mass differences of the stored ion species, the measured cyclotron frequency of both species shift to lower frequencies. The size of the shift of one species is found to be proportional to the number of stored ions of the other species and vice versa.

A quantitative description of the observed frequency shifts must take into account the coupling of all eigen motions by Coulomb interaction. Until now no general analytical solution has been found for the equation of motion, neither for the Paul trap nor for the Penning trap. Nevertheless, it is possible to confirm the observations qualitatively by a three-dimensional simulation of the motion of simultaneously stored ions [Bol1992b].

In practice, it is therefore essential to have a pure ion sample stored in the trap. If that is not possible, the cyclotron frequency can be extrapolated to a single stored ion in the trap, by analyzing the cyclotron frequencies for different numbers of stored ions [Kel2003] (see Section 3.4.2).

3.1.4 Excitation of the ion motion and the cyclotron resonance detection technique

To measure the cyclotron frequency of a stored ion, to remove unwanted ion species from the trap, or to perform buffer gas cooling in a Penning trap, it is necessary to drive the ion motion with an external oscillating electric field. The effect on the ion motion depends on the multi-polarity and the frequency of the driving radiofrequency (RF) field. At present, for the ISOLTRAP experiment dipolar and quadrupolar driving fields in the radial plane are in use. For this purpose the ring electrode is four-fold segmented in the radial plane, as shown in Figure 3.8.

Dipolar excitation

Figure 3.8 depicts how the RF voltage is applied to the ring segments in order to achieve dipolar excitation of the trapped ions. An oscillating dipolar potential is expressed as

$$U_d = a \frac{U_{d0}}{\rho_0} \cos(\omega_d t - \phi_d) \cdot x, \quad (3.28)$$

where a is a geometric factor taking into account that in the azimuthal plane the shape of the ring electrode segment does not follow the dipolar equipotential lines. This potential gives rise to an electric field

$$\vec{E}_d = -\vec{\nabla} U_d = -a \frac{U_{d0}}{\rho_0} \cos(\omega_d t - \phi_d) \cdot \begin{bmatrix} 1 \\ 0 \\ 0 \end{bmatrix}, \quad (3.29)$$

which adds an inhomogeneous part to the equation of motion given in Eq. (3.17):

$$\begin{bmatrix} \ddot{x} \\ \ddot{y} \\ \ddot{z} \end{bmatrix} - \frac{\omega_z^2}{2} \begin{bmatrix} x \\ y \\ -2z \end{bmatrix} - \omega_c \begin{bmatrix} \dot{y} \\ -\dot{x} \\ 0 \end{bmatrix} = \omega_c \begin{bmatrix} -k_0 \cos(\omega_d t - \phi_d) \\ 0 \\ 0 \end{bmatrix}, \quad (3.30)$$

with

$$k_0 = a \frac{q}{m} \frac{U_{d0}}{\rho_0}. \quad (3.31)$$

Using a similar ansatz as for Eq. (3.17), one can solve the radial part of Eq. (3.30), and the solutions turns out to be similar as Eq. (3.21), but here, the magnetron and cyclotron radii are time dependent:

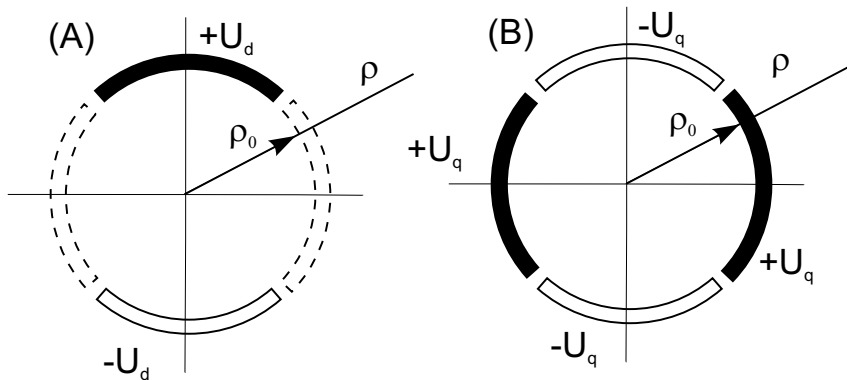


Figure 3.8: Configuration for a dipolar radiofrequency excitation applied to two opposite segments of the ring electrode (A). A quadrupolar radiofrequency excitation applied to four segments of the ring electrode (B).

$$\begin{bmatrix} x \\ y \end{bmatrix} = \rho_-(t) \begin{bmatrix} \cos(\omega_- t - \phi_-) \\ -\sin(\omega_- t - \phi_-) \end{bmatrix} + \rho_+(t) \begin{bmatrix} \cos(\omega_+ t - \phi_+) \\ -\sin(\omega_+ t - \phi_+) \end{bmatrix}. \quad (3.32)$$

For excitations exactly at the magnetron ω_- or the reduced cyclotron ω_+ frequency, the time evolution of the radius of the respective motion is given by

$$\rho_{\pm}(t) = \sqrt{\rho_{\pm}^2(0) + \frac{k_0^2 t^2}{4(\omega_+ - \omega_-)^2} \mp \frac{\rho_{\pm}(0)k_0 t \sin(\phi_d - \phi_{\pm})}{\omega_+ - \omega_-}}. \quad (3.33)$$

A dipolar excitation applied at any of the three eigenfrequencies can excite that motion without affecting the others. This kind of excitation at ω_- and ω_+ frequencies are in use at ISOLTRAP for removing unwanted species from the trap and to enlarge the motional radius.

Quadrupolar excitation

An oscillating quadrupolar potential achieved by the configuration shown in Figure 3.8(B) has the form

$$U_q = a \frac{U_{q_0}}{\rho_0^2} \cos(\omega_q t - \phi_q) \cdot (x^2 - y^2), \quad (3.34)$$

where again a is the geometric factor originating from the shape of the electrode segment. The quadrupolar field due to this potential is given by :

$$\vec{E}_q = -\vec{\nabla} U_q = -2a \frac{U_{q_0}}{\rho_0^2} \cos(\omega_q t - \phi_q) \cdot \begin{bmatrix} x \\ -y \\ 0 \end{bmatrix}. \quad (3.35)$$

The equations of motion become:

$$\begin{bmatrix} \ddot{x} \\ \ddot{y} \\ \ddot{z} \end{bmatrix} - \omega_c \begin{bmatrix} \dot{y} \\ -\dot{x} \\ 0 \end{bmatrix} - \begin{bmatrix} \left(\frac{\omega_z^2}{2} - 2k_0 \cos(\omega_q t - \phi_q) \right) \cdot x \\ \left(\frac{\omega_z^2}{2} + 2k_0 \cos(\omega_q t - \phi_q) \right) \cdot y \\ -\omega_z^2 z \end{bmatrix} = 0, \quad (3.36)$$

where k_0 is now given by

$$k_0 = a \frac{q}{m} \frac{U_{q_0}}{\rho_0^2}. \quad (3.37)$$

Once again the axial motion remains unaffected by the excitation in the azimuthal plane. The radial motions can be combined into a complex equation:

$$\ddot{u} + i\omega_c \dot{u} - \left\{ \frac{\omega_z^2}{2} - 2ik_0 \cos(\omega_q t - \phi_q) \right\} u = 0. \quad (3.38)$$

The solution to the radial equation of motion has a similar form as in the case of the dipolar excitation [see Eq. (3.32)], but now, the temporal dependence of the radii is different. If the frequency of the exciting RF field is exactly set to $\omega_+ + \omega_-$, the radial amplitude evolves as

$$\rho_{\pm}(t) = \rho_{\pm}(0) \cos\left(\frac{\omega_{\text{conv}}}{2}t\right) \mp \rho_{\mp}(0) \sin\left(\frac{\omega_{\text{conv}}}{2}t\right) \cos(\phi_q - \phi_+ - \phi_-), \quad (3.39)$$

where

$$\omega_{\text{conv}} = \frac{k_0}{2(\omega_+ - \omega_-)}. \quad (3.40)$$

This type of excitation is also known as sideband excitation. Furthermore, if the phase difference between the excitation and the radial motion $\phi_q - \phi_- - \phi_+$ is exactly equal to π , the radial evolution is simplified to

$$\rho_{\pm}(t) = \rho_{\pm}(0) \cos\left(\frac{\omega_{\text{conv}}}{2}t\right) \pm \rho_{\mp}(0) \sin\left(\frac{\omega_{\text{conv}}}{2}t\right). \quad (3.41)$$

This shows that the two radial motions are coupled by an excitation at their sum frequency. There is a continuous conversion at a frequency ω_{conv} between the two radial motions. A complete conversion from one motion to the other therefore takes $T_{\text{conv}} = \pi/\omega_{\text{conv}}$. Figure 3.9 shows this conversion as a function of time.

Viscous damping in a Penning trap

In a gas filled Penning trap the ions lose their kinetic energy due to collision with the buffer gas atoms. This damping force can be approximated as a velocity dependent damping for simple analytical formulation as in Eq. (3.7):

$$\vec{F} = \delta \cdot \dot{\vec{x}}. \quad (3.42)$$

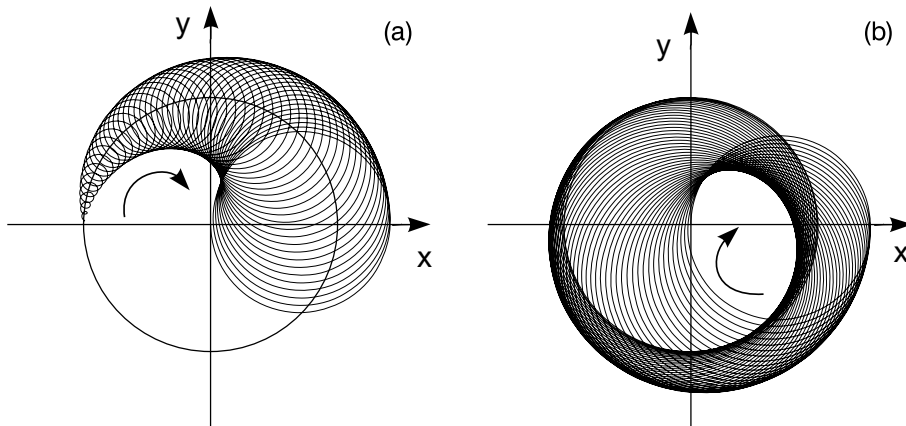


Figure 3.9: Radial motion with a quadrupolar excitation at $\omega_q = \omega_c$. The motion starts with pure magnetron motion (a), indicated by the circle, and converts fully to cyclotron motion (b) in time T_{conv} .

The equations of motion after adding this new force become

$$\begin{bmatrix} \ddot{x} \\ \ddot{y} \\ \ddot{z} \end{bmatrix} - \frac{\omega_z^2}{2} \begin{bmatrix} x \\ y \\ -2z \end{bmatrix} - \begin{bmatrix} \omega_c \dot{y} - \frac{\delta}{m} \dot{x} \\ -\omega_c \dot{x} - \frac{\delta}{m} \dot{y} \\ -\frac{\delta}{m} \dot{z} \end{bmatrix} = 0. \quad (3.43)$$

The axial motion is still independent of the radial motion. It can be described as a damped oscillator

$$z = A'_z e^{-(\delta/2m)t} \cos(\omega'_z t - \phi'_z), \quad (3.44)$$

where

$$\omega'_z = \sqrt{\omega_z^2 - \left(\frac{\delta}{2m}\right)^2}. \quad (3.45)$$

The solution of the radial part can be obtained by combining the two equations into one complex equation as in Eq. (3.38) and with the ansatz $u = e^{-i(\omega t - \alpha)}$. One obtains in Cartesian coordinates:

$$\begin{bmatrix} x \\ y \end{bmatrix} = \rho_- e^{\alpha_- t} \begin{bmatrix} \cos(\omega_- t - \phi_-) \\ -\sin(\omega_- t - \phi_-) \end{bmatrix} + \rho_+ e^{\alpha_+ t} \begin{bmatrix} \cos(\omega_+ t - \phi_+) \\ -\sin(\omega_+ t - \phi_+) \end{bmatrix}, \quad (3.46)$$

where

$$\omega'_\pm = \omega_\pm \pm \Delta\omega, \quad \Delta\omega = \frac{1}{16} \cdot \left(\frac{\delta}{m}\right)^2 \cdot \frac{8\omega_z^2 + (\frac{\delta}{m})^2}{(\omega_c^2 - 2\omega_z^2)^{\frac{3}{2}}}. \quad (3.47)$$

The radial motion in the presence of a damping force is still composed of two circular motions. However, compared to the undamped case, the frequencies are now shifted down and up, respectively, by $\Delta\omega$ from the magnetron ω_- and the reduced cyclotron ω_+ frequencies. These frequency shifts are very small and can be neglected in most cases. In addition, since the shifts are equal in magnitude but opposite in direction, their sum and hence ω_c remains unchanged.

The radii of the motions change exponentially with time constants α_\pm given by,

$$\alpha_\pm = -\frac{\delta}{2m} \left\{ 1 \pm \left(1 + \frac{1}{8} \cdot \frac{8\omega_z^2 + (\frac{\delta}{m})^2}{\omega_c^2 - 2\omega_z^2} \right) \right\}. \quad (3.48)$$

While the radius of the reduced cyclotron motion decreases with a time constant $\alpha_+ \approx -\delta/m$, the magnetron radius increases with a much shorter time constant $\alpha_- \approx (\delta/2m) \cdot (\omega_z/\omega_c)^2$ as shown in Figure 3.10(a). Thus the particle will be lost after a certain time due to the increase in the magnetron radius. This can be avoided by coupling the two radial motions. Hence, both radii will decrease as shown in Figure 3.10(b).

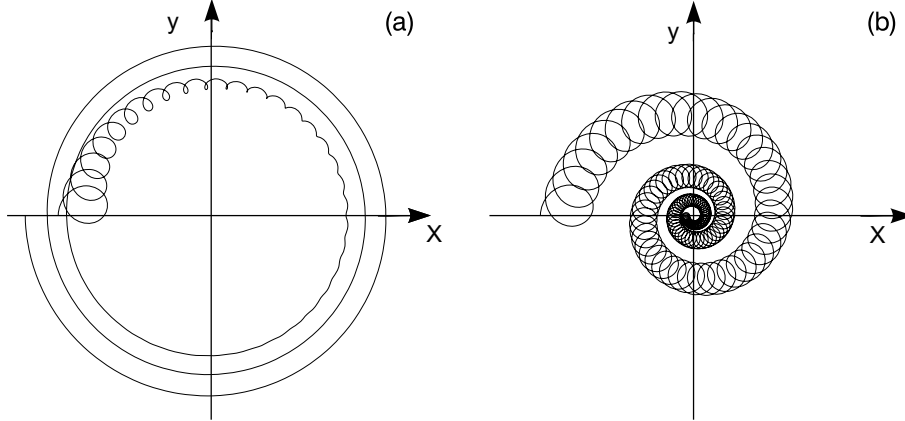


Figure 3.10: Radial motion of an ion in a buffer gas filled Penning trap, *i.e.* under the influence of a damping force without (left) and with strong (right) quadrupolar excitation. For details see text.

Mass-selective buffer gas centering

As discussed before, the magnetron radii of all ions independent of their masses increase exponentially in the presence of buffer gas. After a certain time they are lost, while hitting the trap electrodes. By applying a quadrupolar excitation as described in Section 3.1.4 at a frequency $\omega_c = \omega_- + \omega_+$ for the ion of interest, one can continuously convert the magnetron motion into reduced cyclotron motion, resulting in an overall centering of the ions of interest [Sav1991], as shown in Figure 3.10. By this, the ions can be cooled down to the temperature of the buffer gas.

Time-of-flight ion cyclotron resonance technique

The principle of the time-of-flight (TOF) ion cyclotron resonance detection was originally proposed by Bloch [Blo1953] and first applied for mass measurements by Gräff *et al.* [Grä1980]. Though it is a destructive detection method, its advantage is obvious: It can be used for a single or a very low number of stored ions in the trap. This is particularly of advantage for radioactive ions where decay losses anyhow limits the storage time in the trap. Figure 3.11 shows the principle of the time-of-flight cyclotron resonance detection system.

Ions captured in the trap are first excited by an azimuthal dipolar excitation at their magnetron frequency, which leads to an increase of their magnetron radius. An azimuthal quadrupolar RF excitation is then applied for a time period of $T_q = \pi/\omega_{\text{conv}}$. In the case of $\omega_q = \omega_c$, the magnetron motion is fully converted to cyclotron motion as discussed in Section 3.1.4. Finally the cyclotron radius becomes equal to the initial magnetron radius. Since the reduced cyclotron frequency is much higher than the magnetron frequency, this conversion is accompanied by a fast increase in the radial energy E_r :

$$E_r \propto \omega_+^2 \rho_0^2 - \omega_-^2 \rho_0^2 \approx \omega_+^2 \rho_0^2. \quad (3.49)$$

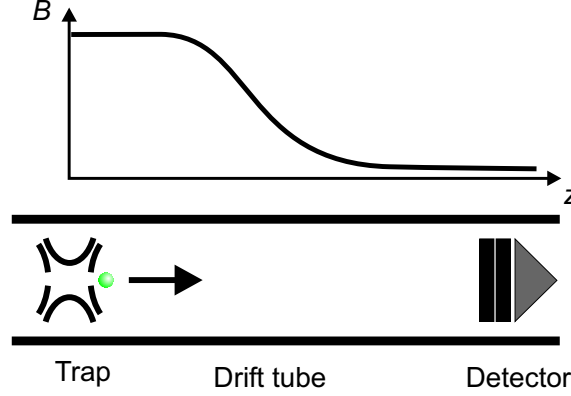


Figure 3.11: Principle of the time-of-flight ion cyclotron resonance detection technique.

Off-resonance ($\omega_q \neq \omega_c$), the conversion is not complete and hence the radial energy gain smaller. The exact functional form of the energy gain depends on the envelope of the excitation signal. For a rectangular envelope, *i.e.*, the quadrupolar excitation is only switched on for a time T_q , the final radial kinetic energy is of the form [Kön1995b] (see Figure 3.12 left):

$$E_r = \frac{\sin^2(\omega_b T_q)}{\omega_b^2}, \quad (3.50)$$

with

$$\omega_b = \frac{1}{2} \sqrt{(\omega_q - \omega_c)^2 + (\omega_{\text{conv}}/2)^2}. \quad (3.51)$$

After this sequence of excitations, the ions are ejected from the trap, fly through a drift section in the gradient of the magnetic field and get detected as shown in Figure 3.11. The on-axis ion detector is installed about 1.2 m upstream where the magnetic field amplitude is already reduced by three orders of magnitude. The magnetic moment that the ions acquire due to their radial motion, interacts with the magnetic field gradient and hence experiences an axial force

$$\vec{F} = -\vec{\mu}(\vec{\nabla} \cdot \vec{B}) = -\frac{E_r}{B} \frac{\partial B}{\partial z} \hat{z}. \quad (3.52)$$

This force leads to a maximum reduction in the time-of-flight from the trap to the detector under resonance condition $\omega_q = \omega_c$.

The change in the time of flight from the trap center $z = 0$ to the detector $z = z_1$ for a given radial energy E_r can be calculated by

$$T_{\text{tot}}(\omega_q) = \int_0^{z_1} \sqrt{\frac{m}{2(E_0 - qU(z) - \mu(\omega_q)B(z))}} dz, \quad (3.53)$$

where E_0 is the initial axial kinetic energy of the ion, $U(z)$ is the electrostatic potential difference along the flight path and $B(z)$ is that for the magnetic field.

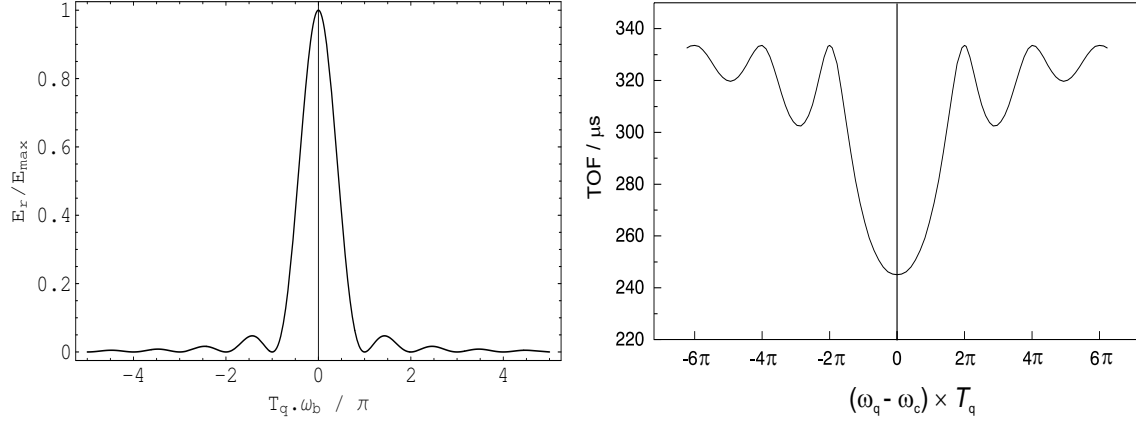


Figure 3.12: Left: Radial energy gain of the ion motion in the case of quadrupolar excitation near ω_c as a function of the detuning $\omega_b = f(\omega_q - \omega_c)$ as in Eq. (3.50). Right: The theoretical line shape of the mean time of flight in the case of quadrupolar excitation near ω_c as a function of the detuning $\Delta\omega = \omega_q - \omega_c$. The central frequency is the true cyclotron frequency for a given mass m .

A scan of the quadrupolar excitation frequency ω_q thus produces a characteristic time-of-flight resonance. The theoretically expected line shape for such a resonance with rectangular envelope is well understood [Kön1995b] and is as represented in Figure 3.12(right).

It follows from Eq. (3.49), (3.50), and (3.53) that the depth of the main peak, the so called time-of-flight effect, is dependent on the initial magnetron radius ρ_0 . The TOF effect is a characteristic property of a cyclotron resonance and is defined as: TOF-effect in % = $100 \cdot (1 - TOF_{\nu_c}/TOF_{\text{base}})$ where TOF_{base} means the time-of-flight “baseline” far from resonance where the sideband oscillations are negligible. The TOF-effect is a measure for the radial energy gain of the ions: A higher gain leads to a greater acceleration after ejection, a shorter TOF, and consequently a bigger TOF-effect. The completeness of the conversion from pure magnetron to pure cyclotron motion depends on the amplitude U_{q_0} and on the time duration T_q of the excitation. The line width of the centroid is inversely proportional to T_q . The resolving power $R = \nu_q \cdot T_q$ is therefore essentially dependent on the excitation time.

3.2 Experimental setup of ISOLTRAP

The ISOLTRAP mass spectrometer was originally installed at the on-line mass separator ISOLDE-2 at CERN, Geneva. In 1992 it was moved to its present place at ISOLDE which can deliver a variety of isotopes of different elements. Since the last major status report of the ISOLTRAP setup in 1996 by Bollen *et al.* [Bol1996], there have been many changes in the setup as well as its performance. A photograph of the presently installed setup is shown in Figure 3.13. Figure 3.14 presents the technical design of it up to the spectrometer section described in the following.

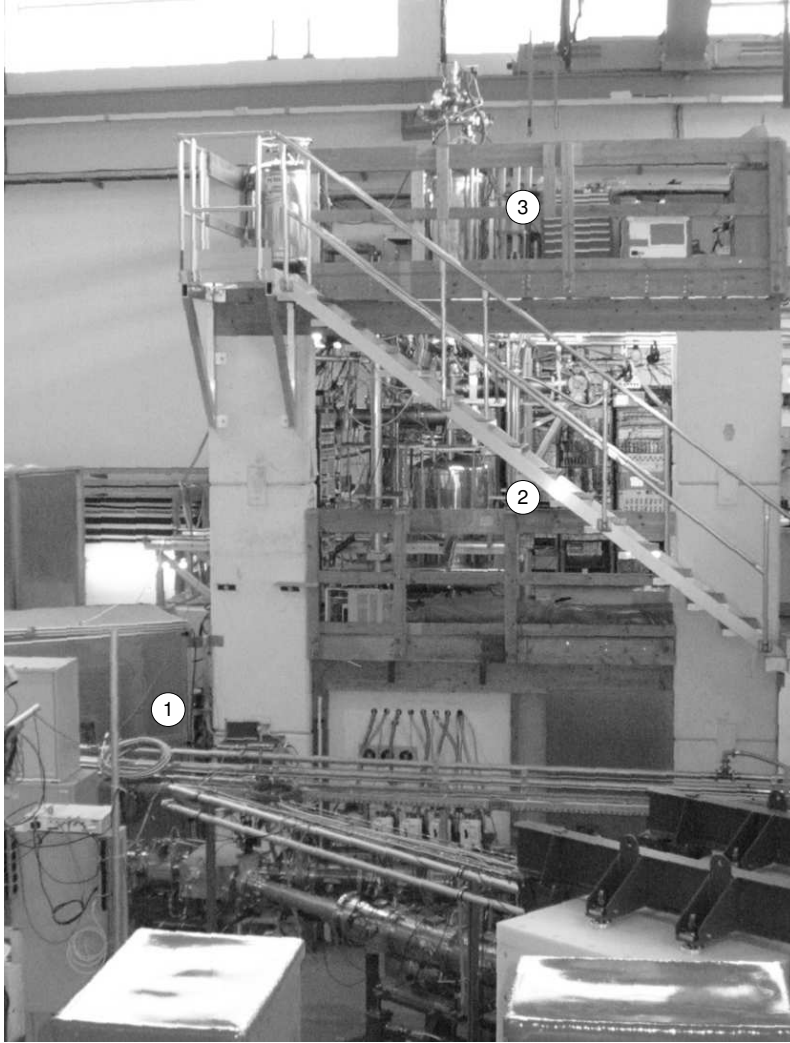
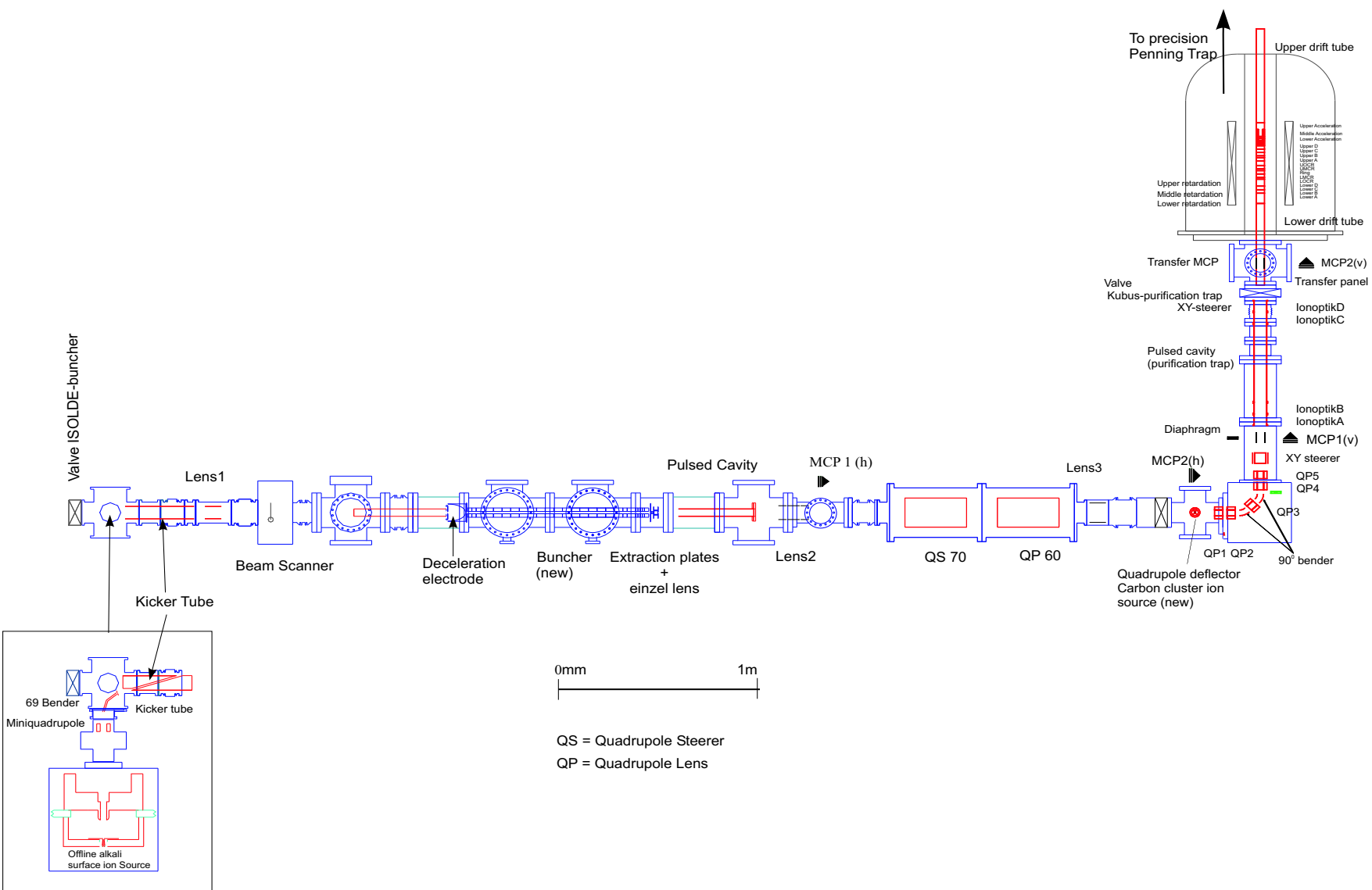


Figure 3.13: A photograph of the ISOLTRAP setup. The high voltage cage for the radiofrequency quadrupole cooler and buncher (1), magnets for the Purification Penning Trap (2), and the Precision Penning Trap (2) are visible.

3.2.1 Production of radioactive beams at ISOLDE

Radionuclides as presented in Figure 2.5, are produced at ISOLDE by bombarding a thick target (*e.g.* UC_2) with 1.4-GeV protons from the CERN proton synchrotron booster (3×10^{13} protons/pulse) [Kug2000]. Radioactive products produced by fission, fragmentation or spallation diffuse out of the target and get ionized by surface, plasma or laser ionization. The laser ion source provides the strongest suppression of isobaric contaminations [Kös2003]. The ions are then accelerated to 60 keV, mass separated by magnetic sector fields and delivered via transfer beam lines to different experiments like ISOLTRAP as shown in Figure 3.15. There are two target stations and two mass separators working in parallel, the General Purpose Separator (GPS) with a mass resolving power of $R \sim 1000$ and the High Resolution Separator (HRS) with $R \sim 5000$. The HRS was originally designed for $R \sim 30\,000$ but it has hysteresis problems. ISOLDE can provide at present 700 radionuclides of



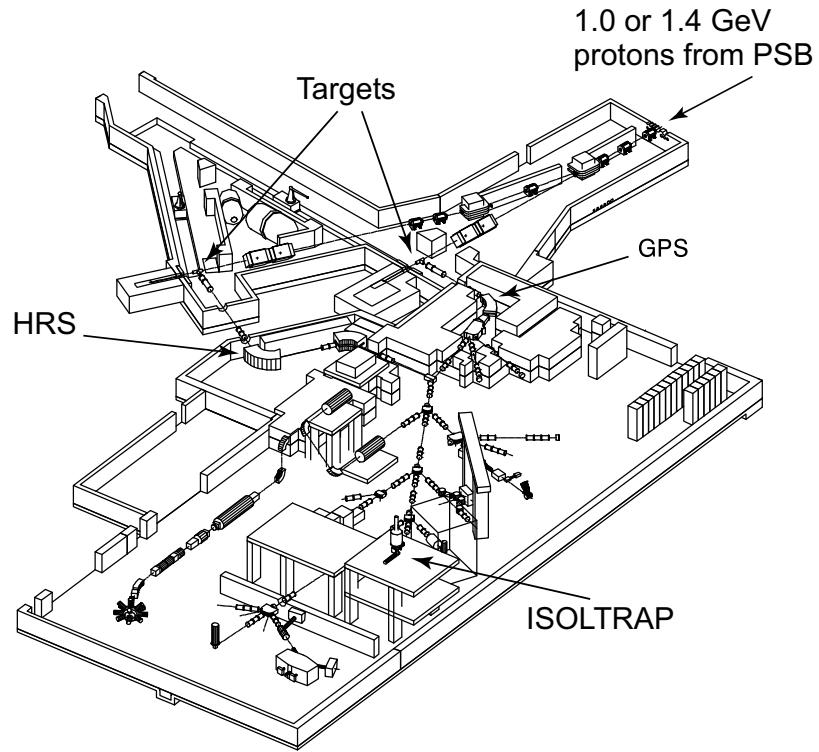


Figure 3.15: The ISOLDE hall with different beam lines heading towards different experiments. PSB denotes Proton Synchrotron Booster at CERN.

about 70 different elements summarized in Figure 2.5.



Figure 3.16: A photograph of the radiofrequency cooler and buncher of ISOLTRAP.

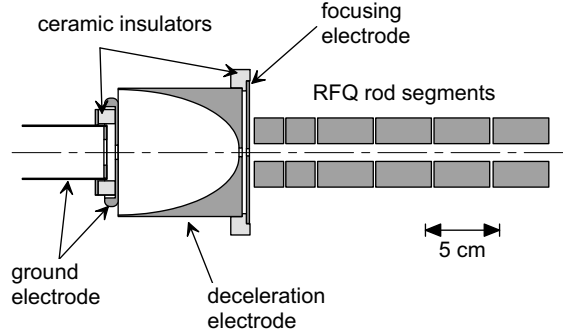


Figure 3.17: The specially designed “egg-cup”-shaped deceleration electrode to match the high emittance of the ISOLDE beam and the first rod segments of the radiofrequency quadrupole cooler and buncher.

3.2.2 ISOLTRAP RFQ cooler and buncher

A linear RFQ cooler and buncher shown in Figure 3.16 has been developed and is now in use at the ISOLTRAP experiment for beam emittance improvement and bunching

Table 3.1: Typical operational parameters of the RFQ cooler and buncher for ions in the mass ranges $A \approx 39$ and $A \approx 133$ [Her2001]. * Electrode voltages are given relative to the HV platform voltage of 30 kV or 60 kV which corresponds to the potential of the ISOLDE ion source. The name of the electrodes are as shown in Figure 3.17 and Figure 3.14.

Parameter		Value	Value	Unit
helium pressure in buncher P_{He}			$\sim 10^{-3}$	mbar
RF frequency $\nu_{\text{RF}} = \omega_{\text{RF}}/2\pi$			990	kHz
RF amplitude U_{RF}	for $A \approx 133$		135	V
	for $A \approx 39$		97	V
cooling time T_{cool}	for $A \approx 133$		10	ms
	for $A \approx 39$		5	ms
cage voltage U_{HV}		30 000	60 000	V
deceleration electrode*		-1350	-3000	V
focusing electrode*		-230	-180	V
quadrupole rod segment*	# 1		-60	V
	# 2		-40	V
	# 3		-25	V
	# 4 to # 22		-10 to -14	V
	# 23 (accumulation)		-16.5	V
	# 23 (ejection)		+2	V
	# 24, # 25		-17.8	V
	# 26 (accumulation)		0	V
	# 26 (ejection)		-70	V
plates of the extraction system*			-240	V
einzel lens system*			-95	V
pulsed cavity*			-2740	V

Table 3.2: Performance of the RFQ cooler and buncher of ISOLTRAP.

Parameters	Values
Accumulation time	0.001 - 1000 ms
Cooling time	2 ... 20 ms
Transversal emittance	2π mm·mrad at 60 keV
Longitudinal emittance	10 eV μ s
Efficiency	12-15% for Xe isotopes

of the ISOLDE DC beam. It has been discussed in detail in [Her2001, Kel2002]. Here, only the setup and its present performance will be discussed.

The 60 keV energy ISOLDE beam with transversal emittance of up to 35π mm·mrad is first decelerated electrostatically by a specially designed egg-cup shaped electrode (see Figure 3.17) to achieve a theoretical capture efficiency of 35% into the RFQ structure situated in a high-voltage platform of 60 kV [Her2001]. The emittance of the ISOLDE beam is improved by buffer gas cooling ($P_{\text{He}} \approx 5 \times 10^{-3}$ mbar) inside the cooler and buncher. The voltages applied to the electrodes create a trapping potential as shown in Figure 3.2. The cooled ion bunch is extracted after an accumulation time of a few ms by switching the last electrodes. Beam optimization is possible via a einzel lens system and a X-Y steerer (see Figure 3.14). The cooled ion bunch is ejected from the 60 kV RFQ with a temporal width of less than 1μ s and guided through a pulsed drift tube ($l = 380$ mm) located at 57.3 kV in which the potential is lowered to ground (see Figure 3.18). The ions remain with a kinetic energy of 2.7 keV. Before the ions enter the first Penning trap the energy is reduced again in a second pulsed drift tube to about 100 eV. The normal operational parameters for the RFQ cooler and buncher are given in Table 3.1. Its performance is tabulated in Table 3.2 [Her2001].

The cooling time mentioned in Table 3.2 refers to the time needed to bring the ion cloud inside the RFQ to thermal equilibrium with the buffer gas at room temperature. The accumulation time can be varied depending on the half-life, the production rate, and the release of the ions from the ISOLDE target.

3.2.3 Ion transport between the RFQ cooler and buncher and the Purification Penning Trap

The ion transport elements that are in use to transfer the ion bunches from the RFQ cooler and buncher to the Purification Trap are shown schematically in Figure 3.14. In order to have mass-independent transport optics it was decided at ISOLTRAP to have only electrostatic ion optical elements. The cooled ion bunch is extracted by a set of electrodes used as einzel lens and as XY-steerer. The buncher including the specially designed entrance and the extraction electrodes are placed in a high voltage cage at 60 kV. The ion bunches thus extracted are accelerated towards the ground potential with 60 keV kinetic energy and are pulsed down to 2.7 keV as mentioned in Section 3.2.2. The ion bunches as shown in Figure 3.14 are then guided by two einzel lens systems (Lens2 and Lens3), three electric quadrupoles (QP60, QP1, QP2)

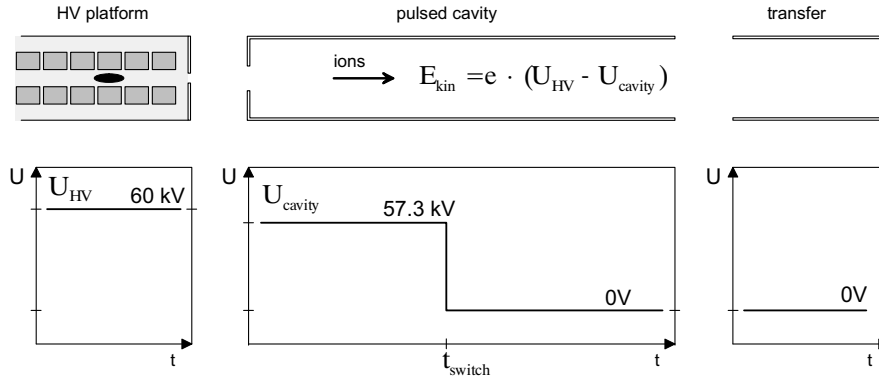


Figure 3.18: The elevator principle to electrostatically lower the beam energy of the ion bunches extracted from the radiofrequency quadrupole cooler and buncher at 60 kV [Her2001].

and one XY-steerer (QS70). Before entering the Purification Trap the ion beam is 90° deflected towards the vertical direction. Two meters downstream from the Purification Trap a carbon cluster laser ion source with a set of lenses and deflectors just before the quadrupole QP4 was temporarily mounted in order to determine the mass accuracy achieved by ISOLTRAP. At that time the bender was removed. The newly designed carbon cluster laser ion source is mounted perpendicular to the beamline at the position of MCP2(h).

The 90° deflector is composed of two electrostatic electrodes (split in two parts) for bending and one quadrupole (QP3) (inserted between the two parts of the 90° deflector) for focusing of the ion bunch. From here on, the ISOLTRAP beam line continues in the vertical direction with two quadrupoles (QP4 and QP5), two XY-steerers, four lenses (Ionoptik A,B,C,D), one drift tube (Lower drift tube), and three retardation electrodes (lower, central and upper) until the lower endcap electrode (Lower endcap A) of the Purification Penning Trap (see Figure 3.14). This section contains another pulse cavity which lowers the ion energy from 2.5 keV to about 100 eV.

3.2.4 The Purification Penning Trap

The second trap of the ISOLTRAP setup is the Purification Penning Trap which is situated in the vertical beam line within a superconducting magnet of 4.7 T field amplitude (Oxford Instruments, System 200/130), as shown in Figure 3.14. It is a cylindrical Penning trap where the ideal quadrupolar electric potential is achieved by the use of correction electrodes apart from the ring and the endcap electrodes. A sketch and a photograph of the trap electrodes is given in Figure 3.19. A nested potential well is formed by applying proper DC voltages to its 13 cylindrical segments [Bec1997, RH1997]. The outer shape of this trap is optimized to capture ion bunches of several 10 eV kinetic energy, while the central part is carefully shaped to achieve a quadrupolar potential over the largest possible volume. This and a large inner trap radius of 17.5 mm allow for the acceptance of a wide incoming ion bunch

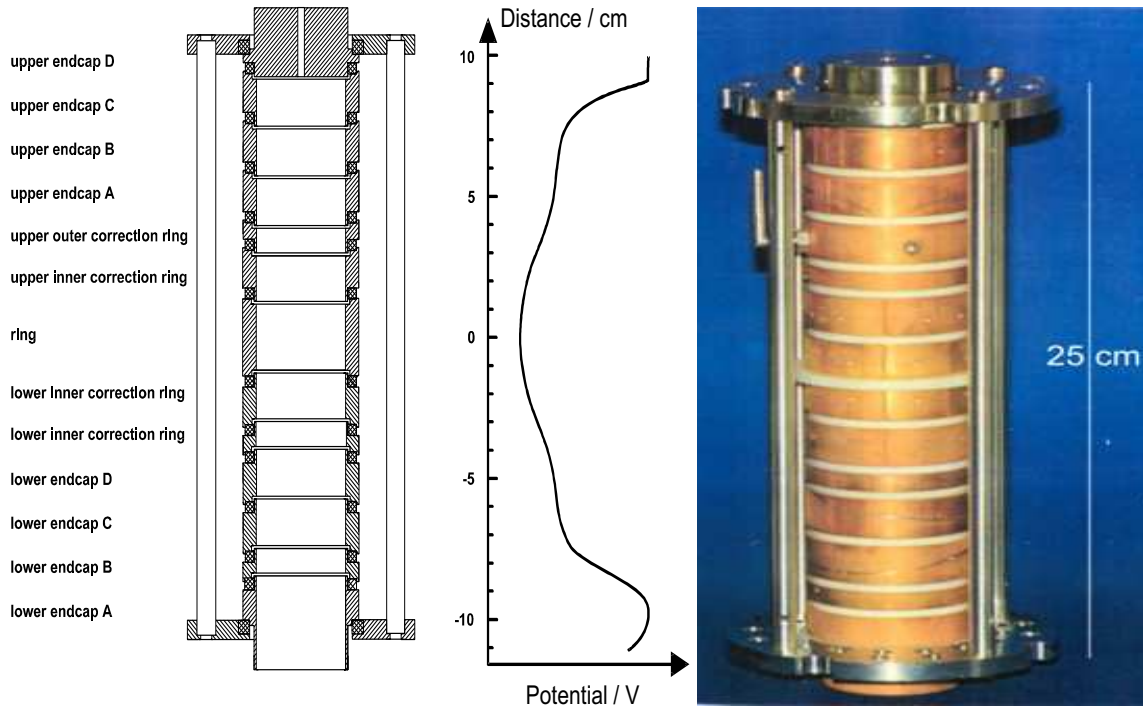


Figure 3.19: Left: Sketch of the cylindrical Purification Penning Trap of ISOLTRAP including the shape of the nested trapping potential along the magnetic field axis. Right: A photograph showing the trap electrodes and support structure of the trap.

and to cool and store more than 10^3 ions at a time. The ring electrode is segmented into four segments in order to apply a quadrupolar RF field for excitation of the ion's radial motion. The mass selective buffer gas cooling technique [Sav1991] as described in Section 3.1.4 is applied here at a helium buffer gas pressure of 10^{-3} - 10^{-4} mbar. A mass resolving power in the order of 10^4 to 10^5 [RH1997] is routinely achieved. The trap parameters are listed in Table 3.3. Two apertures of 3 mm diameter on either end of the trap allow for proper alignment of the trap axis to the magnetic field axis. They also serve for differential pumping between the trap region and either side of the beam line. After isobaric cleaning in the Purification Trap, which lasts between 30 ms and several 100 ms depending on the required resolving power and the half-life of the radionuclide under investigation, the purified ion bunch is transported to the Precision Penning Trap.

Space charge effect

As discussed in Section 3.1.3, due to the Coulomb interaction between two different ion species trapped simultaneously in the trap, the cyclotron frequency shifts. This shift is pronounced with larger number of ions. Such effects have been investigated at the Purification Trap of ISOLTRAP for ^{39}K and ^{41}K ions [Sch2004b] provided by the off-line alkaline surface ion source which will be discussed later.

Three different accumulation times ($T_{\text{accu}} = 10, 50, \text{ and } 100 \text{ ms}$) for the DC beam

Table 3.3: The dimensions, static and dynamic parameters for the Purification Penning Trap under normal trapping/ejection condition. The distance between neighboring trap electrodes is 1 mm.

Element	Length /mm	Radius /mm	Voltage /V
Lower endcap A	36.0	20.0	+88.5/+10
Lower endcap B	9.0	20.0	+14/+20
Lower endcap C	17.0	20.0	+10/+20
Lower endcap D	17.0	20.0	+10/+20
Lower outer correction ring	9.0	20.0	+3.5/+5.2
Lower inner correction ring	16.6	20.0	-6.6/+1.5
Ring electrode	23.8	20.0	-10.0/-10.0
Upper inner correction ring	16.6	20.0	-6.6/-19.6
Upper outer correction ring	9.0	20.0	+3.5/-24.7
Upper endcap A	17.0	20.0	+10.0/-30.0
Upper endcap B	17.0	20.0	+10.0/-39.0
Upper endcap C	17.0	20.0	+10.5/-45.0
Upper endcap D	25.0	1.5	+100.0/-50.0
Characteristic trap dimension d			31.7 mm
Magnetic field			
Field strength at the trap center			4.7 T
Relative homogeneity			$< 10^{-7}/\text{cm}^3$
Relative stability			$< 10^{-8}/\text{h}$
Vacuum /mbar			
Without buffer gas			5×10^{-8}
With buffer gas (He)			$10^{-3} - 10^{-4}$
Typical eigenfrequencies for an ion with mass number $A = 100$			
ν_+			728 kHz
ν_-			0.3 kHz
ν_z			21 kHz

from the ion source was chosen, thereby varying the number of simultaneously stored ions. The natural abundance of ^{39}K is 93% while the rest is that of ^{41}K . Cooling resonances for ^{41}K obtained for different accumulation times are plotted in Figure 3.20. For the short accumulation time (10 ms) the resonance is unaffected since the mass selective buffer gas centering removes the more abundant $^{39}\text{K}^+$ from the trap. This is not the case for longer accumulation times when the trapped unwanted $^{39}\text{K}^+$ ions produce a sizeable space charge effect. The cooling resonance for $^{41}\text{K}^+$ then splits into two resonances (see Figure 3.20 (b) and (c)): one with narrow line-width on the high frequency side and the other with broad line-width on the low frequency side. Figure 3.20 (d) shows that an additionally applied dipolar cleaning at the reduced cyclotron frequency of $^{39}\text{K}^+$ allows to regain the single cooling resonance at the proper frequency for $^{41}\text{K}^+$ even at long accumulation times of 50 ms.

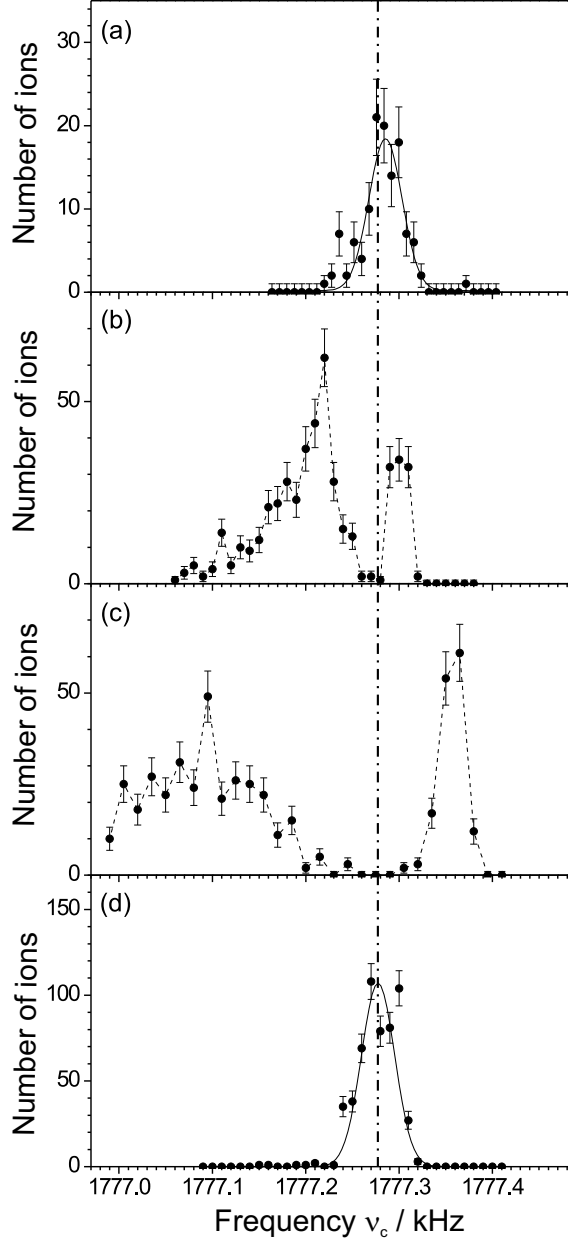


Figure 3.20: Cooling resonances for $^{41}\text{K}^+$ with 10 ms (a), 50 ms (b), and 100 ms (c) accumulation times. The same cooling resonance as in (b) but with an additionally applied dipolar cleaning for $^{39}\text{K}^+$ (d).

3.2.5 The mass spectrometer section

The spectrometer section of ISOLTRAP consists of three parts. An ion transport system from the Purification Penning Trap to the Precision Penning Trap, the Precision Penning Trap itself and an ion drift part from the trap to the detector situated outside the magnetic field. Figure 3.21 gives an overview of the ion optics as well as the vacuum system of this section.

A warm bore superconducting magnet (OXFORD 250/89) with a bore diameter

of 89 mm provides a magnetic field of 5.9 T for the Precision Trap [Bol1996]. It is equipped with superconducting shim coils in order to achieve a homogeneity of $\delta B/B < 10^{-7}$ over a volume of 1 cm^3 . The specified temporal stability is 10^{-8} per hour. It has also been measured recently at ISOLTRAP and the results will be discussed in the next section.

Three vacuum chambers constitute the ion optical enclosure for the spectrometer section [Bol1996]: one below the magnet, a tube holding the Precision Trap inside the bore of the magnet, and the detector chamber placed above the magnet. The chambers are connected with bellows in order to ease the alignment. All vacuum parts are made of stainless steel. The tube inside the magnet bore is made of material with low susceptibility and no magnetic enclosures. This tube, which is precisely machined inside, serves as an optical bench for all ion optical elements placed inside it. The parts are mounted on 1 cm thick discs made of OFHC copper, which themselves fit into the tube within $\pm 0.05 \text{ mm}$ and hence assures good alignment of the optics. The tube itself is mounted in a cardanic holder (CH) on both ends. Micrometer screws allow for a precise and reproducible positioning inside the bore of the magnet. An ultra-high vacuum of $P < 10^{-8} \text{ mbar}$ is achieved with turbomolecular

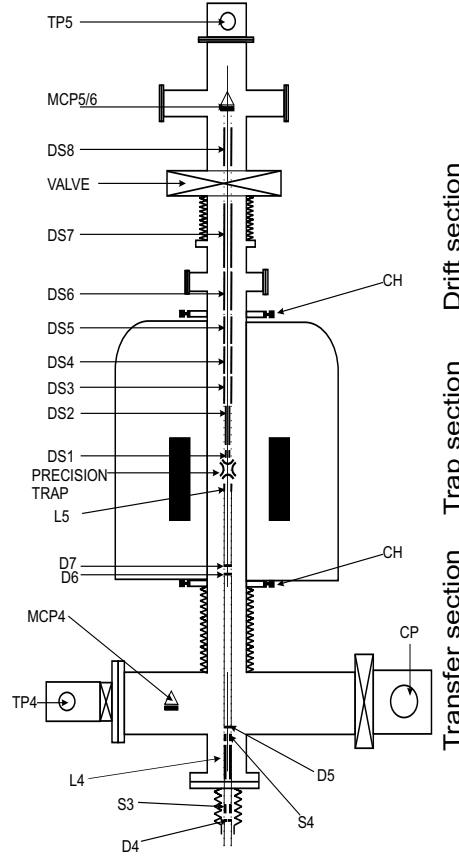


Figure 3.21: Layout of the spectrometer section of ISOLTRAP comprised of a transfer section, the Precision Penning Trap, and a time-of-flight drift section. CH denotes cardanic holder, CP cryopump, D adjustable diaphragms, DS electrostatic elements, L lens, MCP Micro Channel Plate, S steerers, and TP turbo pumps.

pumps at both, the lower (TP4) and the detector chamber (TP5), and an additional cryopump (CP) at the lower chamber.

An alignment of the vacuum tube with respect to the magnetic field axis was performed before the trap and all other ion optical elements were placed into it. It was performed with a setup consisting of an electron gun, pin holes, and a number of diaphragms, all mounted on narrow-tolerance close fitting discs to the vacuum tube. The electron gun, which is a current-heated filament with 0.2 mm pin holes on either side, was aligned with the tube axis. Two detector assemblies, each consists of a 0.4 mm pinhole in the front and electrical ground isolated plate on the back, were placed on the axis of the tube about 25 cm away on either direction of the electron gun. The whole assembly was inserted into the tube such that the electron gun sits in the center of the magnetic field. The electrons thus produced are guided by the magnetic field on either side and by carefully positioning the tube with respect to the bore of the magnet it was possible to have all the electrons completely passing through the pinholes of the detectors. From the dimensions of the system it follows, that the tilting angle in degrees of the tube with respect to the magnetic field axis is as small as $\theta \leq 1 \times 10^{-3}$ [Bol1996]. Considering the present ISOLTRAP Precision Penning Trap parameters this tilting angle can lead to a maximum frequency shift of $\Delta\nu^{\text{tilt}} = \Delta\omega^{\text{tilt}}/(2\pi) < 2$ mHz [Bol1996]. This results in a maximum relative calibration error for $A = 100$ of less than 2×10^{-9} . A final shimming was done after the tube was aligned in order to correct for the inhomogeneities introduced by the tube itself.

Ion transfer section between the two Penning traps

The purpose of this section [Bol1996] is to accept the ion bunch prepared and delivered by the Purification Trap and to transport it to the Precision Trap. The ion optical system (see Figure 3.21) consists of four slits (D4-D7), two sets of deflectors (S3,S4) placed in the low magnetic field region, a set of retardation electrodes (L5) in front of the trap, and an einzel lens (L4). A segmented micro-channel-plate detector (MCP4) in front of the Precision Trap helps to monitor the transfer of the bunch.

This transfer section is important in terms of proper and efficient injection into the high magnetic field. Improperly injected ions pick-up high radial energy while passing through the magnetic field gradient of the superconducting magnet. In extreme case they get back reflected by the high magnetic field. This phenomenon is known as the magnetic mirror effect. Since the cyclotron resonance detection scheme relies on the proper conversion of the resonantly increased radial energy to axial energy, it is essential to keep the initial radial energy during injection as small as possible. Calculated ion trajectories for different injection conditions, *i.e.* different foci and focal strengths show that the best injection focus lies 20 cm below the center of the magnetic field [Bol1996]. Under this condition practically no radial energy is picked up while the ions pass into the high magnetic field region. To achieve this in reality the einzel lens system and the set of steerers are used.

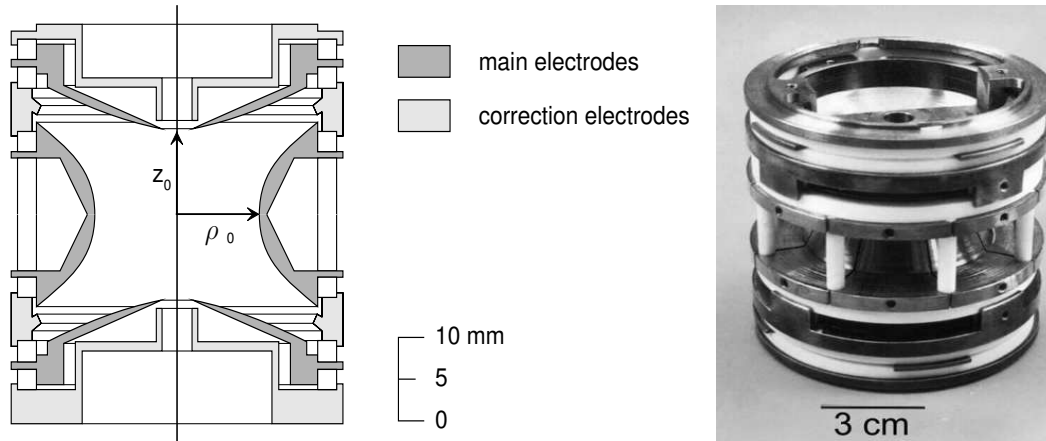


Figure 3.22: Left: The to-the-scale drawing of the ISOLTRAP Precision Penning Trap. Correction elements are drawn in light grey, main electrodes in dark grey. Right: A photograph of it.

The Precision Penning Trap

This trap has been designed to have minimum electric and magnetic field imperfections over a large volume [Bol1996]. This is essential since the cyclotron resonance detection scheme needs to have the ions prepared at large radii in the order of $0.7 - 1$ mm. The choice was a highly compensated hyperbolic trap which offers the best compromise between a perfect field and a desirable trap size. Figure 3.22 shows the cross sectional view as well as a photograph of the trap, while its important parameters and dimensions are tabulated in Table 3.4.

Deviations from the ideal quadrupolar field are compensated by the correction electrodes installed between the endcap and the ring electrodes (for the finite size of the trap) and at the entrance and exit holes of the endcaps. To determine the required voltages for the correction electrodes, calculations were performed with the optimized relaxation method which was found to give necessary accuracy, followed by a least-square fit to a pure quadrupolar field, *i.e.*, taking into account the sum of all higher multipoles. The octopole coefficient for the trap is found to be $|C_4| \approx 10^{-5}$ [Bol1996]. The calculations give directly the best theoretical values for the correction electrode voltages. For a trapping voltage of $U_0 = 8.4$ V, the experimentally determined voltages are tabulated in Table 3.4. The values are in reasonable agreement with the calculated ones within the numerical accuracy of the calculation and the mechanical tolerance of the trap.

The ring electrode is split into four 90° – segments in order to apply the azimuthal quadrupolar RF field needed for the excitation of the ion motion. In order to preserve the good quality of the electric trapping field the slits are only 0.2 mm wide.

Magnetic field inhomogeneities from the trap itself are kept small by the use of materials with low susceptibility. The trap material is oxygen free (OFHC) copper which is additionally gold plated. Glass ceramics (MACOR) are used for insulation. The room temperature susceptibilities of the used materials are listed in Table 3.5. In addition all parts are machined as thin as possible in order to minimize magnetic

Table 3.4: The dimensions, static and dynamic parameters for the Precision Penning Trap of ISOLTRAP under normal trapping/ejection condition. The trapping voltage for this set of parameters is $U_0 = 8.4$ V.

Element	Trapping voltage /V	Ejection Voltage /V
Coverplate	-22.0	-22.0
Lower correction tube	+1.10	+1.18
Lower endcap	-1.60	-1.60
Lower correction electrode	-6.6	-6.6
Ring electrode	-10.0	-2.5
Upper correction electrode	-6.6	-6.6
Upper endcap	-1.6	-2.6
Upper correction tube	+1.10	-2.6
Characteristic trap dimension		
ρ_0		13.00 mm
z_0		11.18 mm
d		10.23 mm
Magnetic field		
Field strength at the trap center		5.9 T
Relative homogeneity		$< 10^{-7}/\text{cm}^3$
Relative stability		$< 10^{-8}/\text{h}$
Vacuum /mbar		$< 10^{-8}$
Typical eigenfrequencies for an ion with mass number A=100		
ν_+		910 kHz
ν_-		1.08 kHz
ν_z		44 kHz

field distortion. It is possible to calculate the effects for different shapes and sizes of these material by a computer program called SUSZI [Sch2004a] and hence to optimize the homogeneity.

The time-of-flight drift section

The time-of-flight ion cyclotron resonance detection technique, as discussed in Section 3.1.4, allows to measure the difference in the time of flight from the trap to

Table 3.5: The magnetic susceptibilities of the used trap materials as compared to that of stainless steel.

Material	Magnetic susceptibilities /cgs unit
OFHC	-7.7×10^{-7}
MACOR	-3.8×10^{-7}
Stainless steel (316LN)	7.2×10^{-4}

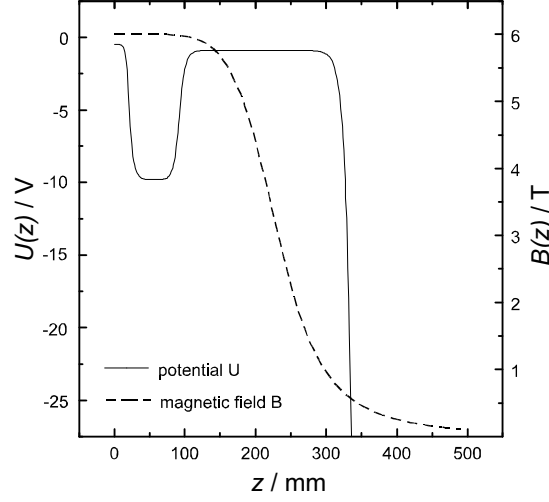


Figure 3.23: The electric potential and the magnetic field strength along the geometrical axis in the first part of the drift section of the mass spectrometer. Maximum retardation is applied in the region of the strongest magnetic field gradient in order to achieve a maximal energy conversion.

the detector as a function of the excitation frequency. For this a proper drift section is designed which enables to fully convert the initial radial energy to axial energy. In addition it serves to efficiently transport the ions to the detector situated 1.3 m above the trap outside the strong magnetic field. Figure 3.23 shows the magnetic and electric potentials in this section. The voltages applied to the drift tubes of this section are listed in Table 3.6. Ions ejected from the Precision Trap drift with a few eV kinetic energy in the homogeneous part of the magnetic field at DS1 (Figure 3.21). They are maximally retarded at the onset of the strongest gradient of the magnetic field but then they slowly drift through the highest field gradient (DS2,DS3) in order to convert 10 eV radial energy fully into axial energy. Since the initial magnetic moment of an ion (see Section 3.1.4)

$$\mu = E_{r,\text{init}}(\omega_q)/B_{\text{init}}, \quad (3.54)$$

Table 3.6: The dimensions and applied voltages for the ion optics in the time-of-flight drift section [Kön1995a].

Element	Length /mm	Voltage /V
DS1	65	-11.1
DS2	200	-2.45
DS3	110	-2.45
DS4	100	-350
DS5	200	-1200
DS6	200	-1100
DS7	280	-1100
DS8	120	-660

is conserved along the ion flight path, one obtains:

$$E_{r,\text{init}}(\omega_q)/B_{\text{init}} = E_{r,\text{final}}(\omega_q)/B_{\text{final}}. \quad (3.55)$$

With the ISOLTRAP magnetic field strength at the trap center and at the detector position the factor by which the radial energy decreases, *i.e.* the axial energy increases and it is given by

$$E_{r,\text{init}}/E_{r,\text{final}} = B_{\text{init}}/B_{\text{final}} \approx 3000. \quad (3.56)$$

In the second part of the TOF section the ions are accelerated (DS4,DS5,DS6) and focussed (DS7) to a micro-channel-plate detector with 18 mm active area diameter.

3.2.6 Off-line ion sources

ISOLTRAP uses two different types of ion sources for its off-line mass and test measurements as well as for magnetic field calibration needed to perform on-line mass measurements on radioactive ions. One of them is a surface ion source mainly delivering ions of alkali elements like K, Rb, and Cs. Presently this ion source is in use to provide well-known reference masses. The second ion source is a laser desorption carbon cluster ion source used for investigating the relative mass uncertainty limit of ISOLTRAP [Kel2003].

Surface ion source

An atom gives away its valence electron to a hot metal surface made of a material with higher work function, and hence forms an ion. Based on this principle, almost all alkali elements can be ionized by a rhenium or tungsten ionizer heated directly or indirectly. ISOLTRAP presently uses an indirectly heated tungsten ionizer.

A directly heated graphite furnace is planned to be installed end of this year to replace the present ion source. Figure 3.24 shows the design of the new ion source. In addition to the surface ionizer it includes a cross beam ionizer where atoms of noble gases or those atoms released by the furnace can be ionized by electron bombardment from a filament. A radiofrequency quadrupole mass filter is placed behind the ionizers for mass separation. The ions are finally extracted via a conical extraction electrode. This ion source assembly is placed before the RFQ cooler and buncher and perpendicular to the ISOLDE beam line (see Figure 3.14). Ions thus created are injected into the RFQ by applying proper voltages to a kicker and bender electrode. In order to create the ions at an energy similar to that of the ISOLDE beam, the ion source is placed at a high-voltage platform of 60 kV. Similar ion optical conditions for both, the off-line ion source and the ISOLDE beam, helps in fast switching between stable reference and radioactive ion beams. This in turn minimizes the systematic uncertainty due to the temporal fluctuations of the magnetic field.

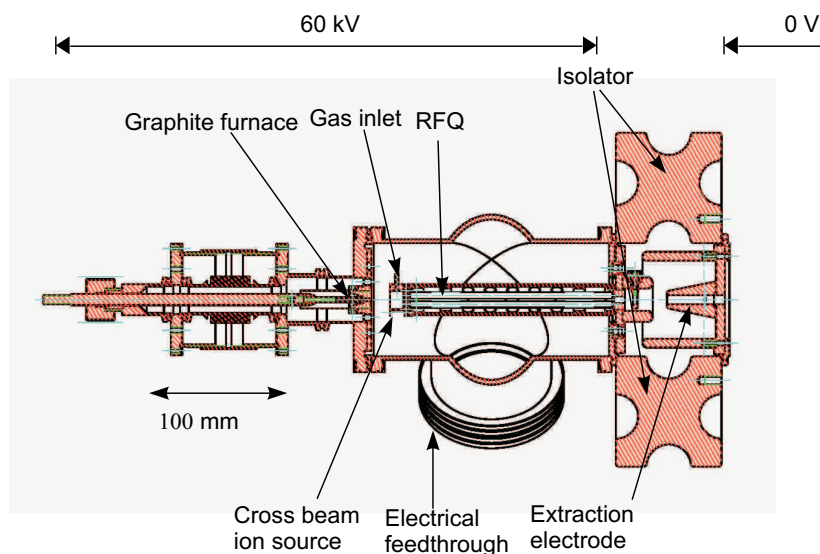


Figure 3.24: Design of the new combined surface and cross beam ion source together with a quadrupole mass filter.

Previously used carbon cluster ions source

Clusters consisting of a few atoms build the bridge between individual atoms and the condensed phase of matter and they are thus of high general interest. Over the last two decades considerable progress has been made in the study of their properties. Ion storage techniques, in particular the use of Penning traps, are tools for advanced investigations of cluster properties. Vice versa, cluster ions can serve as probes for the evaluation of ion trap properties. Furthermore, they are ideally suited for the calibration of mass spectrometers and for consistency checks and systematic uncertainty studies in high-accuracy mass determination [Bla2002] (see also Section 3.1.3). In this context, carbon clusters provide the reference mass of choice. The advantages are obvious: A multitude of reference masses all over the nuclear chart are available which are at most six atomic mass units away from any nuclide of interest. Thus, any systematic mass-dependent uncertainty which increases with the difference between the measured and the reference mass is minimized. By use of carbon clusters as mass references not only direct mass measurements but also absolute mass measurements can be performed since the building blocks of carbon clusters $^{12}\text{C}_n$ are related as closely as possible to the microscopic mass standard: The unified atomic mass unit is by definition $1/12^{\text{th}}$ of the mass of ^{12}C .

ISOLTRAP used a laser ion source for the desorption, fragmentation, and ionization of the C_{60} Fullerene [Sch2002, Kel2003]. Due to its low extraction rate and intensity instabilities it was not possible to use it as a reference ion source especially during on-line mass measurements. For the systematic studies with cross reference measurements, the carbon cluster source was mounted two meters below the Purification Penning Trap, as shown in Figure 3.14, and the 90° electrostatic bender between quadrupoles QP1 and QP3 was removed. Within this work a new carbon cluster laser ion source has been developed to allow the possibility to go for absolute mass

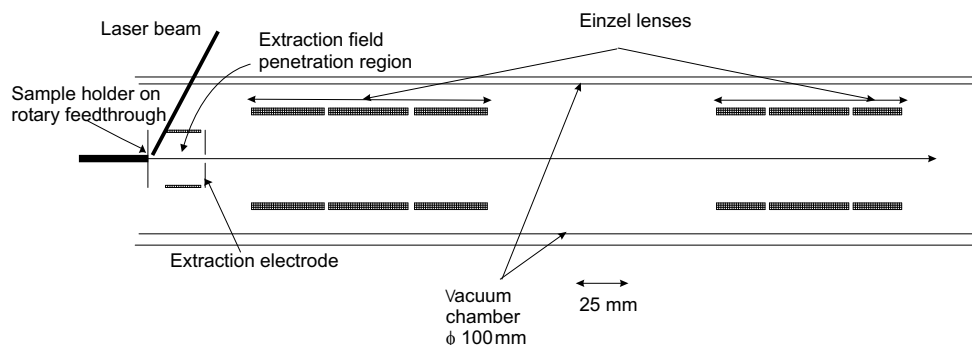


Figure 3.25: To-the-scale drawing of the present carbon cluster laser ion source. The design is based on detailed simulation studies.

measurements during on-line runs. This new source is now mounted at a position just before the quadrupole QP1 which allows a fast switching between radioactive ions and carbon cluster ions since the 90° bender stays in place. The ions are created at a potential of 2.5 kV, so their kinetic energy corresponds to the one of the ions coming from the RFQ buncher.

Present carbon cluster ion source

In order to improve the transport efficiency of the carbon clusters from the creation point to the Purification Penning Trap, a careful ion optical simulation has been performed prior to the designing of the new source.

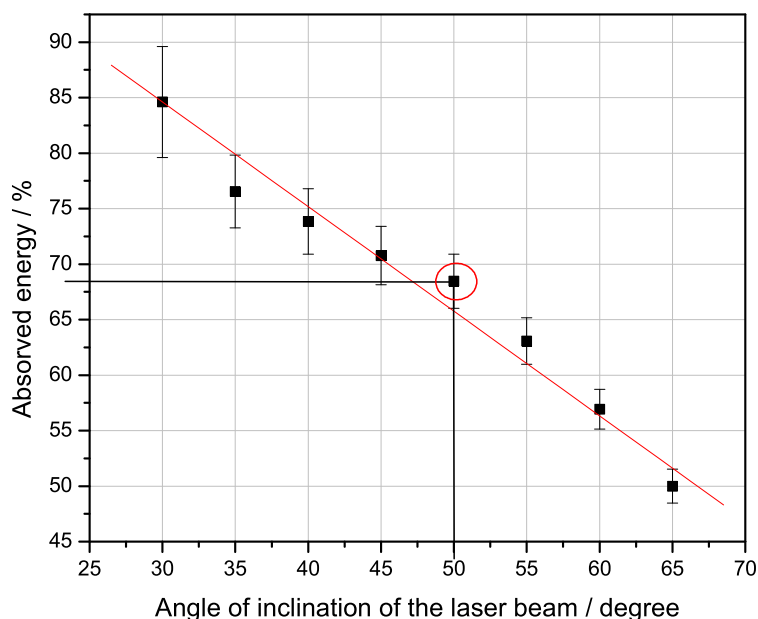


Figure 3.26: The percentage of the absorbed laser power as function of the incidence angle on a Sigradur® sample.

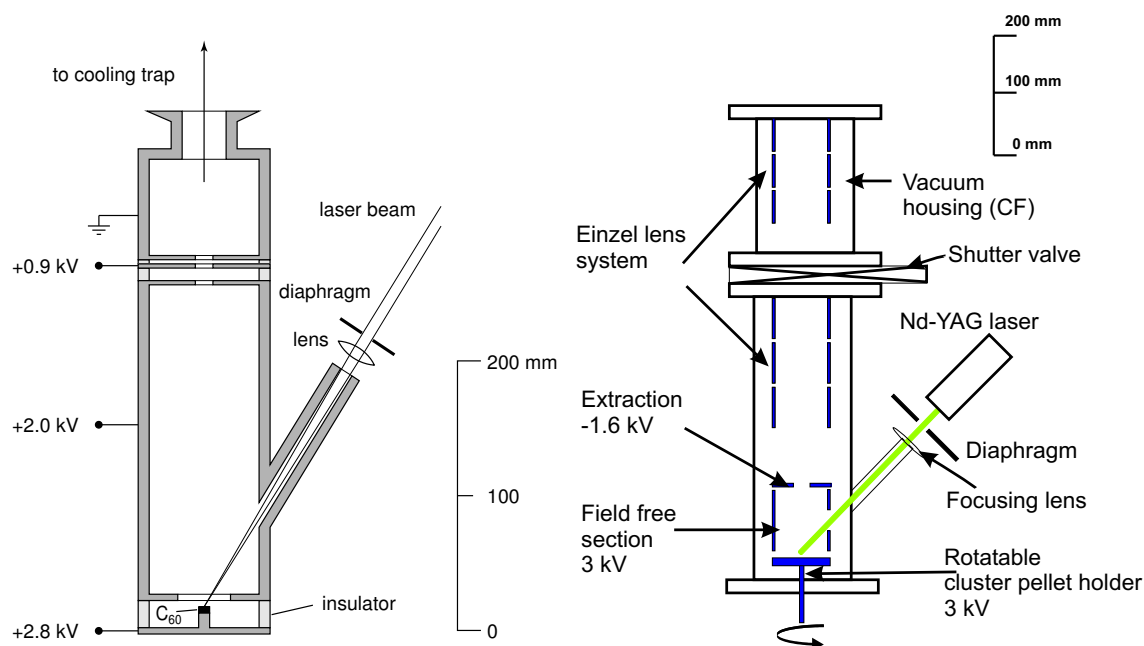


Figure 3.27: Overview sketch of the previous (left) [Bla2002] and present (right) carbon cluster ion source.

The final simulated design of the source is shown in Figure 3.25. It consists of a sample holder, an extraction electrode with a small aperture, and two sets of einzel lenses to focus the beam at the center of a 4-rod quadrupole deflector situated at the place of MCP2(h) (see Figure 3.14). This will ensure efficient capture of the ions in the Purification Penning Trap of ISOLTRAP. For the simulation studies the ions were generated randomly over a circular area of 8 mm diameter having random angular distribution between 0° - 180° . The energy distribution of the created ions was chosen to be 0 – 10 eV. These are about the initial conditions of the carbon cluster ions produced by laser desorption/ionization. The spatial distribution of the ions is due to the temporal variation of the laser spot position.

This new source design fulfills in addition the following conditions:

- Fast exchange of the sample is possible.
- Rotatable sample holder to change continuously the sample surface at the laser spot position.
- Possibility of using different samples, *i.e.* different elements, at the same time.
- Possibility for beam alignment correction, in case of any misalignment at the ion formation/extraction region.
- The angle of inclination of the laser beam with respect to the sample is 52° . The relative intensity absorbed at this angle by a Sigradur[®] carbon sample was measured to be $\sim 68\%$ as shown in Figure 3.26.

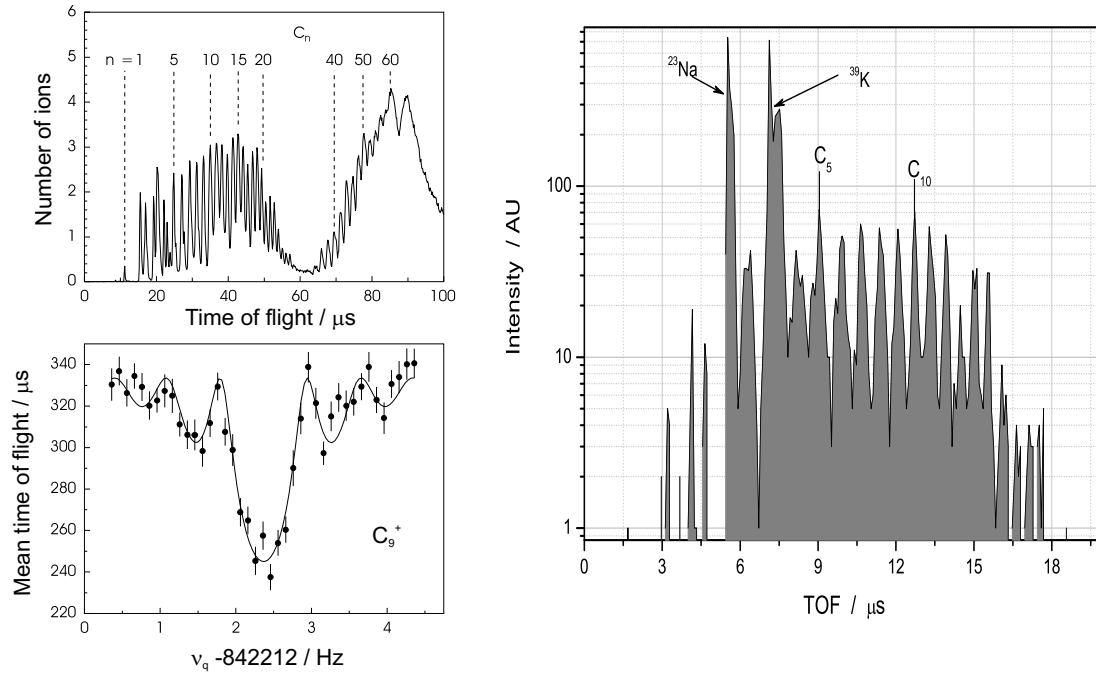


Figure 3.28: Typical time-of-flight signal and a TOF cyclotron resonance plot for C_9^+ measured with Fullerene fragments produced from the previous carbon cluster ions source (left) and a similar spectrum obtained by fragmentation of a Sigradur[®] sample using the present cluster ions source (right) with a laser power of 15 mW. The two peaks of relatively high intensity are because of ^{23}Na and ^{39}K contamination.

The new design of the carbon cluster ion source is shown in Figure 3.27. In the case of a required quick exchange of the sample one can close the shutter valve and vent only the lower part without affecting the rest of the vacuum system. The sample holder is situated on a rotatable feedthrough and the laser spot is focussed off center thereby avoiding to hit the same spot all the time. This ensures longevity of the sample. This kind of arrangement also ensures the possibility of having different samples at the same time on the sample holder. The laser repetition rate as well as the intensity can be adjusted with respect to the sample of interest, the ion bunch intensity, and the measurement cycle. The source has now been tested off-line and a typically obtained TOF spectrum of cluster fragments from a Sigradur[®] sample is shown in Figure 3.28. The ions have been detected by a channeltron detector placed at the focus of the second lens system. The Nd-YAG laser was frequency doubled ($\lambda = 532 \text{ nm}$) and its power was $P_{\text{av.}} = 15 \text{ mW}$. The energy distribution of the produced ions was measured to be about 20 eV at a beam energy of 3 keV, which matches well with the simulated value. This low energy spread is also essential for an efficient loading into the Purification Penning Trap.

3.2.7 The beam diagnostic system

ISOLTRAP uses micro-channel-plate (MCP) detectors to monitor the ion bunch transfer and to record the time-of-flight (TOF) cyclotron resonance (MCP5, see Fig-

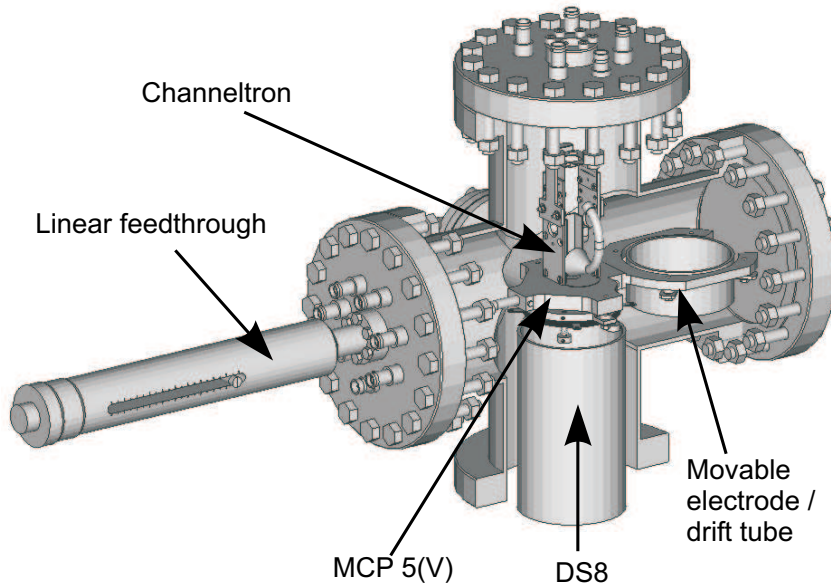


Figure 3.29: The new detector setup having possibility to use a micro channel plate (MCP) and a highly efficient channeltron detector [Yaz2004]. DS8 is the last electrostatic ion optical element before the detector as shown in Figure 3.21.

ure 3.14). To monitor the ISOLDE beam current and its profile, there is one movable faraday cup detector and a scanner placed in front of the RFQ entrance. Both of them are part of the ISOLDE diagnostic tools. This ensures proper injection of the 60-keV ISOLDE beam into the RFQ structure. On the ejection side of the RFQ there is another movable faraday cup and in addition a MCP detector (MCP1(h)). This allows to optimize the ISOLDE beam transfer and RFQ injection by shooting through the RFQ structure. Ion current on the faraday cup is measured by a picoammeter (Keithley 485). All along the beam line there are 7 MCP detectors. Four of them are shown in Figure 3.14. They are all composed of two MCP's with either 50 mm (MCP5/6(V)) or 25 mm active area mounted in a Chevron arrangement. No electron repelling grids are in use. MCP1(v) is mounted in addition with a beam viewing system (Colutron BVS-2) in order to determine the spatial distribution of the ions after the 90° bender. It consists of a MCP and a phosphor screen behind it. The fluorescence signal created by the ion impact on the MCP is monitored by a CCD camera through a glass window. The typical efficiency of such a MCP set is about 30%.

In order to increase the detection efficiency and thus to minimize the required beam-time and to explore more exotic, *i.e.* shorter-lived nuclides, ISOLTRAP is planning to replace its final TOF detector (MCP5(v)) by a specially designed channeltron detector [Yaz2004]. This off-axis channeltron detector with conversion dynode will provide close to 100% detection efficiency. A drawing of the new detection setup is shown in Figure 3.29. The new setup will allow to use the existing MCP5(V) detector and, in addition, makes it feasible to use the highly-efficient channeltron detector.

3.2.8 Control system

ISOLTRAP uses a state-of-the-art control system for running the experiment. More than 100 parameters need to be controlled. The basic requirement of such a control system is to run the measurement cycle (see Section 3.3.1) with a time accuracy in the order of 100 ns. More importantly the system has to be synchronized to follow the time sequences, as elaborated in Section 3.3.1, repeatedly and reliably over weeks of beamtime. Since spring 2003, ISOLTRAP is using a new control system based on the Control System (CS) framework [Bec2002], which has been developed by DVEE/GSI. CS is an object-oriented, multi-threaded, event-driven framework with Supervisory Control and Data Acquisition (SCADA) functionality. It allows one to implement distributed control systems by adding experiment specific add-ons. An elaborate documentation of the control system can be found in [Bec2004]. Here, only a brief description will be given.

Figure 3.30 shows a simplified layout of the ISOLTRAP control system. The hierarchy is composed of the hardware devices, a control PC, and a Graphical User Interface (GUI) PC. The main difference to the earlier control system is that of the control PC. In the past it was a VME bus with a Motorola E6 CPU and the control system software was developed in GNU C [Emm1993] language. The present control system uses only one rack mounted PC for simplicity. All devices can be accessed by GPIB (General Purpose Interface Bus) or via a Object Linking and Embedding for

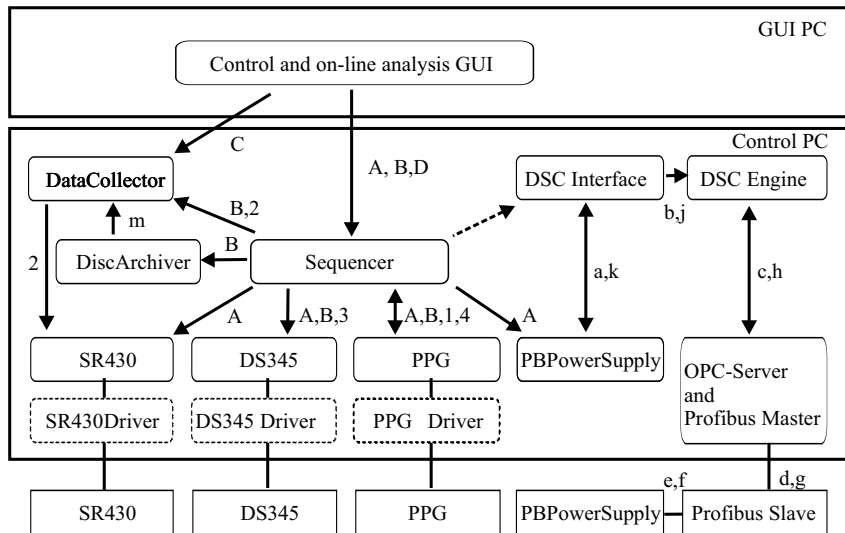


Figure 3.30: Simplified layout of the ISOLTRAP control system. Rectangular boxes represent hardware while round cornered boxes represent software. Active (inactive) software objects have solid (dashed) bordered boxes. Arrows indicate event-driven communication. The direction of the arrows do not indicate the direction of the data flow, but mark caller and callee. To simplify the figure, trending and alarming is indicated only for the Sequencer but not for the other active objects on the Control PC (dashed arrow). Direct method calls and hardware connections are marked by lines. Uppercase and lowercase letters as well as numbers denote communication paths. For detailed explanation see [Bec2004].

Process Control (OPC). The connection to the RFQ cooler and buncher situated at the high voltage platform is provided by optical GPIB and profibus links. The control and online analysis GUIs are written in Borland C++ while the rest is based on the CS framework which is in LabVIEW from National Instruments (NI). An event driven object oriented programming approach is adapted for the CS. Typically 70 objects are created for operating the experiment. For example eight objects are shown in Figure 3.30: *SR430* is a multi-channel-scaler for data acquisition, *DS345* is a function generator for the RF-excitation of the ion motion, *PPG* is a pulse pattern generator to produce bit pattern with 100 ns precision, other devices like *PBPowerSupply*, a power supply controlled by analog I/O of the profibus are described in [Bec2004]. The *Sequencer* is the heart of the control system maintaining the proper sequence of the experimental processes, the *DataCollector* serves to collect and buffer data from the acquisition devices, the *DiscArchiver* retrieves the buffered data from the *DataCollector* and writes it to a permanent storage device. The *DSCInterface* is the interface between all objects and the *DSCEngine* from NI. It serves for trending and alarming as well as a client that is connected to an OPC server and Profibus Master via Object Linking and Embedding (OLE) for Process Control (OPC). Like the DSCEngine, the OPC server and the Profibus master is a commercial product (Beckhoff).

3.3 Experimental mass measurement procedure at ISOLTRAP

At present different experimental mass measurement procedures and time sequences are adopted depending on the nuclide of interest, the presence of impurities, and the half-life of the radionuclide. Here, the most commonly used procedure will be discussed which is carried out within 200 ms to 1.5 s depending on the half-life of the nuclide of interest. A complete process includes accumulation, cooling, and bunching of the ISOLDE DC beam by the RFQ cooler and buncher, the purification and preparation of the ion ensemble in the Purification Penning Trap, and finally the TOF ion cyclotron resonance measurement in the Precision Trap. This is one measurement cycle for a fixed frequency of the quadrupolar RF excitation applied to the ions in the Precision Penning Trap. This cycle is repeated for different frequencies around the (expected) cyclotron frequency to obtain a TOF ion cyclotron resonance curve. The overall cycle consisting of a certain number of frequency steps is repeated several times until enough statistics is obtained. This we call an ion cyclotron resonance (ICR) cycle. To perform a mass measurement, one ICR cycle for the ions of interest from ISOLDE is carried out in between two ICR cycles for the reference ion.

3.3.1 Time sequence for single measurement cycle

Figure 3.31 shows the time pattern that is used within one complete measurement cycle for the cyclotron frequency determination of a radionuclide with half-life in

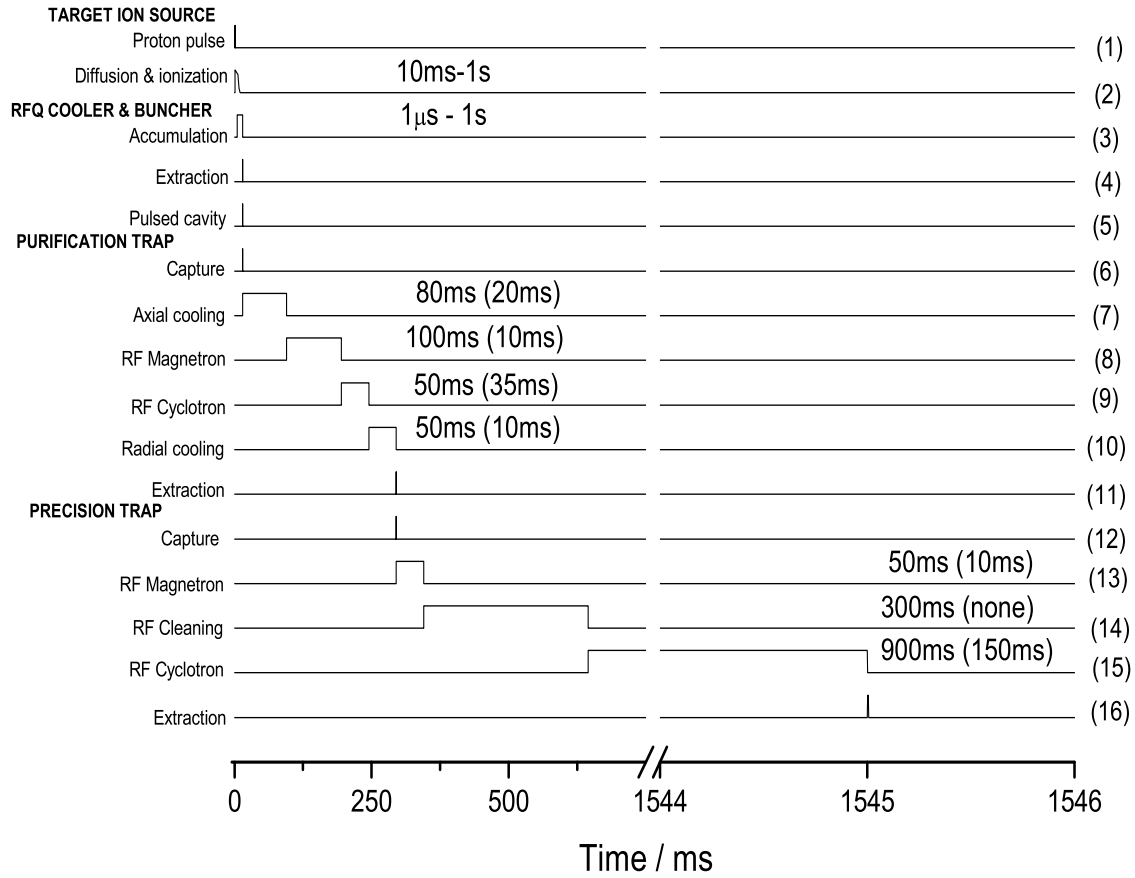


Figure 3.31: Timing diagram of the measurement cycle for a rather long lived ($T_{1/2} = 1$ s) and a very short-lived (within parenthesis) ($T_{1/2} = 100$ ms) radionuclide. A detail discussion is given in the text.

the order of few seconds, like ^{22}Mg ($T_{1/2} = 3.8$ s). It also depicts within parenthesis the corresponding values for a mass measurement on a very short-lived radionuclide with a half-life of about 100 ms. The cycle is started by the proton impact (1) on the ISOLDE target. The diffusion and ionization of the radionuclides last between 10 ms and up to several seconds (2). The processes in the RFQ buncher start with a certain delay (determined by the release time (2)), continues with the accumulation time (3) of about 5-10 ms followed by ejection (4). After a few μs flight time, depending on the mass of the radionuclide, the first pulsed cavity is switched down (5). The capture in the Purification Trap (6) initiates the process to be continued there. It is subsequently followed by an axial cooling of 80 ms (7), magnetron excitation for 100 ms (8), cyclotron excitation of 50 ms (9), radial cooling by waiting for 50 ms (10) before being ejected from the trap (11). A similar time pattern holds for the Precision Trap where capturing (12) triggers the dipolar magnetron excitation for 50 ms (13) followed by dipolar cleaning excitation (if needed) for about 300 ms (14) and finally the RF cyclotron excitation for 900 ms (15) before being ejected for the TOF measurement.

The experimentally obtained line width of a TOF resonance is given by [Bol1996]

$$\Delta\nu_c \approx \frac{0.9}{T_q}, \quad (3.57)$$

where T_q denotes the duration of the quadrupolar RF excitation in the Precision Trap. Mainly, three parameters determine the total duration of a measurement cycle. 1. The required resolving power of the Purification Trap, 2. the envisaged resolving power and accuracy in the Precision Trap, and 3. the half-life of the ions of interest. A lower buffer gas pressure in the Purification Trap results in a higher resolving power but it also increases the cooling and centering time needed. The narrower the line width of the TOF resonance, the more precise the center frequency can be determined. Of course the half-life gives a natural limit. ISOLTRAP uses short cycles for very short-lived radionuclides, *e.g.* for ^{32}Ar , with a half-life of only 98 ms, a total measurement cycle time of about 200 – 300 ms [Bla2003a] was used in order to minimize decay losses. The exotic nuclide ^{74}Rb , with a half-life of only 65 ms, is the shortest-lived nuclide on which a high-precision mass measurement in a Penning trap has been performed. An even shorter measurement cycle of only 150 ms was in use for that.

3.3.2 Cleaning processes

The highest possible mass resolving power of ISOLDE's high-resolution separator is at present about $m/\delta m = 5000$. This can only be achieved by the use of slits after the separator magnet which also results in the reduction of the beam intensity. In many cases this resolving power is not sufficient to obtain a pure mono-isobaric beam. In addition, the resolving power is not sufficient to resolve isomers. Isobaric contaminants are the main impurities that finally needs to be separated by the Purification Penning Trap. Here the resolving power is limited to 10^5 for masses around $A = 100$ and a cooling time of several hundred ms. $R = 30\,000$ is routinely achievable. This is sufficient to separate and to remove by dipolar cleaning almost all isobaric contaminants provided the ratio of the contaminants to the ions of interest is not too high (in the order of 300 : 1). For cleaning ISOLTRAP uses dipolar excitation at the reduced cyclotron frequency ω_+ , thereby driving out only the unwanted species. The resolving power of this cleaning becomes higher if the frequency is set to $2\nu_+$ instead of ν_+ . This is already tested but at present not implemented at ISOLTRAP. In case of a too high number of contaminant ions (≥ 1000), space charge effects have been observed.

3.3.3 Magnetron phase lock mechanism

ISOLTRAP implemented recently a new timing scheme including a magnetron-phase-locking mechanism [Bla2003b], which increased the sensitivity significantly by increasing the TOF effect and eases the access to nuclides that are produced in minute quantities. One example of such a measurement is ^{32}Ar [Bla2003a] ($T_{1/2} = 98$ ms) that is produced with only 100 ions/s at ISOLDE.

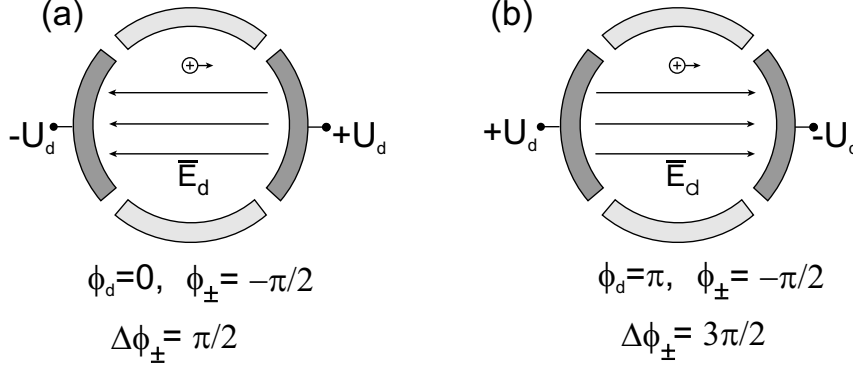


Figure 3.32: (a) Electric dipolar-excitation field \vec{E}_d for $\phi_d = 0$. \vec{E}_d points in the negative x -direction. A positive ion at $\phi_{\pm} = -\pi/2$ is also shown with the arrow indicating its direction of rotation. The phase difference is $\Delta\phi_{\pm} = \pi/2$. (b) For $\phi_d = \pi$, \vec{E}_d points in the positive x -direction. The phase difference is $\Delta\phi_{\pm} = 3\pi/2$ [Bla2003b]. The ion of interest was ^{39}K from the reference ion source.

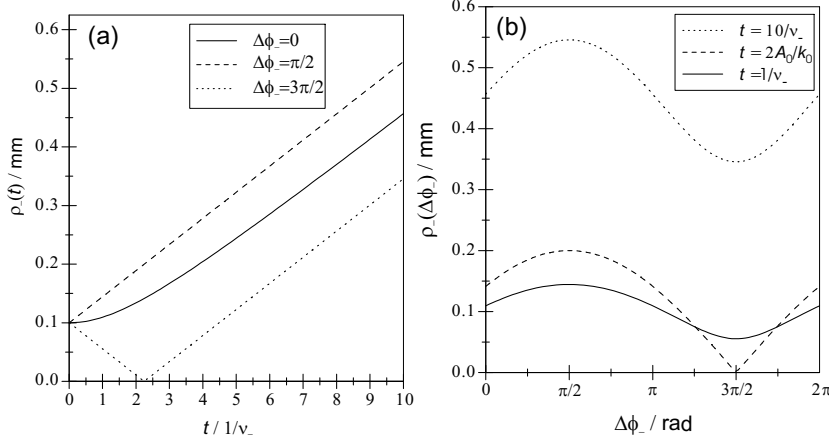


Figure 3.33: (a) Dipolar excitation of the magnetron motion in ISOLTRAP's Precision Trap. The magnetron radius is plotted versus the excitation time (given in units of the magnetron period) for three phase differences $\Delta\phi_- = 0, \pi/2$, and $3\pi/2$. For $\Delta\phi_- = 0$ (solid curve) it grows slowly at first, then almost linearly, for $\Delta\phi_- = \pi/2$ (dashed line) it grows linearly from the very beginning of the excitation and for $\Delta\phi_- = 3\pi/2$ (dotted line) it first shrinks to zero before it grows linearly with t . (b) Magnetron radius plotted versus $\Delta\phi_-$ for three different excitation times t : $t = 1/\nu_-$ (solid), $t = 2A_0/k_0$ (dashed) where the amplitude becomes zero for $\Delta\phi_- = 3\pi/2$, and $t = 10/\nu_-$ (dotted). The sine-like shape from the phase-dependent term in Eq. (3.58) is obvious [Bla2003b].

In Eq. (3.33), one can replace $\phi_d - \phi_{\pm}$ by $\Delta\phi_{\pm}$ and $(\omega_+ - \omega_-)\rho_{\pm}(0)$ by $A_{\pm}(0)$ to obtain

$$\rho_{\pm}(t) = \frac{1}{(\omega_+ - \omega_-)} \sqrt{A_{\pm}^2(0) + \frac{1}{4}k_0^2 t^2 \mp A_{\pm}(0)k_0 t \sin \Delta\phi_{\pm}}. \quad (3.58)$$

Equation (3.58) shows that if the resonantly excited initial ion radius is greater than zero, the phase difference between the ion eigen motion and the dipolar excitation

signal plays an important role on the evolution of the ion radius due to the excitation. The time evolution of the reduced-cyclotron and the magnetron radii are affected oppositely due to the presence of the $\pm \sin(\Delta \phi_{\pm})$ term in Eq. (3.58). Three scenarios of the phase differences are illustrated here:

- $\Delta \phi_{\pm} = 0$: In this case the sine term in Eq. (3.58) vanishes and the radius grows slowly at the beginning, then almost linearly with the excitation time (see Figure 3.33(a)).
- $\Delta \phi_{\pm} = \pi/2$: This situation is illustrated in Figure 3.32(a), where the dipolar excitation field E_d is antiparallel to the ion's motion. Here, $\sin(\Delta \phi) = 1$ and the root in Eq. (3.58) becomes $|A_{\pm}(0) \mp \frac{k_0}{2}t|$. In the case of resonant reduced-cyclotron excitation, $\rho_+(t)$ is diminished linearly with t to zero. Then it grows linearly with t . In the case of resonant magnetron excitation, $\rho_-(t)$ grows linearly with t from the very beginning of the excitation.
- $\Delta \phi_{\pm} = 3\pi/2$: This situation is illustrated in Figure 3.32(b), where the dipolar excitation field E_d is parallel to the ions motion. For this phase difference $\sin(\Delta \phi) = -1$ and the root term becomes $|A_{\pm}(0) \pm \frac{k_0}{2}t|$. In the case of resonant reduced-cyclotron excitation, $\rho_+(t)$ grows linearly with t from the very beginning of the excitation. In the case of resonant magnetron excitation, $\rho_-(t)$ diminishes linearly with t to zero and then it grows linearly with t .

Since the evolution of the magnetron excitation is of present interest, only this kind of excitation is considered now. The graph in Figure 3.33(a) shows plots for the realistic case of a dipolar excitation of the magnetron motion in the Precision Trap of ISOLTRAP for three different phase differences discussed above.

In the plot of Figure 3.33(b), the magnetron radius $\rho_-(t)$ is plotted as a function of the phase difference $\Delta \phi_-$ for three different excitation times: $t = 1/\nu_-$ (one magnetron period), $t = 2A_0/k_0$ (a bit more than two periods) where the amplitude becomes zero for $\Delta \phi_- = \pi/2$ and $t = 10/\nu_-$ (ten periods). Here $A_0 = A_-(0)$. The last case is the one valid for ISOLTRAP's measurement cycle. The sine-like shape of the curves results from the phase-dependent term in Eq. (3.58).

The temporal spread of the ion bunch from the Purification Trap to the measurement trap is about $1 \mu\text{s}$ while the typical magnetron frequency for ^{39}K is around one kHz. So the ion bunch can be considered as belonging to the same magnetron phase.

Figure 3.34 demonstrates the variation of the TOF effect for different phases of the applied magnetron RF excitation field. All resonances were taken with similar number of ions ($N = 5000$). Experimentally the proper phase is determined by looking at the variation of the TOF at the resonance minimum while varying the delay of the externally applied dipolar magnetron excitation and hence the phase of it with respect to the phase of the ions initial magnetron motion. By choosing the optimal phase for the magnetron excitation the uncertainty of a measured cyclotron frequency is reduced significantly compared to a measurement with an average phase difference (while keeping the number of ions constant). It also reduces the required radioactive beam time to reach a certain statistical uncertainty.

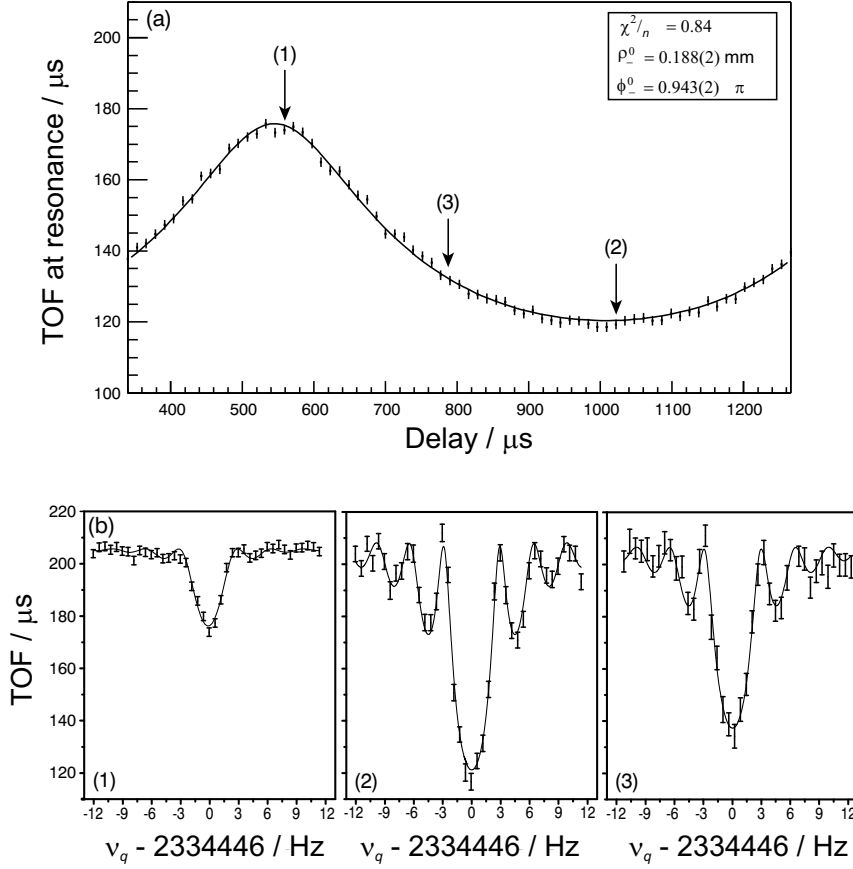


Figure 3.34: (a) The Time-Of-Flight (TOF) at the TOF resonance minimum when Scanning the magnetron excitation phase [Bla2003b]. The delay was scanned from 340 to 1266 μs corresponding to a phase scan of $0 - 2\pi$. The solid curve represents a fit of the theoretical curve to the data. (b) Cyclotron resonance scans recorded at the three marked points. (1) $\Delta\phi_- \approx 3\pi/2$, where the response to the magnetron excitation is minimal. (2) $\Delta\phi_- \approx \pi/2$, where the response to the magnetron excitation is maximal. (3) $\Delta\phi_- \approx 0$, where the response to the magnetron excitation is similar to the response with an averaged phase. In all three plots the solid curve is a fit of the theoretical function [Kön1995b] to the data.

3.3.4 Tuning of the trap parameters

Section 3.1.3 summarized the importance of minimizing the magnetic and electric trapping field imperfections with the goal to achieve highest accuracy in direct mass determination. ISOLTRAP adapted some of the already known procedures [Bol1996, Bec1997] and developed it further [Gué2004] to tune its Precision Trap and to determine the limit of the systematic uncertainty that are generated by the residual imperfections.

Capture timing to the Precision Trap

The cooled ion bunch from the Purification Trap is captured in the Precision Trap after a certain delay time called the “capture time” which corresponds to the flight

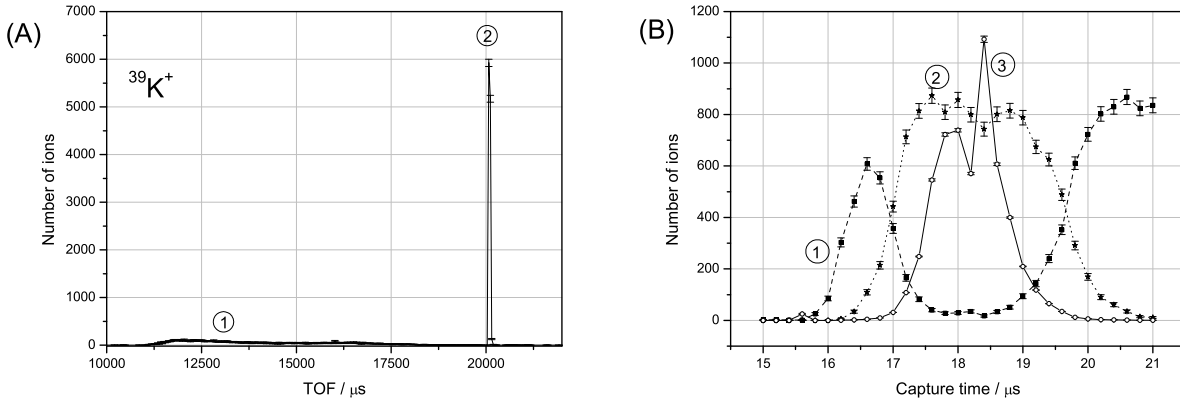


Figure 3.35: (A) Number of $^{39}\text{K}^+$ ions as a function of their time of flight from the Precision Trap to the detector. Ions which have large axial energy and a wide energy distribution due to a wrong capture time appear with a much shorter time of flight in spectrum (1). Correctly captured ions (2) appear at a later time due to lower axial energy. In addition their energy spread is much smaller. (B) Number of $^{39}\text{K}^+$ ions as a function of the capture time in the Precision Trap. The ratio of the “slow” (1) and the “fast” (2) ones is magnified by a factor of 25 (3).

time between the two traps. A variation of this delay time leads to a capture at a certain position in the Precision Trap and also to a variation of the number of trapped ions. Being unable to reach the potential minimum of the Precision Trap for a very short capture time, the cooled ion cloud gains axial energy due to the switching of the endcap electrodes. They are called the “fast” ions. The same happens for a too long capture time as it matches with one axial oscillation period of the ion cloud in the trap. Only if the capture time is set to a proper value the cooled ion cloud stays in the Precision Trap without gaining any axial energy. They are called the “slow” ions. These two types of $^{39}\text{K}^+$ ions, can be distinguished by their TOF distribution after being released from the Precision Trap as shown in Figure 3.35(A). The first curve (#1) with a broad time distribution shows the “fast” ions that get captured at a relatively short delay capture time as well for very long capture time. The second narrow curve (#2) obtained from the “slow” ions has its maximum at a delay time around $18.5 \mu\text{s}$. The second class of ions are the ones with low axial energy which have to be used to avoid systematic errors due to electric field imperfections in the Precision Trap. Thereby a plot as shown in Figure 3.35(B) of the ratio (magnified by a factor of 25) of these two count rate classes as a function of the capture time provides the best possible value for the capture time.

Magnetic-field optimization

Once the capture time is known, it is essential to minimize the magnetic-field inhomogeneity as discussed in section 3.1.3. The capture time is the tool to probe the extent of the homogeneous trap volume while the shift in the cyclotron frequency

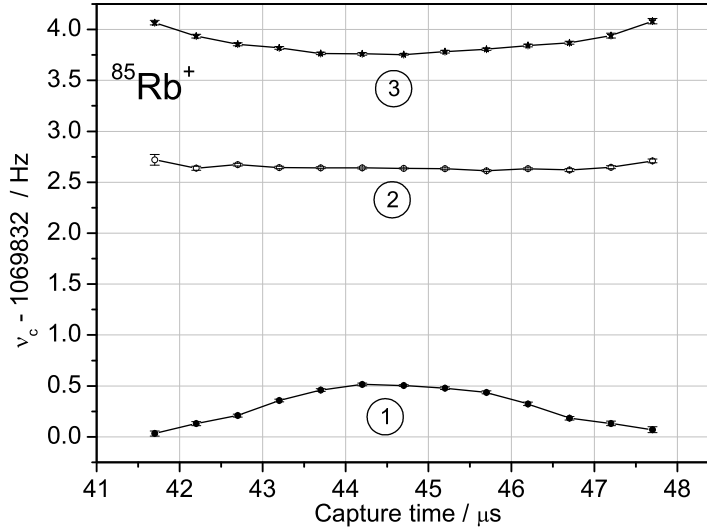


Figure 3.36: Cyclotron frequency variation as a function of the capture time in the Precision Trap for different values of the shim coil current: 100 mA (1), 270 mA (2) and 350 mA (3).

is the measurement parameter to determine the magnetic field homogeneity. Figure 3.36 shows the cyclotron frequency as a function of the capture time for different current values of the correction shim coils of the superconducting magnet. A current of 270 mA turns out to be the best value for which the cyclotron frequency varies only very little. These measurements were performed with $^{85}\text{Rb}^+$ ions from the reference surface ion source of ISOLTRAP. However, the optimized values are mass independent and can be kept for experiments with different masses.

Electric-field optimization

In a very similar way as the magnetic-field optimization, the electric-field imperfections can be minimized as well. The electric-field optimization aims to make the electric field harmonic over the largest possible volume in the trap. Imperfections can be minimized by optimizing the voltages applied to the correction electrodes (correction ring as well as the correction tubes, see Figure 3.22) of the Precision Trap. A plot of the ν_+ frequency, which is sensitive to the electric field imperfections, for $^{85}\text{Rb}^+$ as a function of the capture time for different correction electrode voltages is shown in Figure 3.37. Clearly the correction tube voltage of 1.120 V is the optimal one, since the ν_+ stays almost constant over a large variation of the capture time, hence over a larger trap volume. This optimization is performed after the magnetic-field optimization as this ensures the effect of the magnetic-field inhomogeneity to the reduced-cyclotron frequency is negligible.

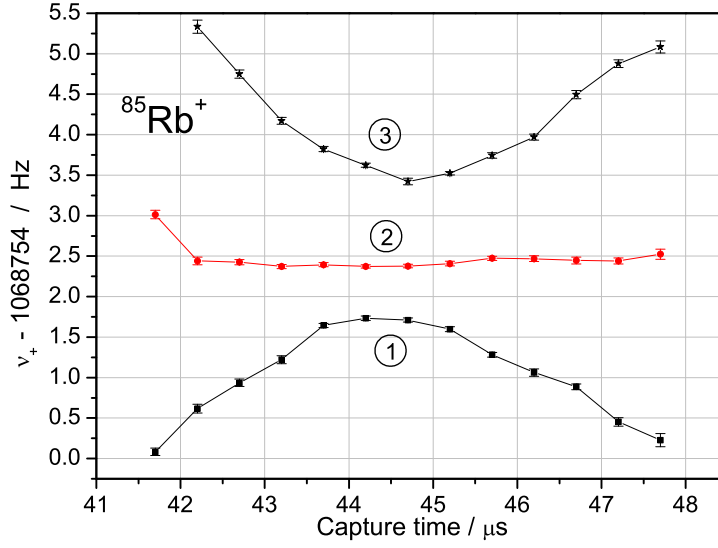


Figure 3.37: The reduced cyclotron frequency as a function of the capture time in the Precision Trap for different values of the correction tube voltage: 1.250 V (1), 1.120 V (2) and 0.950 V (3). The optimal value is 1.120 V.

3.4 Determination of the systematic uncertainty and data analysis

ISOLTRAP used a laser desorption carbon cluster ion source [Sch2002] to perform cross-reference mass measurements over a wide mass range from $A = 72$ to $A = 240$. In a cross-reference mass measurement, a measurement which is carried out using carbon clusters both as the reference ion and as the ion of interest, the true value of the ratio of the cyclotron frequencies $\nu_{c,\text{ref}}/\nu_c$ is exactly known. These measurements helped in understanding the sources and determining the extent of systematic uncertainties in real mass measurements. The measurements have shown that the accuracy limit of ISOLTRAP for the frequency ratio of any two nuclides is 8×10^{-9} [Kel2003].

Over a period of three months more than 350 cyclotron frequency measurements have been performed. The evaluation of these data yielded the determination of the mass dependent systematic uncertainty, the steady decrease of the magnetic-field strength, the uncertainty due to magnetic field fluctuations, and the residual systematic uncertainty. A detailed description of the performed measurements can be found in [Bla2002, Kel2003]. Here, only the results of the evaluation will be presented.

3.4.1 Determination of the systematic uncertainty

From the cyclotron frequency ratio measurement between the ion of interest (ν) and the reference ion (ν_{ref}), the mass m of the ion of interest can be derived using

$$m = \frac{\nu_{\text{ref}}}{\nu}(m_{\text{ref}} - m_e) + m_e, \quad (3.59)$$

where m_{ref} is a well-known reference mass while m_e is the electron mass. Since ISOLTRAP measures the mass of singly charged ions one has to correct for the electron mass. After the analysis ISOLTRAP gives the frequency ratio as the final result, so that at anytime the mass can be derived using the present best value of the reference mass. The uncertainties associated with the frequency ratio determination finally propagates to the mass uncertainties. As discussed in Section 3.1.3, the known systematic uncertainties that are associated with the ISOLTRAP experiment are either mass-dependent or dependent on the temporal fluctuation of the magnetic-field amplitude. The mass-dependent error can be estimated from cross-reference mass measurements over a wide mass range. The relative change of the magnetic-field magnitude in the Precision Trap can be determined by measuring the shift of the cyclotron frequency of a known mass over a long period of time. The changes in the magnetic-field amplitude are dependent on ambient conditions, like temperature, pressure, earth's magnetic field, stray fields around the experiment, presence of ferromagnetic materials near the magnet, etc.. Thus, it is difficult to keep it under full control. However, minimizing the time interval of the cyclotron frequency measurements between the reference ion and the ion of interest can reduce this systematic uncertainty.

Figure 3.38 shows the variation of the relative deviation of measured cyclotron frequency ratios from that of the true value $e(r)/r$ as a function of the mass difference

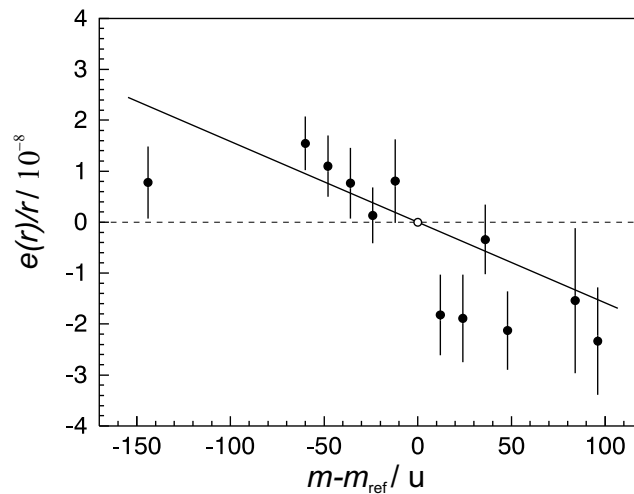


Figure 3.38: Deviation of the weighted mean of the frequency ratios of all carbon cluster cross-reference measurements as a function of the mass difference $m - m_{\text{ref}}$ between reference ion and ion of interest. The straight line is a linear least-squares fit to the data. Fullerene fragments of C_{10}^+ , C_{12}^+ , C_{20}^+ were used as references [Kel2003].

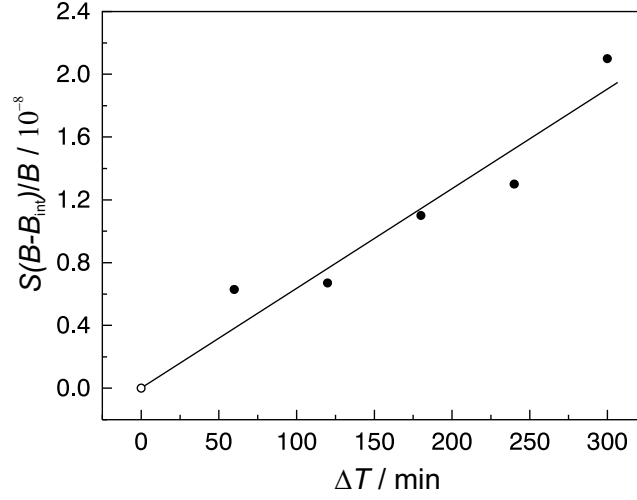


Figure 3.39: Relative standard deviation of the magnetic-field magnitude B about the interpolated value B_{int} for different time intervals ΔT between the two reference measurements, obtained via cyclotron frequency measurements of $^{85}\text{Rb}^+$. Since a data point represents standard deviation of a measured quantity, it cannot be assigned an uncertainty [Kel2003].

$m - m_{\text{ref}}$. Assuming linearity as a first-order effect a mass-dependent systematic uncertainty

$$\frac{u_m(r)}{r} = -1.6(4) \cdot 10^{-10} / u \cdot (m - m_{\text{ref}}), \quad (3.60)$$

was obtained [Kel2003]. Similarly from the short term magnetic field drift the time dependent systematic uncertainty was determined to be [Kel2003]

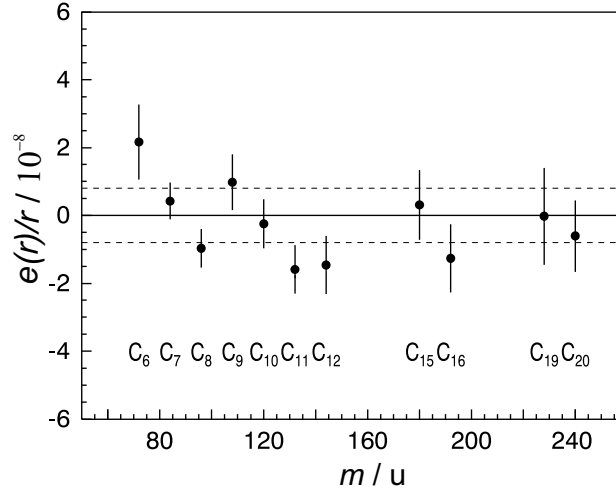


Figure 3.40: Dispersion of weighted means of the cyclotron frequency ratios for all carbon cluster cross-reference measurements from their true value after correction for the mass-dependent effect. The dashed lines indicate the residual systematic uncertainty that must be added to the uncertainties of the mean values in order to obtain a reduced χ^2 that obeys the condition $\chi^2/N \leq 1$ [Kel2003].

$$\frac{u_B(\nu_{\text{ref}})}{\nu_{\text{ref}}} = 6.35(45) \cdot 10^{-11} / \text{min} \cdot \Delta T. \quad (3.61)$$

These set of measurements (see Figure 3.39) were taken over a long time period but then divided into intervals of 15 min which is roughly the interval of ISOLTRAP's reference measurements. Incorporating both of these systematic uncertainties into the cross reference carbon cluster measurements, the residual systematic uncertainty of ISOLTRAP can be derived to be

$$\frac{u_{\text{res}}(r)}{r} = 8 \cdot 10^{-9}, \quad (3.62)$$

as shown in Figure 3.40 [Kel2003]. This uncertainty also constitutes the limit of accuracy for cyclotron frequency ratio measurements with the ISOLTRAP setup because all other uncertainties, being statistical in nature, can be reduced by an increased number of repeated measurements. A more recent analysis of masses around $A = 22$ indicates, that this limit can be even pushed further down by careful adjustment of the capture timing in the Precision Trap.

3.4.2 ISOLTRAP's standard analysis procedure

The typical approach adopted by ISOLTRAP to analyze its data will be briefly discussed here, with the mass measurement of ^{22}Mg as an example. A vivid description of the analysis around the mass $A = 22$ can be found in Chapter 4. ^{22}Mg is a β^+ emitter with a half-life of 3.857 s [Wap2003]. A number of well-known reference masses were used to calibrate the magnetic field. To discuss the general analysis method, only the measurements made with $^{39}\text{K}^+$ as reference will be presented. One $^{22}\text{Mg}^+$ TOF cyclotron resonance measurement between two $^{39}\text{K}^+$ cyclotron resonance measurements completes one mass measurement cycle. Figure 3.41 shows an example of the mean TOF as a function of the quadrupolar RF excitation frequency in the Precision Trap for $^{22}\text{Mg}^+$. The solid line is a least-square fit of the theoretically expected line shape [Kön1995b] to the data points with $\chi^2 \approx 1$. This fit determines the central frequency of the TOF resonance with its uncertainty. At this stage of the analysis, ISOLTRAP uses a technique called the count rate class analysis or z-class analysis [Kel2003] to take care of the cyclotron frequency shift due to the presence of any contaminant ion stored simultaneously in the trap. The data set is divided into more than two classes according to the number of simultaneously stored ions in the trap and the centroid frequencies are plotted as a function of the center of gravity of the count rate distribution in that class. This is shown in Figure 3.42 where the radioactive nuclide $^{22}\text{Na}^+$ is taken as an example. A linear least-squares fit is used to extrapolate the frequency towards a single stored ion in the trap. The two extrapolated points are for 0.25 and 0 count rate classes. An average of these two frequencies corresponds to about 15% detection efficiency. In some cases, like that of ^{22}Mg , the number of detected ions is within three per measurement cycle. Even considering 60% detector efficiency, this number is too low

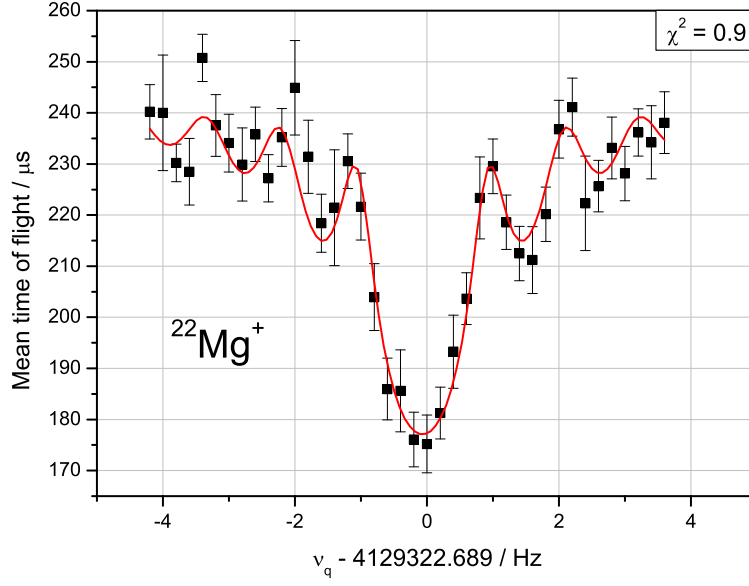


Figure 3.41: The mean time-of-flight variation as a function of the quadrupolar RF excitation frequency applied to the ring electrode segments of the Precision Trap. The resonance was obtained within 40 min collecting nearly 350 ions in total. The solid line is a least-square fit of the theoretically expected line shape [Kön1995b] to the measured data points.

to see any observable frequency shift due to contaminations within the ISOLTRAP uncertainties.

The ^{22}Mg - ^{39}K mass measurement cycle was repeated six times with about 350 ions for each $^{22}\text{Mg}^+$ TOF resonance. Due to the low ^{22}Mg yield and losses by the HRS mass separator, the reference measurements were performed within time intervals of about 90 min. To obtain the frequency ratio r as used in Eq. (3.59), the cyclotron frequency of the reference ion ($^{39}\text{K}^+$) is then interpolated linearly to the time of the actual measurement ($^{22}\text{Mg}^+$) [Kel2003]. The relative standard uncertainty due to the magnetic field drift $\frac{u_B(\nu_{\text{ref}})}{\nu_{\text{ref}}}$ [see Eq. (3.61)], for the time interval between two reference measurements, is then added quadratically to the relative standard uncertainty in the cyclotron frequency determination for the reference mass (^{39}K). The weighted mean of the measured ratios and its uncertainty is calculated using

$$\bar{r} = \frac{\sum_i \frac{r^i}{u_c^2(r^i)}}{\sum_i \frac{1}{u_c^2(r^i)}} \quad (3.63)$$

and

$$\frac{u(\bar{r})}{\bar{r}} = \frac{1}{\bar{r} \sqrt{\sum_i \frac{1}{u_c^2(r^i)}}}, \quad (3.64)$$

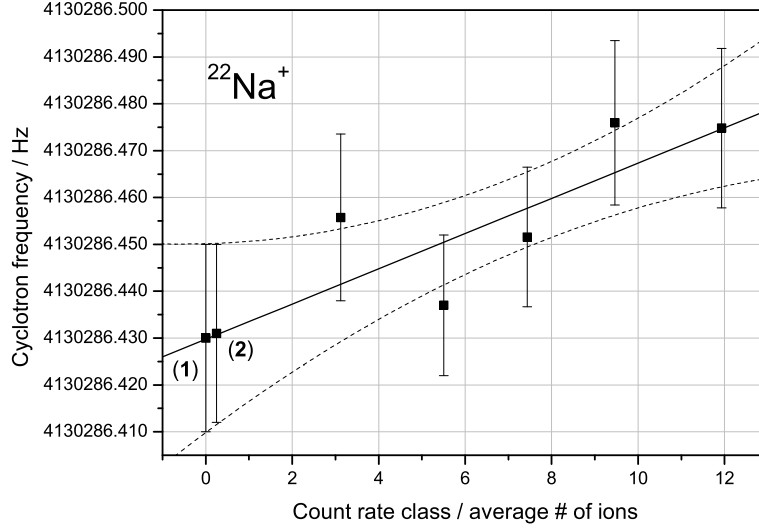


Figure 3.42: Cyclotron frequency as a function of the count rate class. The measurement was made with $^{22}\text{Na}^+$ ions from ISOLDE. The straight line is a linear least-squares fit to the data points. (1) and (2) are the extrapolated points for 0 and 0.25 count rate classes obtained out of the fit. The dashed lines are 1σ confidence bands of the fit.

where $u_c(r^i)$ denotes the uncertainty on the i th cyclotron frequency ratio determination after incorporating the uncertainty due to the magnetic field drift. This ratio is then corrected for the mass dependent systematic error $\frac{u_m(r)}{r}$ [see Eq. (3.60)]. The difference in the reference mass and the mass of interest is in this case 17 u. This corrected value is then the final frequency ratio and is expressed as

$$\bar{r}_{\text{corr}} = \bar{r} \left[1 + \frac{u_m(\bar{r})}{\bar{r}} \cdot \Delta m \right]. \quad (3.65)$$

The final relative standard uncertainty on the frequency ratio measurement is calculated by the quadrature rule of error addition which includes the above mentioned relative mass dependent systematic uncertainty (Eq. (3.60)) and the relative residual systematic uncertainty (Eq. (3.62))

$$\frac{u_c(\bar{r})}{\bar{r}} = \sqrt{\left[\frac{u(\bar{r})}{\bar{r}} \right]^2 + \left[\frac{u_m(\bar{r})}{\bar{r}} \right]^2 + \left[\frac{u_{\text{res}}(\bar{r})}{\bar{r}} \right]^2}. \quad (3.66)$$

The mass of ^{22}Mg is then derived from the best known value of the mass of ^{39}K [Wap2003], using Eq. (3.59). In this case the obtained mass value is $m(^{22}\text{Mg}) = 21.99957090(30)$ u.

3.5 Performance of the ISOLTRAP spectrometer

During the last three years, the performance of the Penning trap mass spectrometer ISOLTRAP in respect to efficiency, accuracy, accessible half-life, and resolving power

has been considerably enhanced. These breakthroughs in mass spectrometry of radionuclides are briefly described in the following.

3.5.1 Absolute mass measurements

Since the unified atomic mass unit is defined as $1/12$ of the mass of ^{12}C , carbon clusters provide an ideal mass reference for absolute mass measurements: They eliminate by definition the uncertainty of the mass of the reference ion. The molecular binding energies of the carbon clusters, being of the order of $V_b < 10^{-9}$, can be neglected at the present level of ISOLTRAP's precision. To perform absolute mass measurements at ISOLTRAP, a carbon cluster reference ion source has been developed and implemented (see Section 3.2.6).

3.5.2 Accuracy

Until the year 2002 the combined uncertainty was estimated conservatively to be $\delta m/m \approx 1 \cdot 10^{-7}$ [Bol1996], which includes such uncertainties as caused by inhomogeneities in the magnetic and electric fields (see Section 3.1.3), by magnetic field drifts or fluctuations, and the mass dependent systematic uncertainty steaming from the difference in mass Δm between the investigated ion and reference ion.

The carbon cluster cross reference measurements [Bla2002, Kel2003] allowed us to study the various contributions of different systematic effects to the combined uncertainty of a frequency ratio determination (see Section 3.4.1). This investigation yielded a relative mass-dependent cyclotron-frequency-ratio shift as low as $-1.6(4) \times 10^{-10} / u \cdot (m - m_{\text{ref}})$ which is corrected as well as added to the final uncertainty. Once all known effects are taken into account, the remaining uncertainty is found to be $8 \cdot 10^{-9}$. This also represents the current limit of the accuracy of our setup [Kel2003]. A better understanding and correction of the imperfections in the trap can even push further down the accuracy limit, as it was recently observed from a mass evaluation around $A = 22$ [Muk2004].

3.5.3 Efficiency

The total efficiency ϵ_{tot} of the ISOLTRAP apparatus can be expressed as

$$\epsilon_{\text{tot}} = \epsilon_{\text{cap}} \cdot \epsilon_{\text{bun}} \cdot \epsilon_{\text{trans}} \cdot \epsilon_{\text{det}}, \quad (3.67)$$

where ϵ_{cap} , ϵ_{bun} , ϵ_{trans} , and ϵ_{det} are the capturing, bunching, transport, and detection efficiencies at different sections of the apparatus. Since for the two Penning traps the capturing and trapping efficiencies are almost close to unity and the transfer efficiency is close to 90%, ϵ_{tot} is mainly determined by the RFQ cooler and buncher capturing and bunching efficiency. The installation of the RFQ trap as well as a complete re-alignment of the setup resulted in an increase of the overall efficiency of the ISOLTRAP spectrometer by several orders of magnitude. It reaches now about

1 – 5% for stable or long-lived nuclides as determined in November 2001 from the ratio of the number of ^{36}Ar ions observed by the MCP5 detector (see Figure 3.14) to the number of ions measured at the focal plane of the ISOLDE separator. For very short-lived nuclides such as ^{32}Ar with $T_{1/2} = 98$ ms, an overall efficiency of about 0.1% was achieved, mainly due to additional decay losses [Bla2003a]. The efficiency can still be improved by the installation of a new detector system as mentioned in Section 3.2.7 and by an efficiency increase of the RFQ.

3.5.4 Half-life

As discussed in Section 3.3.1, the total time needed for a single measurement cycle is mainly given by the time duration of the RF excitations needed for cleaning and centering in the Purification Trap and for coupling of the radial motions in the Precision Trap. The second one is a trade off since this time duration also determines the line-width of the TOF resonance. Therefore, an alternative measurement cycle with a total cycle time of only about 200 ms was developed. The nuclide with the shortest half-life measured until now is ^{74}Rb with a half-life of only 65 ms [Kel2004].

3.5.5 Resolving power

Accurate high-precision mass measurements with Penning traps require clean beams to avoid systematic errors in the mass determination arising from a Coulomb interaction of different ion species in the trap. To this end, in the Purification Penning Trap of ISOLTRAP, a mass selective cooling technique is employed [Sav1991]. A mass resolving power of $10^4 - 10^5$ can be achieved which is sufficient to resolve and separate isobaric contaminants even close to stability, provided the ratio of the unwanted-to-wanted species is below ≈ 300 . For higher ratios in the Purification Trap, space charge effect of the unwanted ion species restricts the buffer gas cooling

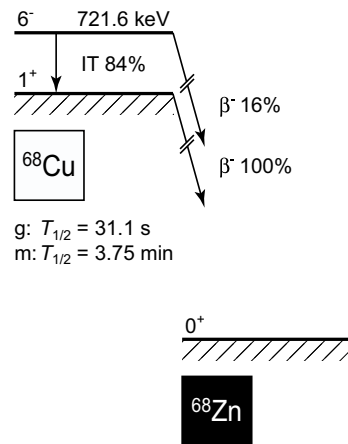


Figure 3.43: The low-energy nuclear level scheme of ^{68}Cu [Bla2004]. Indicated are configuration assignments, level energies, half-lives $T_{1/2}$, and decay modes taken from [Wap2003]. ^{68}Zn is stable.

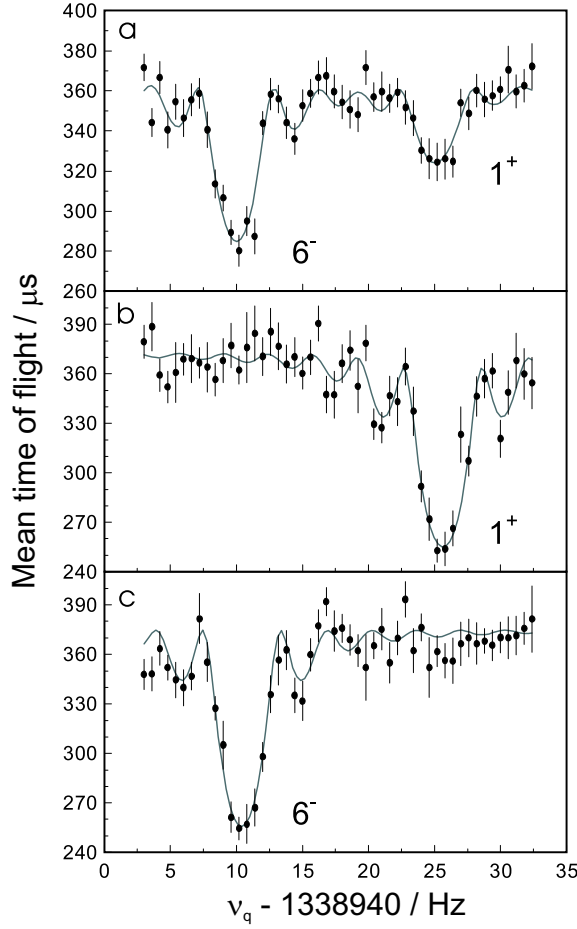


Figure 3.44: The Time-Of-Flight (TOF) resonance for (a) both the isomeric 6^+ and the ground 1^- state, (b) the isolated ground state while the isomeric state is cleaned by dipolar reduced cyclotron excitation, and (c) the isolated isomeric state while the ground state is cleaned. In all three spectra the solid line is the fit of the theoretical function to the data [Kön1995b].

technique as described in Section 3.2.4. The resolving power in the Purification Trap is strongly correlated to the buffer gas pressure in the trap. A lower pressure results in higher resolving power provided the pressure is enough to cool the ions within acceptable time. So the preparation of a clean beam is a compromise with the half-life of the radionuclide of interest.

An important issue in direct mass measurements is to resolve isomeric states since nearly one third of the nuclides in the nuclear chart have long-lived isomeric states with - in many cases - unknown excitation energies. To achieve this, a very high resolving power is required. An empirical formula for the resolving power is given by [Bol2001]

$$R = m/\Delta m = \nu_c/\Delta\nu_c \approx 1.25 \cdot \nu_c \cdot T_q, \quad (3.68)$$

where $\Delta\nu_c$ is the FWHM of the resonance. A resolving power of $R \approx 10^6$ is reached in the Precision Penning Trap for ions with mass number 100 and with an excitation

time of $T_q = 1$ s, as typically used in on-line experiments.

The dipolar cleaning procedure described in Section 3.3.2 is often adopted to get rid of isomers which cannot be resolved by the Purification Trap. One such example is the mass measurements performed on the isomeric as well as the ground state of ^{68}Cu [Bla2004]. The low-energy nuclear level structure for this nuclide is shown in Figure 3.43. It has one low lying isomeric state 6^- while its ground state is 1^+ . Both decay via β^- -decay to the ^{68}Zn ground state. In Figure 3.44, the time-of-flight resonances are plotted showing in (a) the mixture of both states as delivered by ISOLDE. To avoid shifts in the determination of the cyclotron frequency due to the presence of contaminants (here the isomers), a dipolar RF excitation at the reduced cyclotron frequency of the unwanted isomer was applied. It resulted in an isolated state giving only one resonance as shown in Figure 3.44(b) and (c). It shows the strength of this cleaning procedure adopted in the Precision Trap at ISOLTRAP to prepare isomerically pure ion samples. This possibility along with laser and decay spectroscopy measurements recently allowed to solve the state assignment problem of ^{70}Cu by the ISOLTRAP mass spectrometer [Roo2004].

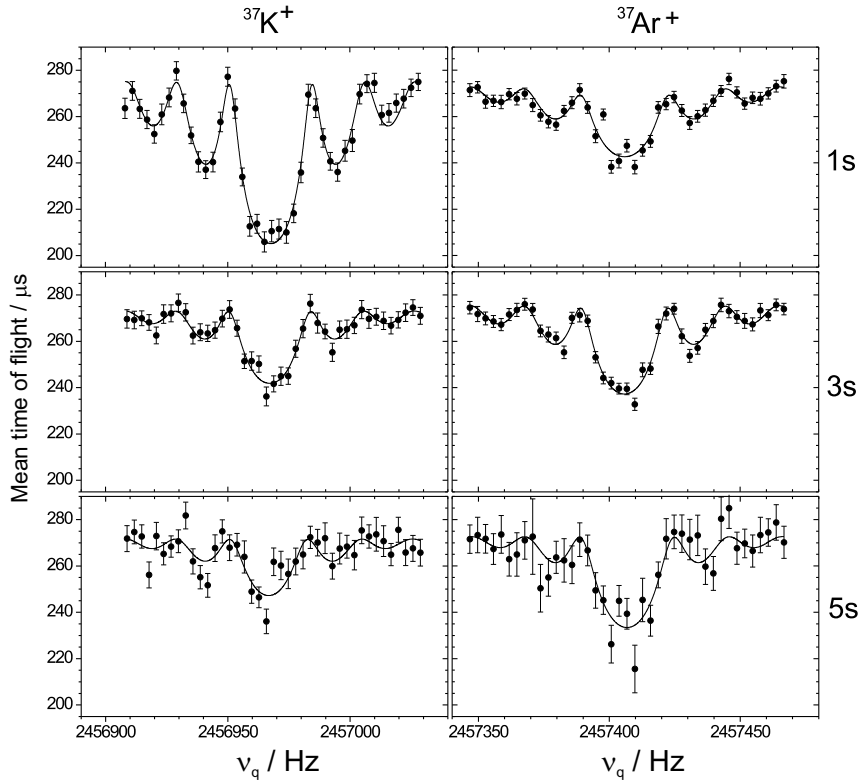


Figure 3.45: The Time-Of-Flight (TOF) resonances for $^{37}\text{K}^+$ (mother) and $^{37}\text{Ar}^+$ (daughter) for three different waiting times in the Purification Penning Trap of ISOLTRAP [Her2004].

3.5.6 Applicability

The ISOLTRAP spectrometer is capable to measure masses of all nuclides produced at ISOLDE provided their half-life is ≥ 50 ms and the production rate is ~ 100 ions per proton pulse. These numbers are limited mainly by the length of the measurement (preparation) cycle and the total efficiency of the present setup. The main drawback of the ISOL facility, as mentioned, in Chapter 2 is the inability to provide refractory elements. Recently, ISOLTRAP has demonstrated a new technique called “mass spectrometry with in-trap-decay products”, by which masses of these elements can be measured after they are produced by β -decay of their non-refractory mother in the ISOLTRAP Purification Trap. The pilot experiment at ISOLTRAP was performed by storing $^{37}\text{K}^+$ with a half-life of 1.2 s [Wap2003] in the Purification Trap for a few seconds until the largest part of the stored ions decayed into $^{37}\text{Ar}^+$ (the daughter nucleus). The mass of the so prepared ^{37}Ar ions was then measured in the Precision Trap [Her2004].

Figure 3.45 demonstrates the comparative TOF resonances for the mother and daughter ions after 1, 3, and 5 seconds of waiting time in the Purification Trap. It shows that with longer waiting times the TOF effect (see Section 3.1.3) increases for the daughter nuclide while it decreases for the mother nuclide due to the change in their relative abundances. From these measurements one can extract the nuclear half-life of the decaying mother nuclide, by careful understanding of the systematic uncertainties. Such uncertainties may arise due to loss of ions from the gas-filled Purification Penning Trap by mechanisms other than nuclear decays [Her2004].

With the installation of the new detector system (see Section 3.2.7) the present efficiency can be improved by more than a factor of two, allowing to access more exotic shorter-lived nuclides. Higher-order excitation schemes as well as the implementation of the Ramsey technique are now under investigation in order to shorten the total cycle time as well as to increase the resolving power.

Chapter 4

Mass evaluation around $A = 22$

Mass measurements with a relative mass uncertainty of better than 1.5×10^{-8} were performed on ^{22}Mg and its reaction partners ^{21}Na and ^{22}Na with the ISOLTRAP Penning trap mass spectrometer at ISOLDE, CERN, yielding the mass excesses $D(^{22}\text{Mg}) = -399.92(27)$ keV, $D(^{21}\text{Na}) = -2184.71(21)$ keV, and $D(^{22}\text{Na}) = -5181.56(16)$ keV [Muk2004]. The importance of these results is twofold: First, a comparative half-life (Ft value) has been obtained for the superallowed β decay of ^{22}Mg to further test the conserved-vector-current (CVC) hypothesis. Second, the resonance energy for the ^{21}Na proton capture reaction has been independently determined, allowing direct comparisons of observable γ radiation in nova explosions with the yield expected from models.

The data taking period covered three separate beamtimes. Table 4.1 shows the target-ion sources used for the production of the radionuclides during these beamtimes. The first beamtime lasted for 5 days where ^{22}Mg , ^{22}Na , ^{23}Na , and ^{24}Mg atoms were produced by bombarding a 19-g/cm^2 Ti-foil target (rolls of $30\text{-}\mu\text{m}$ foil) with 1.4-GeV protons from the CERN Proton Synchrotron Booster. The Mg isotopes were selectively laser-ionized with the ISOLDE resonance ionization laser ion source [Kös2003] and Na was surface ionized at the 2100°C hot W ionizer. ^{21}Na was measured in a separate run that lasted for 24 hours. It was produced from a standard ISOLDE $\text{UC}_x/\text{graphite}$ target with a W surface ionizer. The ions were accelerated to 60 keV and mass-separated in the high-resolution mass separator (HRS). The yield of ^{22}Mg was $3.1 \times 10^5/\mu\text{C}$, that of ^{22}Na about $10^9/\mu\text{C}$. For ^{22}Mg the HRS was operated at a mass resolving power of $m/\delta m \approx 4000$ in order to suppress the more abundant ^{22}Na , improving the ratio of ^{22}Mg to ^{22}Na to about $1/200$. The suppres-

Table 4.1: General characteristics and production yields of the radioactive nuclides used.

* RILIS denotes Resonance Laser Ion Source.

Nuclei	$T_{1/2}$	Target	Ion source	Yields/ μC
^{21}Na	22.49(4) s	$\text{UC}_x/\text{graphite}$ (13g/cm^2)	W surface	1.80×10^4
^{22}Na	2.6019(4) y		W surface	10^9
^{22}Mg	3.857(9) s	Ti-foil	RILIS*	3.1×10^9

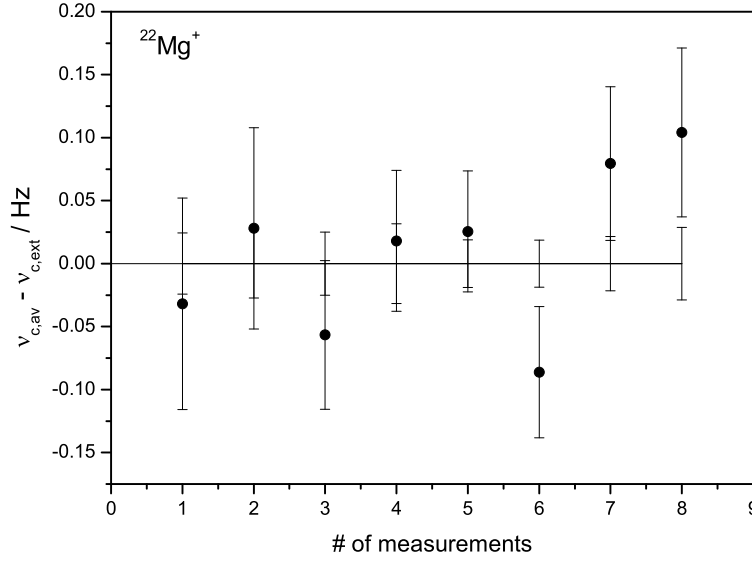


Figure 4.1: The difference in cyclotron frequencies without ($\nu_{c,av}$) and with the zeroth extrapolated ($\nu_{c,ext}$) count rate class analysis as described in Section 3.4.2. The zero line with error bars represents the results of $\nu_{c,av}$.

sion of the remaining ^{22}Na contaminants was achieved in ISOLTRAP’s Purification Penning Trap. Any residual contamination still present in the Precision Penning Trap would lead to a cyclotron frequency shift which increases with an increased number of ions stored simultaneously. Such an effect was excluded in the course of the standard analysis procedure [Kel2003], as mentioned in Chapter 3. No such dependence was found for any of the studied nuclides. A summary of the count rate class analysis as described in [Kel2003] and in Section 3.4.2 for all measured ^{22}Mg cyclotron resonances is shown in Figure 4.1. The difference in the measured cyclotron frequency for all count rate classes as compared to the extrapolated value for near zero count rate class shows a random fluctuation about the zero line. This exhibits that simultaneously stored ions in the precision trap were only ^{22}Mg . Over the measurement period of about three days, eight resonances of ^{22}Mg were recorded, of which a typical example is shown in Figure 3.41. In order to have a frequency ratio link between the better known ^{37}K mass and the less precise ^{39}K mass, the necessary data was taken during a third beamtime dedicated to measure the isotopic chain of potassium using a similar target as for magnesium.

The frequency ratios measured (see Table 4.2) during three consecutive beamtimes were taken as input for a least-squares fit in order to evaluate the masses of the above mentioned nuclides. In addition, this evaluation allowed to extract the mass differences for the reaction partners ^{21}Na - ^{22}Mg and ^{22}Mg - ^{22}Na directly along with their uncertainties. The least-squares and maximum likelihood technique to be described below lead to the possibility of further understanding the present limit of the systematic uncertainty of ISOLTRAP. The flow-matrix [Aud1986] obtained by this technique helped in the identification of the “influence” and “significance” of

Table 4.2: The frequency ratios used as input data for the analysis. The mass values of the references are taken from [Wap2003]. The values of the masses that are used as input for the analysis are marked *. The uncertainties given are without the residual systematic uncertainty.

Nuclei	$T_{\frac{1}{2}}$	Reference	Reference mass / μ u	Frequency ratio r
^{22}Mg	3.857(9) s	^{22}Na	21994436.4 (4)	1.0002333826 (91)
^{22}Na	2.6019(4) y	^{23}Na	22989769.2809 (29)*	0.9567044060 (39)
^{22}Na	2.6019(4) y	^{24}Mg	23985041.700 (14)*	0.9170045076 (59)
^{22}Na	2.6019(4) y	^{39}K	38963706.68 (20)*	0.5644791231 (29)
^{22}Mg	3.857(9) s	^{39}K	38963706.68 (20)*	0.5646108630 (55)
^{39}K	STABLE	^{23}Na	22989769.2809 (29)*	1.694844629 (13)
^{39}K	STABLE	^{37}K	36973375.89 (10)*	1.0538322643 (54)
^{21}Na	22.49(4) s	^{23}Na	22989769.2809 (29)*	0.9133457067 (80)
^{21}Na	22.49(4) s	^{39}K	38963706.68 (20)*	0.5388964127 (29)
^{24}Mg	STABLE	^{23}Na	22989769.2809 (29)*	1.0432930227 (47)

each datum to the finally derived adjusted parameters of the fit. In the following the theoretical background of the evaluation, its application to our data and the implication of the results will be discussed.

4.1 General theory

The evaluation method adopted to perform a least-squares analysis of the experimental data is based on the procedure elaborated in [Aud1986]. Consider Q data q_i , $i = 1, \dots, Q$ and M set of parameters to be determined m_μ , $\mu = 1, \dots, M$ ($Q \geq M$), are related according to a matrix equation

$$\sum_{\mu=1}^M k_i^\mu m_\mu = q_i \pm dq_i, \quad (4.1)$$

where $q_i \pm dq_i$ is the derived datum for the i th measurement along with its uncertainty. q_i has to be an appropriately continuous and differentiable function in order to perform a least-squares fit [Ken1951, Ead1971] which allows to determine the parameters of a linear over-determined system along with their uncertainties. q_i can be expressed as $q_i(|m\rangle, dq_i)$, where $|m\rangle$ is the column vector of parameters m_μ . The measured i th datum is l_i with an uncertainty σ_i . As the uncertainties in our case have Gaussian distribution, the probability of one particular datum i having a value l_i is [Lin1961, Bra1970, Ead1971]:

$$P_i(|m\rangle) = \frac{1}{\sqrt{2\pi}\sigma_i} \exp \left\{ -\frac{1}{2} \left[\frac{l_i - q_i}{\sigma_i} \right]^2 \right\}. \quad (4.2)$$

The likelihood function for the set of data is given by

$$L(|m\rangle) = \prod_{i=1}^Q P_i(|m\rangle). \quad (4.3)$$

The principle of the analysis is to maximize this likelihood function which can be achieved when

$$S^2 = \sum_i \left(\frac{l_i - q_i}{\sigma_i} \right)^2 \quad (4.4)$$

is a minimum. In matrix notation this takes the form

$$S^2 = \langle l - q | \mathbf{W} | l - q \rangle, \quad (4.5)$$

where \mathbf{W} is the weight matrix $W_{ij} = \delta_{ij} \sigma_i^{-2}$. At the minimum, S^2 has a χ^2 distribution. So the solution of

$$\nabla_m S^2 = \nabla_m \langle l - q | \mathbf{W} | l - q \rangle = 0, \quad (4.6)$$

is the minimum. For a set of linear equations as we have here, the solution is unique since the coefficient matrix \mathbf{K} in Eq. (4.1) comprises constant and unique elements k_i^μ . Following the mathematical steps as in [Aud1986], the vector of the adjusted parameters/masses turns out to be

$$|\bar{m}\rangle = \mathbf{A}^{-1} \mathbf{K}^t \mathbf{W} |q\rangle = \mathbf{R} |q\rangle, \quad (4.7)$$

where the *normal* matrix

$$\mathbf{A} = \mathbf{K}^t \mathbf{W} \mathbf{K} \quad (4.8)$$

is a square matrix of the order M , positive-definite, symmetric, and regular and hence invertible [Lin1961]. \mathbf{K}^t represents the transpose of the matrix \mathbf{K} . The rectangular (M, Q) matrix \mathbf{R} is called the *Response* matrix. The diagonal elements of \mathbf{A}^{-1} represents the squared uncertainties on the adjusted masses while the non-diagonal elements $(a^{-1})_\mu^\nu$ are the correlations between masses m_μ and m_ν .

The adjusted data vector turns out to be

$$|\bar{q}\rangle = \mathbf{K} |\bar{m}\rangle. \quad (4.9)$$

The minimum uncertainties of the adjusted data can be calculated [Bra1970] in a similar way as in Eq. (4.6), to be the diagonal elements of

$$\mathbf{d}q = \sqrt{\mathbf{K} \mathbf{A}^{-1} \mathbf{K}^t}. \quad (4.10)$$

The flow-of-information matrix is another important tool to look into the quality of the data. It is defined as [Aud1986]

$$\mathbf{F} = \mathbf{R}^t \otimes \mathbf{K}. \quad (4.11)$$

An element F_i^μ of this matrix \mathbf{F} represents the *influence* of datum i on the adjusted parameter \overline{m}_μ . So a column of \mathbf{F} represents all the contributions brought by all data to a given adjusted parameter \overline{m}_μ while a line depicts all influences given by a single piece of datum q_i . The sum of the influences along a line is the *significance* of that datum.

4.1.1 Consistency of data

For an over-determined system ($Q > M$), if the precisions dq_i assigned to data q_i are indeed all accurate, the normalized deviation between adjusted data \overline{q}_i and input data q_i would have Gaussian distribution with $\sigma = 1$, and would generate [Bra1970, Wap2003]

$$\chi^2 = \sum_{i=1}^Q \left(\frac{\overline{q}_i - q_i}{dq_i} \right)^2 \quad (4.12)$$

equal to $Q - M$, the number of degrees of freedom, with precision $\sqrt{2(Q - M)}$.

The consistency can also be expressed in terms of normalized χ or the *consistency factor* or *Birge ratio* as

$$\chi_n = \sqrt{\chi^2 / (Q - M)}, \quad (4.13)$$

for which the expected value would be $1 \pm 1/\sqrt{2(Q - M)}$.

4.1.2 Applicability to our data

The result of a ISOLTRAP measurement is a frequency ratio r between a cyclotron frequency of a reference ion ν_{ref} and that of the ion of interest ν :

$$r = \frac{\nu_{\text{ref}}}{\nu}. \quad (4.14)$$

This measured ratio can be expressed in terms of the masses by

$$r = \frac{m - m_e}{m_{\text{ref}} - m_e}, \quad (4.15)$$

where m_e denotes the electron mass. Eq. (4.15) can be simplified into a linear equation in m :

$$m - r \cdot m_{\text{ref}} = m_e(1 - r). \quad (4.16)$$

It is modified to

$$m - C \cdot m_{\text{ref}} = (r - C)m_{\text{ref}} + m_e(1 - r), \quad (4.17)$$

in order to have the left side independent of r by introducing a factor $C = A/A_{\text{ref}}$. Including the uncertainties on the measured values, it takes the form:

$$m - C \cdot m_{\text{ref}} = (r - C)m_{\text{ref}} + m_e(1 - r) + \left\{ (r - C)\delta m_{\text{ref}} + m_{\text{ref}}\delta r \right\}, \quad (4.18)$$

where the term $m_e \cdot \delta r$ is neglected and the uncertainty is mainly dominated by $m_{\text{ref}}\delta r$. Eq. (4.18) can now be compared with Eq. (4.1). Ten frequency ratios were measured between 7 masses which thus form a linear over-determined system. Since in our case

$$q_i = (r - C)m_{\text{ref}} + m_e(1 - r) \quad (4.19)$$

is a continuous and differentiable function, we can follow all the steps shown in Section 4.1 in order to apply a least-squares fit to our data.

4.2 The mass evaluation

The input for the mass evaluation around the mass of ^{22}Mg came from 10 frequency ratio measurements. These ratios were taken for different combinations of the following nuclides ^{21}Na , ^{22}Na , ^{22}Mg , ^{23}Na , ^{24}Mg , ^{39}K , and ^{37}K under the condition that they were measured successively in time with one frequency measurement of the ion of interest between two measurements of the reference ion. Out of these 7 nuclides, masses of ^{23}Na , ^{24}Mg , ^{39}K , and ^{37}K are known with an uncertainty better than $2 \times 10^{-7}\text{u}$ [Wap2003]. In particular the nuclei ^{23}Na and ^{24}Mg are known to better than $1 \times 10^{-8}\text{u}$. The input values are tabulated in Table 4.2 while the co-efficient matrix is given as

$$\mathbf{K} = \begin{pmatrix} {}^{22}\text{Na} & {}^{22}\text{Mg} & {}^{23}\text{Na} & {}^{24}\text{Mg} & {}^{39}\text{K} & {}^{37}\text{K} & {}^{21}\text{Na} \\ 0 & -1 & 0 & 0 & 0 & 0 & 1 \\ -1 & 1 & 0 & 0 & 0 & 0 & 0 \\ -1 & 1 & 0 & 0 & 0 & 0 & 0 \\ 1 & 0 & -0.9565217391 & 0 & 0 & 0 & 0 \\ 1 & 0 & 0 & -0.91666667 & 0 & 0 & 0 \\ 1 & 0 & 0 & 0 & -0.5641025641 & 0 & 0 \\ 0 & 1 & 0 & 0 & -0.5641025641 & 0 & 0 \\ 0 & 0 & -1.6956521739 & 0 & 1 & 0 & 0 \\ 0 & 0 & 0 & 0 & 1 & -1.054054054 & 0 \\ 0 & 0 & -0.91304347826 & 0 & 0 & 0 & 1 \\ 0 & 0 & 0 & 0 & -0.5384615384 & 0 & 1 \\ 0 & 0 & -1.0434782608 & 1 & 0 & 0 & 0 \\ 0 & 0 & 1 & 0 & 0 & 0 & 0 \\ 0 & 0 & 0 & 1 & 0 & 0 & 0 \\ 0 & 0 & 0 & 0 & 1 & 0 & 0 \\ 0 & 0 & 0 & 0 & 0 & 1 & 0 \end{pmatrix}$$

The first two lines of the \mathbf{K} -matrix originate from mass difference values of ${}^{21}\text{Na}$ - ${}^{22}\text{Mg}$ and ${}^{22}\text{Mg}$ - ${}^{22}\text{Na}$, since these are finally needed from the analysis. The initial uncertainties on these two data were kept to 1×10^{-6} so that they practically do not contribute to the least-squares adjustment but finally come out as adjusted data with their uncertainty according to Eq. (4.9) and (4.10). The last four lines came from input mass value relations of the four precisely known nuclei [Wap2003]. The remaining 10 rows are from the frequency relations according to Eq. (4.18).

The uncertainties on the measured data used as input are given in Table 4.2. In addition a residual systematic uncertainty was added quadratically and was varied until a consistency factor χ_n exactly equal to unity was obtained. For all the matrix calculations, the Mathematica 5.0 computer program of Wolfram Research was used on a 32-bit Intel[®] PC.

4.2.1 Least-squares adjustment results

Following the steps as mentioned in Section 4.1, the adjusted masses along with their uncertainties are obtained. In addition, the two mass differences along with their uncertainties are obtained following the Eqs. (4.9) and (4.10) for the adjusted data. The final result of the least-squares adjustment in terms of mass excesses is shown in Table 4.3. The deviation of the AME2003 mass excess values from that of the ISOLTRAP values are plotted in Figure 4.2. The four precisely known masses ${}^{23}\text{Na}$, ${}^{24}\text{Mg}$, ${}^{37}\text{K}$, and ${}^{39}\text{K}$ which are used as the input for the adjustment do not change. However, for ${}^{39}\text{K}$, it is even possible to reduce the uncertainty compared to that given in AME2003 [Wap2003]. The mass excess for ${}^{21}\text{Na}$ agrees well with the AME value [Wap2003], but with a reduced uncertainty of only 210 eV. There

Table 4.3: The mass excesses of the nuclei after the adjustment as compared to their values taken from the Atomic Mass Evaluation (AME2003) [Wap2003]. The last column gives the difference between the ISOLTRAP masses and those of AME2003.

Nuclei	Adjusted mass excess /keV	AME mass excess /keV	(IS-AME) /keV
^{21}Na	-2184.71 (21)	-2184.2 (7)	-0.51
^{22}Na	-5181.56 (16)	-5182.4 (4)	0.84
^{22}Mg	-399.92 (27)	-397.0 (1.3)	-2.92
^{23}Na	-9529.8535 (27)	-9529.8536 (27)	0.0001
^{24}Mg	-13933.565 (13)	-13933.567 (13)	0.002
^{37}K	-24800.21 (9)	-24800.20 (9)	-0.01
^{39}K	-33807.16 (16)	-33807.01 (19)	-0.15

are remarkable deviations of the AME values for ^{22}Na and ^{22}Mg which helped in solving some of the ambiguities regarding these masses derived indirectly in former experiments.

Our result for the mass of ^{22}Na agrees well with a value deduced from $^{21}\text{Ne}(p,\gamma)^{22}\text{Na}$ resonances [Ant1970]. It disagrees by 2.3σ with the weighted mean of two β -end-point measurements using the $^{22}\text{Na}(\beta^+)^{22}\text{Ne}$ decay [Bec1968, Gil1972].

A comparison of our result for the ^{22}Mg mass excess with previous data and one new data is shown in Figure 4.3. The mass excess of ^{22}Mg in AME2003 is derived from two (p,t) reaction Q values [Har1974, Nol1974] for which the reaction energies of

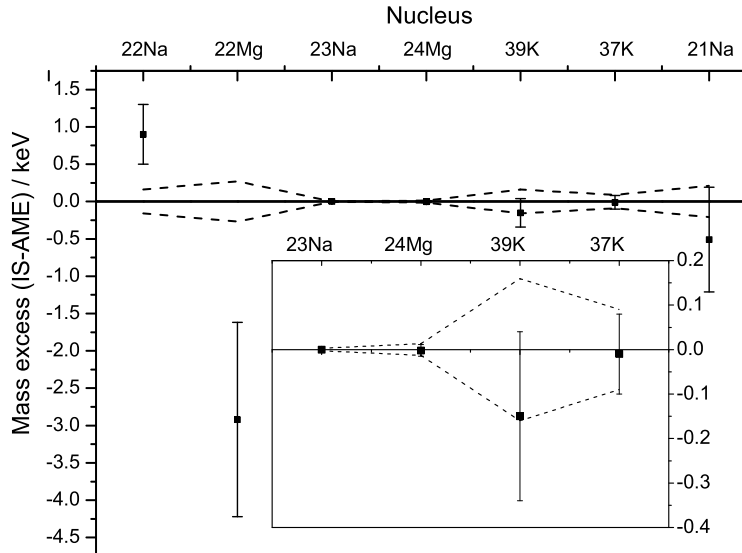


Figure 4.2: The dashed error band along the zero line shows the uncertainty of the ISOLTRAP (IS) measurement. The scattered squares exhibit the deviation of the AME [Wap2003] values along with their error bars. The inset shows part of the data enlarged.

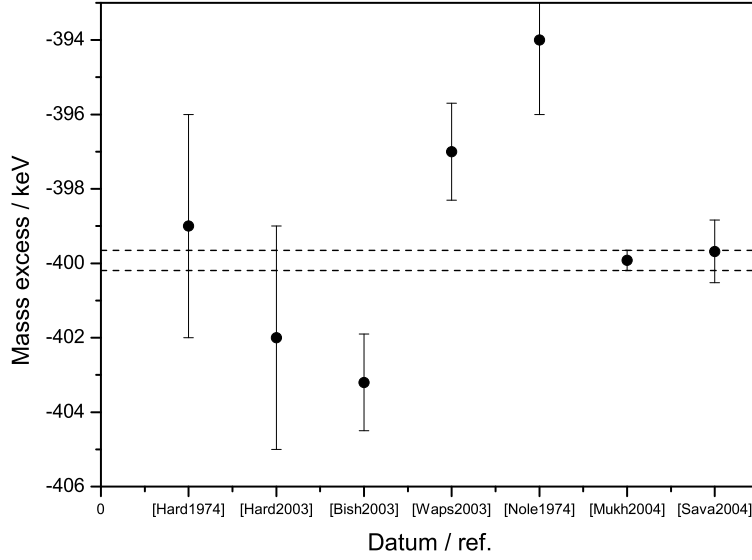


Figure 4.3: Comparison of the mass excesses of ^{22}Mg as reported by different groups including the AME2003 [Wap2003]. The dashed lines represent the error band of our value as reported in [Muk2004].

the corresponding calibration reactions have changed in the meantime (Figure 4.3). While a recalibration of the value of Ref. [Nol1974] appears not to be feasible, the other [Har1974] was updated by Hardy *et al.* [Har2003], resulting in a lower mass excess. The result from Ref. [Bis2003] also indicated that ^{22}Mg was probably more bound, a conclusion that is confirmed by our measurement. There has recently been another direct mass measurement performed on ^{22}Mg and ^{22}Na [Sav2004] which agrees well with our values but with much lower precision.

4.2.2 Discussion

The least-squares analysis allowed to quantify the systematic error for the local mass region centered around $A = 22$. As mentioned in Section 3.3.4, the capture time in the precision trap is an important parameter that can contribute to the systematic error. For example, the value for the capture time of $18.4 \mu\text{s}$ for ^{39}K was measured in a similar way as shown Figure 3.35. During the experiment this value could only be set to an integer number of μs , therefore it was set in some cases to $18 \mu\text{s}$ while in some other cases to $19 \mu\text{s}$. A value of $18 \mu\text{s}$ falls in the plateau of the plot shown in Figure 3.35(B) but not a capture time of $19 \mu\text{s}$. This led to a slightly higher χ_n value of 1.3 instead of $\chi_n^{\text{theo}} = 1 \pm 0.2$ for 10 degrees of freedom. So we removed all the data with $19 \mu\text{s}$ capture time from our analysis and hence one of the mass links namely ^{24}Mg - ^{39}K , was also removed decreasing the degrees of freedom to 9. To accommodate for the residual systematic uncertainty due to the difference between the required and the actually set value of the capture time we quadratically added a systematic uncertainty to the mass dependent uncertainty and the residual

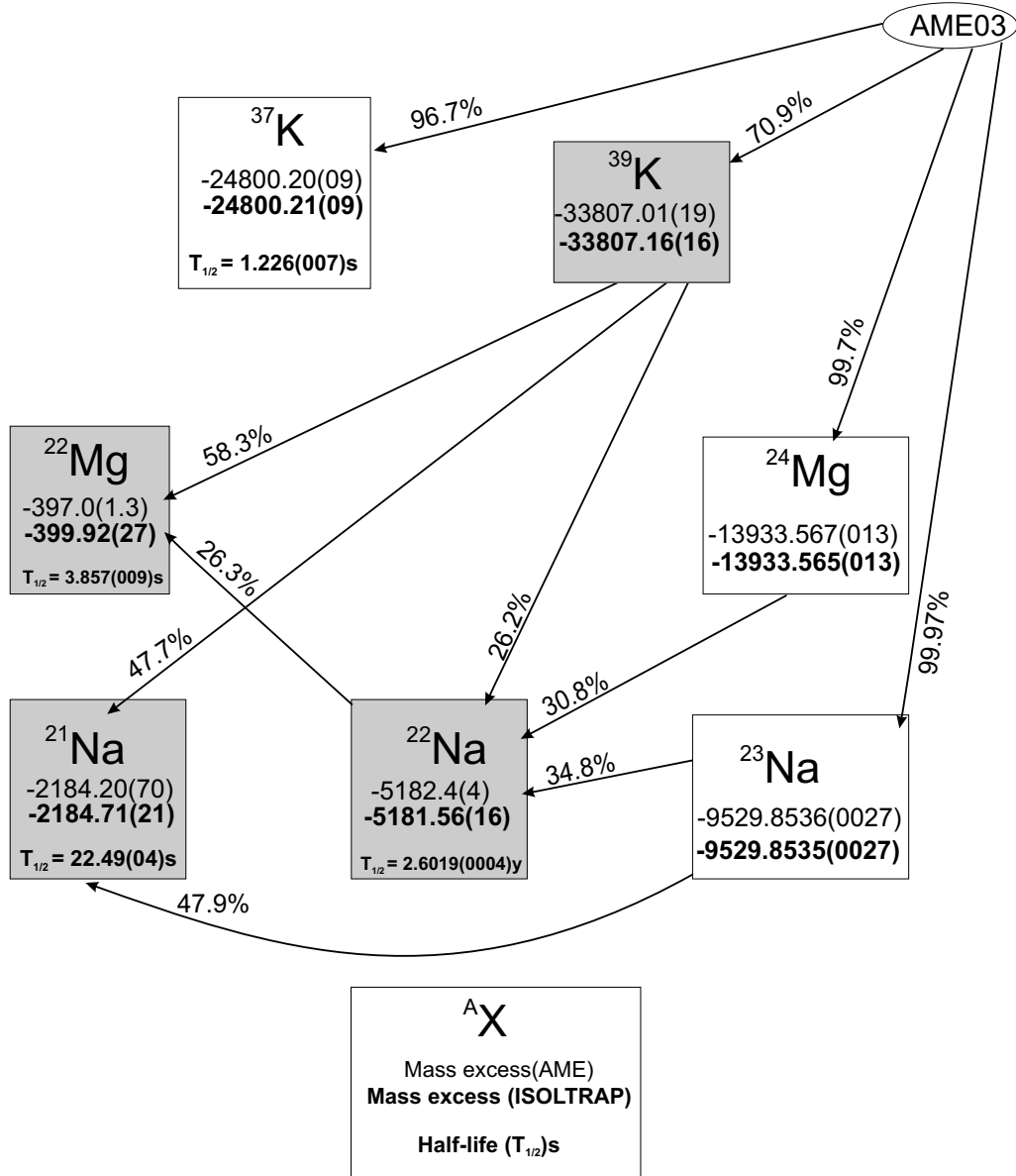


Figure 4.4: The influences on a mass value from different frequency ratio links in terms of percentage. Contributions below 10% are not shown. The total incoming flow for a given nuclei sums up to 100%. The shaded box represents ISOLTRAP's contribution in improving the mass uncertainties.

systematic uncertainty. This added value was varied so as to achieve $\chi_n = 1.0$, resulting a necessary total relative systematic uncertainty value of 1.3×10^{-8} .

The analysis therefore was very useful in pointing out the fact that the capture time needs to be adjusted well within a fraction of a μs . This has now already been implemented. The limit of this residual error holds only for this mass region.

The information-flow matrix \mathbf{F} obtained from the analysis gave an insight into which piece of data contributed to what extent in obtaining the final adjusted mass values. The significant contributors obtained from the \mathbf{F} -matrix are depicted in Figure 4.4.

The mass excess values for the very precisely known masses are fully influenced by the AME2003 [Wap2003]. The adjusted ^{22}Mg mass value has an influence of 60% from the knowledge of ^{39}K mass while an influence of about 30% comes from ^{22}Na mass link which in turn is feeded almost equally by very precise values of ^{23}Na , ^{24}Mg , and ^{39}K . It is important to note that this allowed us also to reduce the uncertainty of the ^{39}K mass by 30 eV which is mainly influenced by the ^{37}K and ^{23}Na mass values ($\sim 10\%$ each), the rest being from AME2003. The new ^{39}K mass value agrees well within the uncertainty of the AME2003 [Wap2003] value.

4.3 Physics implication

The mass of the short-lived radionuclide ^{22}Mg has recently been a subject of controversy in two different fields of physics: the superallowed β decay of ^{22}Mg to ^{22}Na [Har2003] and the $^{21}\text{Na}(p, \gamma)^{22}\text{Mg}$ reaction rate in classical novae [Bis2003]. In both contexts, the authors concluded that there was conflicting information on the ^{22}Mg mass. The value tabulated in the recent Atomic-Mass Evaluation (AME2003) [Wap2003] is derived from two discrepant thirty-year-old reaction Q value measurements. Clearly, an independent and direct high-precision measurement of the ^{22}Mg mass with an uncertainty well below 1 keV was required.

4.3.1 Contribution to test the CVC hypothesis

The CVC hypothesis holds that the (corrected) comparative half-lives Ft of all superallowed β decays are equal as a consequence of the assumed independence of the vector-current part of the weak interaction from the strong force. The determination of Ft requires precision measurements of the decay energy and the partial decay half-life, as well as detailed calculations of the associated isospin-symmetry-breaking (δ_C) and radiative corrections (δ_R) [Tow2002, Tow2003]. The comparative half-lives for nine superallowed $T = 1$ ($0^+ \rightarrow 0^+$) decays have been determined to a precision of $\approx 10^{-4}$ or better [Tow2003]. They agree well with each other within their uncertainties and yield a weighted mean value of $\overline{Ft} = 3072.2(0.9)(1.1)$ s, where the second uncertainty term represents a deviation in the calculation of δ_C by two different groups [Orm1995, Tow2002] and the first term contains all other uncertainty contributions.

The vector coupling constant G_V extracted from nuclear β decay, together with that from muon decay [Shr1978], yields the most precise value of the V_{ud} element of the Cabibbo-Kobayashi-Maskawa (CKM) matrix. Using this result for V_{ud} , the unitarity test of the CKM matrix currently fails by more than two standard deviations [Tow2003], a result which is also confirmed by the V_{ud} value obtained from neutron β decay [Abe2002]. Based on the realization that the uncertainty in V_{ud} is now mainly due to the calculated corrections, in particular the nuclear-structure-dependent terms, it has been pointed out [Tow2002] that these terms could be validated by measuring additional superallowed transitions covering a wider range of magnitudes of the correction terms. Of particular interest in this context are

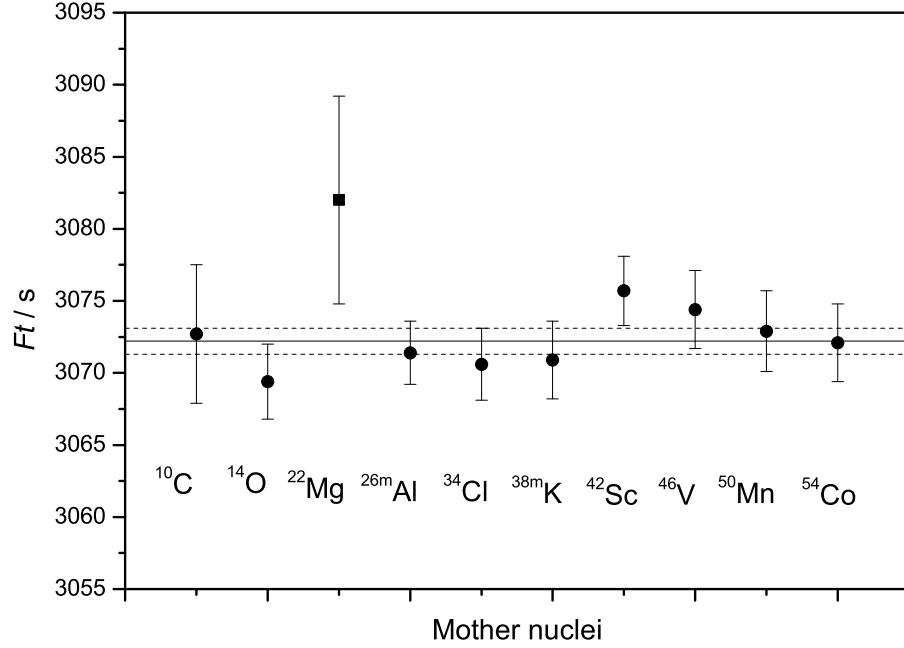


Figure 4.5: Comparative half-life for the decay $^{22}\text{Mg}(\beta^+)^{22}\text{Na}$ (square) compared with the high-precision data for the other nine nuclides ^{10}C – ^{54}Co (circles) [Tow2003]. The dashed lines indicate the confidence interval of the weighted mean $\overline{Ft} = 3072.2(9)$ s of the other data.

the even- Z , $T_z = -1$ nuclei with $18 \leq A \leq 42$ and the odd- Z , $T_z = 0$ nuclei with $A \geq 62$ [Tow2002]. We have lately addressed the $A = 74$ case that falls into the latter category [Kel2004]. This new result for the former ($A = 22$), for which important progress was recently made by Hardy *et al.* in the determination of the partial half-life [Har2003], is now presented here.

The least-squares adjustment provided directly the mass difference $D(^{22}\text{Mg}) - D(^{22}\text{Na}) = 4781.64(28)$ keV. From this mass-excess difference and the level energy $E_x = 657.00(14)$ keV for the 0^+ state in ^{22}Na [End1990], we obtain a decay energy for the superallowed decay of ^{22}Mg of $Q = 4124.64(31)$ keV, which corresponds to a statistical rate function $f = 418.48(19)$ [Tow2004]. Using the half-life $T_{1/2} = 3.8755(12)$ s, the branching ratio into the superallowed channel $R = 53.15(12)\%$ [Har2003], the corrections $\delta_R = 1.20(3)\%$ and $\delta_C = 0.265(15)\%$ [Tow2002], as well as an electron capture fraction of $P_{\text{EC}} = 0.07\%$ [Tow2004], this yields a comparative half-life of $Ft = 3082.0(7.2)$ s. Figure 4.5 shows this result alongside the existing high-precision data [Tow2003] and illustrates the agreement to within 1.3σ with their weighted mean $\overline{Ft} = 3072.2(9)$ s. The uncertainty is still about a factor 2.5 larger than those of the other nuclides, but this is now almost entirely due to the uncertainty of the branching ratio into the superallowed channel (94% contribution to the variance of Ft). In fact, a precise

measurement of R could improve the precision of Ft to better than 2 s. Under the assumption of CVC, the predicted branching ratio would be $R = 53.319(38)\%$.

4.3.2 Present status of the CKM unitarity

Since the last compiled data by the Particle Data Group (PDG) 2002 [Hag2002], there has been a number of development both in theory and experiment to check the unitarity of the CKM matrix. The matrix [Cab1963, Kob1973] relates the quark eigen states of the weak interaction with the quark mass eigen states (unprimed)

$$\begin{pmatrix} d' \\ s' \\ b' \end{pmatrix} = \begin{pmatrix} V_{ud} & V_{us} & V_{ub} \\ V_{cd} & V_{cs} & V_{cb} \\ V_{td} & V_{ts} & V_{tb} \end{pmatrix} \begin{pmatrix} d \\ s \\ b \end{pmatrix}$$

and, as such, the matrix is unitary. At present, the most precise test of unitarity is provided by the elements from the first row *i.e.*

$$V_{ud}^2 + V_{us}^2 + V_{ub}^2 = 1. \quad (4.20)$$

Any deviation from unitarity may either point to the necessity of extending the three-generation Standard Model or may lead to physics beyond the Standard Model [Tow2003].

This deviation is represented as

$$\Delta \pm \delta = 1 - (V_{ud}^2 + V_{us}^2 + V_{ub}^2). \quad (4.21)$$

The first matrix element comes usually from the superallowed nuclear β -decay together with the muon decay data as discussed in Section 4.3.1. It can also be derived from neutron decay or from pion decay. The main contribution to the uncertainty of V_{ud} obtained from the theoretical understanding of nuclear β -decay measurements comes from nuclear structure effects. Neutron and pion decays do not need nuclear-structure dependent calculations but they have other disadvantages. Neutron decay is not purely vector-like while the pion β -decay branch ($\pi^+ \rightarrow \pi^0 e^+ \nu_e$) is very weak ($\sim 10^{-8}$). So at present the most precise value for V_{ud} comes from the superallowed nuclear β decays.

The value of V_{us} comes from hyperon, $K \rightarrow \pi \mu \nu (K_{\mu 3})$, or from $K \rightarrow \pi e \nu (K_{e 3})$ decays. However, $K_{e 3}$ decay provides a smaller theoretical uncertainty [She2003]. The PDG [Hag2002] derives this element from a more than thirty-year-old $K_{e 3}$ data. The $|V_{us}|$ in case of $K_{e 3(\gamma)}^0$ decay is represented as

$$|V_{us}| = \left[\frac{128\pi^3 \Gamma(K_{e 3(\gamma)}^0)}{G_F^2 M_{K^0}^5 S_{EW} I_{K^0}} \right]^{\frac{1}{2}} \cdot \frac{1}{f_+^{K^0 \pi^-}(0)}, \quad (4.22)$$

where the relevant terms for the discussion here are the *form factor* $f_+^{K^0 \pi^-}(0)$ derived in the framework of chiral perturbation theory [Cir2002] and the decay width

$\Gamma(K_{e3(\gamma)}^0)$, which in turn is a function of the K^0 lifetime and $K_{e3(\gamma)}^0$ branching ratio. The same formula holds for $K_{e3(\gamma)}^+$ decay as well. Recently, the form factor has been reevaluated by the inclusion of $\mathcal{O}(p^6)$ terms where p denotes 4-momentum [Cir2004]. In addition, there has been recently a high-statistics K_{e3}^+ branching ratio measurement performed by the E865 collaboration at Brookhaven [She2003]. Unfortunately, for K_{e3}^0 decay there exists only the old data giving rise to two different values for $\Gamma(K_{e3}^0)$ depending on the procedure for the data treatment [Cir2004]:

$$\Gamma(K_{e3}^0)_{\text{fit}} = (7.50 \pm 0.08) \times 10^6 \text{s}^{-1} \quad (4.23)$$

$$\Gamma(K_{e3}^0)_{\text{average}} = (7.7 \pm 0.5) \times 10^6 \text{s}^{-1}. \quad (4.24)$$

Presently new experiments (CMD2, NA48, KLOE) [Cir2004] are in progress in order to clarify the situation.

The last element in the first row of the CKM matrix, V_{ub} , is derived from semi-leptonic decay of B mesons [Hag2002]. Since its value is very small it contributes negligibly to Eq. (4.21).

Table 4.4 summarizes the present status regarding the deviation (if any) from unitarity of the CKM matrix elements for the first row, V_{ub} is omitted. The deviation from unity along with their uncertainty is plotted in Figure 4.6. The present state of the available V_{us} data is very confusing since the K_{e3}^+ result deviates by $\sim 2\sigma$ from the K_{e3}^0 decay result. V_{us} from K_{e3}^+ decay along with the nuclear V_{ud} data confirms unitarity, but it is in conflict with K_{e3}^0 decay data, which shows more than 2σ deviation from unitarity. This situation will certainly improve with new K_{e3}^0 results, that will be coming from the experiments presently underway.

The explanation of the input data in the Table 4.4 and Figure 4.6 are explained below:

- (1) The values are as given in the PDG2002 [Hag2002].
- (2) V_{ud} from nuclear β -decay data [Tow2003] & V_{us} from PDG2002 [Hag2002].
- (3) V_{ud} from neutron decay [Tow2003] & V_{us} from PDG2002 [Hag2002].
- (4) V_{ud} from pion decay [Tow2003] & V_{us} from PDG2002 [Hag2002].
- (5) V_{ud} from nuclear β -decay data [Tow2003] & V_{us} is reevaluated by including $\mathcal{O}(p^6)$ loops for the form factor and $\Gamma(K_{e3}^0)_{\text{fit}}$ from Eq. (4.24) [Cir2004].
- (6) V_{ud} from nuclear β -decay data [Tow2003] & V_{us} is reevaluated by including $\mathcal{O}(p^6)$ loops for the form factor and $\Gamma(K_{e3}^0)_{\text{average}}$ from Eq. (4.24) [Cir2004].
- (7) V_{ud} from nuclear β -decay data [Tow2003] & for V_{us} the K_{e3}^0 lifetime is taken from PDG2002 [Hag2002] while the branching ratio is from preliminary data of KLOE [Sci2003, Cir2004] experiment. The quoted uncertainty is only statistical.

Table 4.4: The present global status of the CKM unitarity. The explanation for the sources of the input data are given in the text.

Input data	V_{ud}	δV_{ud}	V_{us}	δV_{us}	Δ	δ
(1)	0.9734	0.0008	0.2196	0.0026	0.0043	0.0019
(2)	0.974	0.0005	0.2196	0.0026	0.0031	0.0015
(3)	0.9745	0.0016	0.2196	0.0026	0.0021	0.0033
(4)	0.967	0.0161	0.2196	0.0026	0.0167	0.0312
(5)	0.974	0.0005	0.2153	0.0026	0.005	0.0015
(6)	0.974	0.0005	0.2182	0.0075	0.0037	0.0034
(7)	0.974	0.0005	0.2143	0.0025	0.0054	0.0014
(8)	0.974	0.0005	0.2186	0.0027	0.0035	0.0015
(9)	0.974	0.0005	0.2238	0.0033	0.0012	0.0018

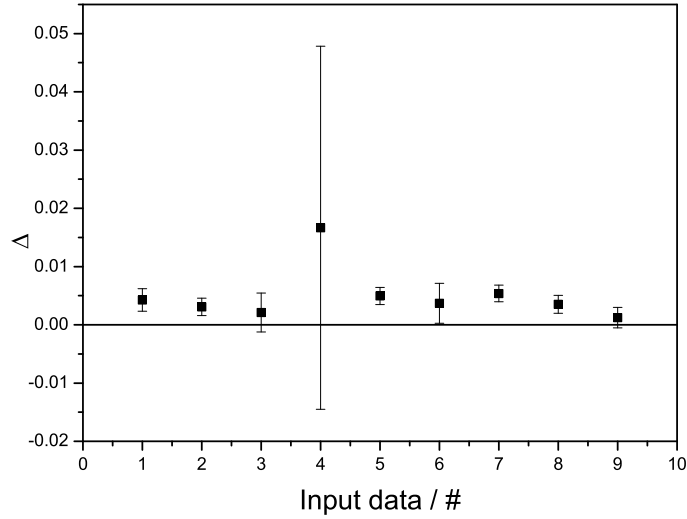


Figure 4.6: A comparison of the deviation from unitarity of the first row of the CKM matrix for different available input values of the V_{ud} and V_{us} elements. The source of each data is explained in the text.

- (8) V_{ud} from nuclear β -decay data [Tow2003] & V_{us} uses the decay width Γ from PDG2002 while the form factor is obtained by the inclusion of $\mathcal{O}(p^6)$ loops [Cir2004] for K_{e3}^+ decay.
- (9) V_{ud} from nuclear β -decay data [Tow2003] & V_{us} from recent result of the K_{e3}^+ branching ratio measurement experiment with the high statistics [She2003] and the lifetime is from PDG2002.

4.3.3 Contribution to nuclear-astrophysics

The other domain for which the mass of ^{22}Mg is important is nuclear astrophysics. As detailed knowledge of nuclear structure is necessary but not sufficient for the

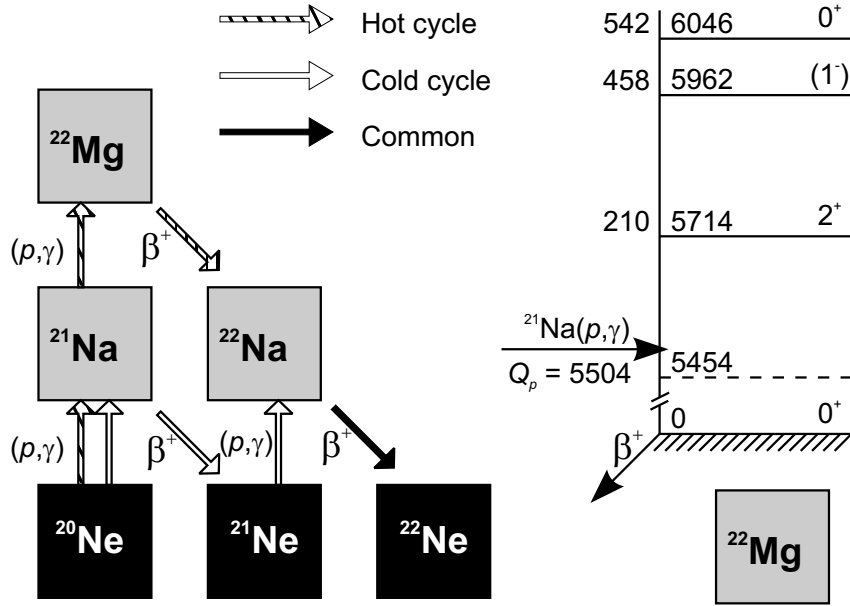


Figure 4.7: (left) “Hot” and “cold” reaction paths of the NeNa cycle. The bottom row (black boxes) are stable nuclides; (right) Level scheme of ^{22}Mg , showing the levels with astrophysical relevance [End1990]. The level energies E_x (center) are shown along with the center-of-mass energies $E_x - Q_p$ (left; both in keV) and the spin-parity (right).

constraint of stellar models, one of the most important quests in astrophysics is the definition of clear observable. Nova bursts are of particular interest due to their relative occurrence frequency and are viable candidates for observation with γ ray telescopes, as first pointed out by Clayton and Hoyle [Cla1974]. Nucleosynthesis in ONe nova explosions proceeds by radiative proton capture on abundant ^{20}Ne seed nuclei that ultimately produces the β -decaying nuclide ^{22}Na . The γ ray in question is emitted from the first excited state of its daughter ^{22}Ne at 1275 keV. All searches so far with several different instruments have failed to detect the ^{22}Na 1275-keV γ ray signature [Jea2001]. However, the expected frequency of ONe nova outbursts and the dependence of the flux on the spatial distribution have recently been revised [Jea2001] and the upper limits for the ejected ^{22}Na mass deduced from the absence of observed γ radiation are still compatible with current nova models.

The so-called NeNa cycle for the production of ^{22}Na can follow two possible paths, shown in Fig. 4.7(a), depending on the $^{21}\text{Na}(p, \gamma)^{22}\text{Mg}$ reaction rate and the temperature at the reaction site [Wie1986a].

In the “cold” cycle, ^{21}Na produced in the $^{20}\text{Ne}(p, \gamma)^{21}\text{Na}$ proton capture reaction β -decays to ^{21}Ne , which forms ^{22}Na through a second (p, γ) reaction. At higher temperatures, the proton capture on ^{21}Na is enhanced and ^{22}Mg is predominantly produced. In both cases, the β^+ decay chain proceeds through ^{22}Na to ^{22}Ne , but in the “cold” cycle the ^{22}Na production is delayed by the β decay of ^{21}Na , making more ^{22}Na available at a time when the nova envelope has become transparent to γ radiation. The quantity of ^{22}Na observable in these nova outbursts hence depends critically on the $^{21}\text{Na}(p, \gamma)^{22}\text{Mg}$ reaction rate, which is an exponential function of

the resonance energy E_R [Fow1967].

In current ONe nova models [Jos1999, Smi2000], a precise computation of the amount of ^{22}Na ejecta is hampered by the uncertainty of the $^{21}\text{Na}(p,\gamma)^{22}\text{Mg}$ reaction rate. Under nova conditions, it is expected to be dominated by one or several narrow resonances, in particular that into the 5714-keV 2^+ state [Wie1986a]. The resonance strength of the capture reaction can be obtained from shell structure calculations [Wie1986a, Wie1986b]. It has also recently been measured experimentally from the maximum thick-target yield by Bishop *et al.* [Bis2003], who found a discrepancy in the resonance energy of the 2^+ level which pointed to a probable deviation of the ^{22}Mg mass from the AME value.

Our mass measurements on ^{21}Na and ^{22}Mg yield a $^{21}\text{Na}(p,\gamma)^{22}\text{Mg}$ resonance energy into the 5713.9-keV 2^+ state of $E_R = 209.7(1.2)$ keV, somewhat higher than the value of 205.7(5) keV from the yield curve measurement [Bis2003]. A further reduction in the uncertainty of the resonance energy is currently hampered by the inadequate knowledge of the level energy of the aforementioned 2^+ state in ^{22}Mg . Our measurement indicates a slightly lower $^{21}\text{Na}(p,\gamma)^{22}\text{Mg}$ reaction rate at all temperatures than found in [Bis2003], but well within the uncertainties reported there. Our result therefore confirms their conclusion that the predicted final ^{22}Na content in ONe nova ejecta, and hence the γ ray flux, does not contradict the upper limits from observational searches. In addition to the independent determination of the resonance energy, our result should allow more detailed calculations of the resonance strength of the $^{21}\text{Na}(p,\gamma)^{22}\text{Mg}$ capture reaction as a complementary input for nova models.

Chapter 5

Conclusions

In the frame of this thesis, several technical developments have been addressed, *e.g.* to improve the characteristics of a radioactive ion beam and to perform absolute mass measurements. The experimental part includes high-precision mass measurements, mass evaluation procedure, and the impact of these results for further testing the Standard Model predictions and to derive important astrophysical observable.

Laser Ion Source Trap: Detailed simulation and calculation were performed to study the feasibility of a Laser Ion Source Trap (LIST) which combines the advantages of a resonance ionization laser ion source and an RFQ trap. Realistic approaches concerning the ion-atom interaction and the behavior of a hot graphite furnace with respect to ionization were adopted. Based on these calculations, a 10 cm long RFQ cooler and buncher was designed, constructed, and is presently in test phase [Brü2005, Wie2004].

As the calculations point out, there will be a major improvement in the beam emittance and purity with the installation of LIST at the online isotope separators like ISOLDE. Recent experimental results [Rau2004] indicate the advantage of the repeller electrode in suppressing the surface ionized unwanted isobars.

Towards absolute mass measurement: A carbon cluster laser ion source was designed, constructed, and tested to perform absolute mass measurements on radioactive nuclides using $^{12}\text{C}_n (n = 1, 2, \dots)$ as mass references for calibration purposes. It is now installed at the ISOLTRAP setup and allows to use carbon clusters as reference masses for online measurements. The source is efficient for ion transportation, highly flexible in terms of possible reference samples, and last but not least easy to operate under on-line conditions. The energy distribution of the ions created at an absolute energy of 2.5 keV was measured to be 20 eV which agrees well with ion trajectory simulations.

Mass measurements and evaluation around $A = 22$: Cyclotron frequency ratio measurements between different radioactive and stable nuclides in the region

of $A = 22$ were performed. Two contradicting values for the mass of ^{22}Mg derived from reaction kinematics were available. Therefore, it was necessary to perform a direct mass measurement on this nuclide. The importance of this nuclide being twofold, made the problem even more interesting. The other nuclides that are associated to these problems are ^{22}Na (superallowed β -decayed product) and ^{21}Na (reaction partner for (p, γ) reaction). In addition, cyclotron frequencies for ^{23}Na , ^{24}Mg , ^{39}K , and ^{37}K were also measured for calibration. A least squares fit method was then applied to extract from the measured cyclotron frequency ratios the masses and some required mass differences along with their uncertainties. Relative mass uncertainty $\sim 10^{-8}$ is achieved out of these measurements.

The mass of ^{22}Mg and its contribution for Standard Model tests: The performed analysis allowed to extract the Q value of the superallowed β decay $^{22}\text{Mg}(\beta^+)^{22}\text{Na}$ with an unprecedented precision. A comparative half-life of $Ft = 3082.2(9)$ was thereby derived for this superallowed β -decay which agrees within 1.3σ with the weighted mean of the high precision data available for 9 other such decays. A comparative view with presently available data on the unitarity of the CKM matrix is also given. The squared sum of the first row of the CKM matrix fails by $\sim 2\sigma$ from unity with values taken from the Particle Data Group 2002.

The mass of ^{22}Mg and its contribution to nuclear astrophysics: Our mass measurements on ^{21}Na and ^{22}Mg confirm the present $^{21}\text{Na}(p, \gamma)^{22}\text{Mg}$ reaction rate in an ONe nova burst but with much lower uncertainty. The present upper limit of the ejected γ ray flux from a ONe nova ejecta is found to be consistent with the present observational searches. Furthermore this result should allow more detailed calculations of the resonance strength of the $^{21}\text{Na}(p, \gamma)^{22}\text{Mg}$ capture reaction as a complementary input for nova models.

Bibliography

- [Abe2002] H. Abele, M. A. Hoffmann, S. Baeßler, D. Dubbers, F. Glück, U. Müller, V. Nesvizhevsky, J. Reich, and O. Zimmer. *Is the unitarity of the quark-mixing CKM matrix violated in neutron β -decay?* Phys. Rev. Lett. **88**, 211801 (2002).
- [Ant1970] A. Anttila, M. Bister, and E. Arminen. *Investigation of ^{22}Na excited states.* Z. Phys. **A234**, 455–464 (1970).
- [Aud1986] G. Audi, W. G. Davies, and G. E. Lee-Whiting. *A method of determining the relative importance of particular data on selected parameters in the least-squares analysis of experimental data.* Nucl. Instr. and Meth. **A249**, 443–450 (1986).
- [Aug1994] G. Auger et al. *A cyclotron as a high resolution mass spectrometer for fast secondary ions.* Nucl. Instr. and Meth. **A350**, 235–243 (1994).
- [Äys2001] J. Äystö. *Development and applications of the IGISOL technique.* Nucl. Phys. **A693**, 477–494 (2001).
- [Bec1968] E. Beck and H. Daniel. *Das Positronenspektrum von ^{22}Na und die Ruhemasse des Neutrinos aus dem β^+ - Zerfall.* Z. Phys. **A216**, 229–231 (1968).
- [Bec1997] D. Beck. *Massenbestimmung instabiler Isotope der Seltenen Erden um ^{146}Gd mit dem ISOLTRAP-Spektrometer.* PhD thesis, Johannes Gutenberg University, Mainz (1997).
- [Bec2002] D. Beck and H. Brand. *CS - A Control System Framework for Experiments at GSI.* Scientific report, Gesellschaft für Schwerionenforschung (2002).
- [Bec2004] D. Beck, K. Blaum, H. Brand, F. Herfurth, and S. Schwarz. *A new control system for ISOLTRAP.* Nucl. Instr. and Meth. **A527**, 567–579 (2004).
- [Bia1989] L. Bianchi, B. Fernandez, J. Gastebois, A. Gillibert, W. Mittig, and J. Barrette. *SPEG: An energy loss spectrometer for GANIL.* Nucl. Instr. and Meth. **A276**, 509–520 (1989).
-

-
- [Bis2003] S. Bishop, R. E. Azuma, L. Buchmann, A. A. Chen, M. L. Chatterjee, J. M. D’Auria, S. Engel, D. Gigliotti, U. Greife, M. Hernanz, D. Hunter, A. Hussein, D. Hutcheon, C. Jewett, J. José, J. King, S. Kubono, A. M. Laird, M. Lamey, R. Lewis, W. Liu, S. Michimasa, A. Olin, D. Ottewell, P. D. Parker, J. G. Rogers, F. Strieder, and C. Wrede. $^{22}\text{Na}(p,\gamma)^{22}\text{Mg}$ reaction and oxygen-neon novae. *Phys. Rev. Lett.* **90**, 162501 (2003).
- [BjØ1986] T. Bjørnstad, E. Hagebø, P. Hoff, O. C. Jonsson, E. Kugler, H. L. Ravn, S. Sundell, B. Vosicki, and the ISOLDE Collaboration. *Methods for production of intense beams of unstable nuclei: new developments at ISOLDE*. *Phys. Scrip.* **34**, 578–590 (1986).
- [Bla2002] K. Blaum, G. Bollen, F. Herfurth, A. Kellerbauer, H.-J. Kluge, M. Kuckein, E. Sauvan, C. Scheidenberger, and L. Schweikhard. *Carbon clusters for absolute mass measurements at ISOLTRAP*. *Eur. Phys. J.* **A15**, 245–248 (2002).
- [Bla2003a] K. Blaum, G. Audi, D. Beck, G. Bollen, F. Herfurth, A. Kellerbauer, H.-J. Kluge, E. Sauvan, and S. Schwarz. *Masses of ^{32}Ar and ^{33}Ar for fundamental tests*. *Phys. Rev. Lett.* **91**, 260801 (2003).
- [Bla2003b] K. Blaum, G. Bollen, F. Herfurth, A. Kellerbauer, H.-J. Kluge, M. Kuckein, S. Heinz, P. Schmidt, and L. Schweikhard. *Recent developments at ISOLTRAP: towards a relative mass accuracy of exotic nuclei below 10^{-8}* . *J. Phys.* **B36**, 921–930 (2003).
- [Bla2003c] K. Blaum, C. Geppert, H.-J. Kluge, M. Mukherjee, S. Schwarz, and K. Wendt. *A novel scheme for a highly selective laser ion source*. *Nucl. Instr. and Meth.* **B204**, 331–335 (2003).
- [Bla2004] K. Blaum, D. Beck, G. Bollen, P. Delahaye, C. Guénaut, F. Herfurth, A. Kellerbauer, H.-J. Kluge, D. Lunney, S. Schwarz, L. Schweikhard, and C. Yazidjian. *Population inversion of nuclear states by a Penning trap mass spectrometer*. *Europhys. Lett.* **67**, 586–592 (2004).
- [Blo1953] F. Bloch. *Experiments on the g-factor of the electron*. *Physica* **19**, 821–831 (1953).
- [Bol1990] G. Bollen, R. B. Moore, G. Savard, and H. Stolzenberg. *The accuracy of heavy-ion mass measurements using time of flight-ion cyclotron resonance in a Penning trap*. *Journal of Applied Physics* **68**, 4355–4374 (1990).
- [Bol1992a] G. Bollen, H. Hartmann, H.-J. Kluge, M. König, T. Otto, G. Savard, and H. Stolzenberg. *Towards a “perfect” Penning trap mass spectrometer for unstable isotopes*. *Phys. Scrip.* **46**, 581–586 (1992).
-

- [Bol1992b] G. Bollen, H.-J. Kluge, M. König, T. Otto, G. Savard, H. Stolzenberg, R. B. Moore, G. Rouleau, G. Audi, and ISOLDE collaboration. *Resolution of nuclear ground and isomeric states by a Penning trap mass spectrometer*. Phys. Rev. **C46**, R2140–R2143 (1992).
- [Bol1996] G. Bollen, S. Becker, H.-J. Kluge, M. König, R. B. Moore, T. Otto, H. Raimbault-Hartmann, G. Savard, L. Schweikhard, H. Stolzenberg, and the ISOLDE collaboration. *ISOLTRAP: a tandem Penning trap system for accurate on-line mass determination of short-lived isotopes*. Nucl. Instr. and Meth. **A368**, 675–697 (1996).
- [Bol2001] G. Bollen. *Mass measurements of short-lived nuclides with ion traps*. Nucl. Phys. **A693**, 3–18 (2001).
- [Bra1970] S. Brandt. *Statistical and computational methods in data analysis*. North Holland, Amsterdam (1970).
- [Bro1986] L. S. Brown and G. Gabrielse. *Geonium theory: Physics of a single electron or ion in a Penning trap*. Review of Modern Physics **58**, 233–311 (1986).
- [Brü2005] K. Brück. PhD thesis, Johannes Gutenberg University, Mainz (2005), in preparation.
- [Buc1993] M. V. Buchanan and R. L. Hettlich. *Fourier transform mass spectrometry of high-mass biomolecules*. Anal. Chem. **65**, 245A (1993).
- [Cab1963] N. Cabibbo. *Unitary symmetry and leptonic decays*. Phys. Rev. Lett. **10**, 531–533 (1963).
- [Cha1998] M. Chartier et al. *The masses of $^{70,71}\text{Se}$* . Nucl. Phys. **A637**, 3–14 (1998).
- [Cir2002] V. Cirigliano, M. Knecht, H. Neufeld, H. Rupertsberger, and P. Talavera. *Radiative corrections to K_{13} decays*. Eur. Phys. J. **C23**, 121–133 (2002).
- [Cir2004] V. Cirigliano, H. Neufeld, and H. Pichl. *K_{e3} decays and CKM unitarity*. Eur. Phys. J. **C35**, 53–65 (2004).
- [Cla1974] D. D. Clayton and F. Hoyle. *Gamma-ray lines from novae*. Astrophys. J. **187**, L101–103 (1974).
- [Cor1989] E. A. Cornell, R. M. Weisskoff, K. R. Boyce, Jr. R. W. Flanagan, G. P. Lafyatis, and D. E. Pritchard. *Single-ion cyclotron resonance measurement of $M(\text{CO}^+)/M(\text{N}_2^+)$* . Phys. Rev. Lett. **63**, 1674–1677 (1989).
- [Dah2000] D. A. Dahl (2000), SIMION 3D 7.0, Laplace equation solver software, Idaho National Engineering Laboratory.
-

- [Dav1992] C. N. Davids, B. B. Back, K. Bindra, D. J. Henderson, W. Kutschera, T. Lauritsen, Y. Nagame, P. Sugathan, A. V. Ramayya, and W. B. Walters. *startup of the Fragment Mass Analyzer at ATLAS*. Nucl. Instr. and Meth. **70**, 358–365 (1992).
- [Daw1995] P.H. Dawson. *Quadrupole Mass Spectrometry and its applications*. Elsevier, Amsterdam (1995).
- [Deh1967] H. G. Dehmelt. *Radiofrequency spectroscopy of stored ions I. Storage*. Adv. At. Mol. Phys. **3**, 53–72 (1967).
- [Den1997] P. Dendooven. *The development and status of the IGISOL technique*. Nucl. Instr. and Meth. **B126**, 182–189 (1997).
- [Dyc1989] Jr. R. S. Van Dyck, F. L. Moore, D. L. Farnham, and P. B. Schwinberg. *Number dependency in the compensated Penning trap*. Phys. Rev. **A40**, 6308–6313 (1989).
- [Dyc1992] Jr. R. S. Van Dyck, D. L. Farnham, and P. B. Schwinberg. J. Mod. Optics **39**, 243 (1992).
- [Dyc1993] Jr. R. S. Van Dyck, D. L. Farnham, and P. B. Schwinberg. *Tritium-Helium-3 mass difference using the Penning trap mass spectroscopy*. Phys. Rev. Lett. **19**, 2888–2891 (1993).
- [Ead1971] W. T. Eadie, D. Drijard, F. E. James, M. Roos, and B. Sadoulet. *Statistical methods in experimental physics*. North Holland, Amsterdam (1971).
- [Ell1978] H. W. Ellis, E. W. McDaniel, D. L. Albritton, L. A. Viehland, S. L. Lin, and E. A. Mason. *Transport properties of gaseous ions over a wide energy range Part II*. Atomic Data and Nucl. Data Tables **22**, 197–217 (1978).
- [Emm1993] J. Emmes. *Präzisionsmassenspektrometrie in der Penningfalle*. Diplomarbeit, Johannes Gutenberg University, Mainz (1993).
- [End1990] P. M. Endt. *Energy levels of $A = 21 - 44$ nuclei (VII)*. Nucl. Phys. **A521**, 1–400 (1990).
- [Fow1967] W. A. Fowler, G. R. Caughlan, and B. A. Zimmerman. *Thermonuclear reaction rates*. Ann. Rev. Astron. Astrophys. **5**, 525–570 (1967).
- [Gab1990] G. Gabrielse, X. Fei, L. A. Orozco, R. L. Tjoelker, J. Hass, H. Kalinowsky, T. A. Trainor, and W. Kells. *Thousand fold improvement in the measured antiproton mass*. Phys. Rev. Lett. **65**, 1317–1320 (1990).
-

- [Gab1993] G. Gabrielse, W. Jhe, D. Phillips, W. Quint, L. Haarsma, K. Abdullah, H. Kalinowsky, and J. Gröbner. *A single trapped antiproton and antiprotons for antihydrogen production*. Hyperfine Interactions **81**, 5–14 (1993).
- [Gei1992] H. Geissel et al. *The GSI projectile fragment separator (FRS): a versatile magnetic system for relativistic heavy ions*. Nucl. Instr. and Meth. **B70**, 286–297 (1992).
- [Gei2001] H. Geissel, F. Attallah, K. Beckert, F. Bosch, M. Falch, B. Franzke, M. Hausmann, Th. Kerscher, O. Klepper, H.-J. Kluge, C. Kozhuharov, Yu. Litvinov, K. E. G. Löbner, G. Münzenberg, N. Nankov, F. Nolden, Yu. Novikov, T. Ohtsubo, Z. Patyk, T. Radon, C. Scheidenberger, J. Stadlmann, M. Steck, K. Sümmerer, H. Weick, and H. Wollnik. *Progress in mass measurements of stored exotic nuclei at relativistic energies*. Nucl. Phys. **A685**, 115c–126c (2001).
- [Ger1990] Ch. Gerz, D. Wilsdorf, and G. Werth. *Measurement of the $^4\text{He} - D_2$ mass difference*. Z. Phys. **D17**, 119–121 (1990).
- [Gho1995] P. K. Ghosh. *Ion traps*. Oxford University Press, New York (1995).
- [Gil1972] H. J. Gils, D. Flothmann, R. Löhken, and W. Wiesner. *A 4π $\beta - \gamma$ coincidence spectrometer using $\text{Si}(\text{Li})$ and $\text{NaI}(\text{Tl})$ detectors*. Nucl. Instr. and Meth. **105**, 179–188 (1972).
- [Grä1980] G. Gräff, H. Kalinowsky, and J. Traut. *A direct determination of the proton electron mass ratio*. Z. Phys. **A297**, 35–39 (1980).
- [Gué2004] C. Guénaut. PhD thesis, University of Orsay, France (2004), in preparation.
- [Hag1991] D. Hagen and G. Werth. *Measurement of the $^3\text{He}^+/\text{H}_2^+$ mass ratio*. Europhys. Lett. **15**, 491–495 (1991).
- [Hag2002] K. Hagiwara et al. *Review of particle physics*. Phys. Rev. **D66** (2002).
- [Har1974] J. C. Hardy, H. Schmeing, W. Benenson, G. M. Crawley, E. Kashy, and H. Nann. *Fermi beta decay: The masses of ^{22}Mg , ^{26}Si , ^{30}S , and ^{34}Ar* . Phys. Rev. **C9**, 252–257 (1974).
- [Har2003] J. C. Hardy, V. E. Iacob, M. Sanchez-Vega, R. G. Neilson, A. Azhari, C. A. Gagliardi, V. E. Mayes, X. Tang, L. Trache, and R. E. Tribble. *High precision measurement of the superallowed $0^+ \rightarrow 0^+ \beta$ decay of ^{22}Mg* . Phys. Rev. Lett. **91**, 082501 (2003).
- [Hau2001] M. Hausmann, J. Stadlmann, F. Attallah, K. Beckert, P. Beller, F. Bosch, H. Eickhoff, M. Falch, B. Franczak, B. Franzke, H. Geissel, Th. Kerscher, O. Klepper, H.-J. Kluge, C. Kozhuharov, Yu. A.
-

- Litvinov, K. E. G. Löbner, G. Münzenberg, N. Nankov, F. Nolden, Yu. N. Novikov, T. Ohtsubo, T. Radon, H. Schatz, C. Scheidenberger, M. Steck, Z. Sun, H. Weick, and H. Wollnik. *Isochronous mass measurements of hot exotic nuclei*. Hyperfine Interactions **132**, 291–297 (2001).
- [Her2001] F. Herfurth, J. Dilling, A. Kellerbauer, G. Bollen, S. Henry, H.-J. Kluge, E. Lamour, D. Lunney, R.B. Moore, C. Scheidenberger, S. Schwarz, G. Sikler, and J. Szerypo. *A linear radiofrequency ion trap for accumulation, bunching and emittance improvement of radioactive ion beams*. Nucl. Instr. and Meth. **A469**, 254–275 (2001).
- [Her2004] A. Herlert, B. Beck, K. Blaum, F. Carrel, P. Delahaye, S. George, C. Guénaut, F. Herfurth, A. Kellerbauer, H.-J. Kluge, D. Lunney, M. Mukherjee, L. Schweikhard, and C. Yazidjian. to be submitted to New J. Phys. (2004).
- [Hip1949] J. A. Hipple, H. Sommer, and H. A. Thomas. *A precise method of determining the Faraday by magnetic resonance*. Phys. Rev. **76**, 1877–1878 (1949).
- [Hof2000] S. Hofmann and G. Münzenberg. *The discovery of the heaviest elements*. Review of Modern Physics **72-3**, 733–767 (2000).
- [Hur1988] G. H. Hurst and M. G. Payne. *Principles and applications of resonance ionisation spectroscopy*. Adam Hilger, Bristol (1988).
- [Ich2003] S. Ichikawa, A. Osa, M. Matsuda, K. Tsukada, M. Asai, Y. Ngame, S. C. Jeong, and I. Katayama. *Ion source development for the JAERI on-line isotope separator*. Nucl. Instr. and Meth. **B204**, 372–376 (2003).
- [Jea2001] P. Jean et al. *REXTRAP, an ion buncher for REX-ISOLDE*. In *Proc. of the Fourth INTEGRAL Workshop*, volume SP-459, page 73 (2001).
- [Jef1983] J. B. Jeffries, S. E. Barlow, and G. H. Dunn. *Theory of space-charge shift of ion cyclotron resonance frequencies*. Int. J. Mass Spectrom. Ion Process **54**, 169–187 (1983).
- [Jhe1992] W. Jhe, D. Phillips, L. Haarsma, J. Tan, and G. Gabrielse. *Cylindrical Penning traps and self-shielding superconducting solenoids for high precision experiments*. Phys. Scrip. **46**, 264–267 (1992).
- [Jos1999] J. José, A. Coc, and M. Hernanz. *Nuclear uncertainties in the NeNa-MgAl cycles and production of ^{22}Na and ^{26}Al during nova outbursts*. Astrophys. J. **520**, 347–360 (1999).
-

- [Jun1987] K. Jungmann, J. Hoffnagel, R. G. DeVoe, and R. G. Brewer. *Collective oscillations of stored ions*. Phys. Rev. **A36**, 3451–3454 (1987).
- [Kap1965] P. L. Kapitza. *Collected Papers of P. L. Kapitza, Volume II, 1938-1964 chapter 45*. Pergamon Press Ltd. (1965).
- [Kel2002] A. Kellerbauer, G. Bollen, J. Dilling, S. Henry, F. Herfurth, H.-J. Kluge, E. Lamour, R.B. Moore, C. Scheidenberger, S. Schwarz, G. Sikler, and J. Szerypo. *A linear radiofrequency quadrupole ion trap for the cooling and bunching of radioactive ion beams*. Nucl. Phys. **A701**, 565c–569c (2002).
- [Kel2003] A. Kellerbauer, K. Blaum, G. Bollen, F. Herfurth, H.-J. Kluge, M. Kuckein, E. Sauvan, C. Scheidenberger, and L. Schweikhard. *From direct to absolute mass measurements: A study of the accuracy of ISOLTRAP*. Eur. Phys. J. **D22**, 53–64 (2003).
- [Kel2004] A. Kellerbauer, G. Audi, D. Beck, K. Blaum, G. Bollen, B. A. Brown, P. Delahaye, C. Guénaut, F. Herfurth, H.-J. Kluge, D. Lunney, S. Schwarz, L. Schweikhard, and C. Yazidjian. *Direct mass measurement on the superallowed emitter ^{74}Rb and its daughter ^{74}Kr : Isospin-symmetry-breaking correction for standard-model tests*. Phys. Rev. Lett. **93**, 072502 (2004).
- [Ken1951] Kenney and Keeping. *Mathematics of statistics*. Van Nostrand, Princeton, New York, Toronto, London (1951).
- [Kim1997] T. Kim. *Buffer gas cooling of ions in an RF ion guide: A study of the cooling process and cooled beam properties*. PhD thesis, McGill University, Montreal, Canada (1997).
- [Kir2003] R. Kirchner. *Review of ISOL Target-ion-source systems*. Nucl. Instr. and Meth. **B204**, 179–190 (2003).
- [Klu1985] H.-J. Kluge, F. Ames, W. Ruster, and K. Wallmeroth. *Laser ion sources*. In *Proc. Accelerated Radioactive Beams Workshop, TRIUMF 85-1*, pages 119–128 (1985).
- [Kob1973] M. Kobayashi and T. Maskawa. *CP-violation in the renormalizable theory of weak interaction*. Prog. Theor. Phys. **49**, 652–657 (1973).
- [Kön1995a] M. König. *Präzisionsmassenbestimmung instabiler Cäsium- und Bariumisotope in einer Penningfalle und Untersuchung der Ionenbewegung bei azimuthaler Quadrupolanregung*. PhD thesis, Johannes Gutenberg University, Mainz (1995).
- [Kön1995b] M. König, G. Bollen, H.-J. Kluge, T. Otto, and J. Szerypo. *Quadrupole excitation of stored ion motion at the true cyclotron frequency*. Int. J. Mass Spectrom. Ion Process **142**, 95–116 (1995).
-

-
- [Kös2003] U. Köster et al. *On-line yields obtained with the ISOLDE RILIS*. Nucl. Instr. and Meth. **B204**, 347–352 (2003).
- [Kre1991] M. Kretschmar. *Particle motion in a Penning trap*. Eur. J. Phys. **12**, 240–248 (1991).
- [Kub1992] T. Kubo, M. Ishihara, N. Inabe, H. Kumagai, I. Tanihata, and K. Yoshida. *The RIKEN radioactive beam facility*. Nucl. Instr. and Meth. **B70**, 309–319 (1992).
- [Kug2000] E. Kugler. *The ISOLDE facility*. Hyperfine Interactions **129**, 23–42 (2000).
- [Let1987] V. S. Letokov. *Laser photoionization spectroscopy*. Academic Press, Orlando (1987).
- [Lin1961] Y. V. Linnik. *Method of least squares*. Pergamon, New York (1961).
- [Lun2001] D. Lunney, G. Audi, H. Doubre, S. Henry, C. Monsanglant, M. de Saint Simon, C. Thibault, C. Toader, C. Borcea, G. Bollen, and the ISOLDE Collaboration. *Precision mass measurements of very short-lived, neutron-rich Na isotopes using a radio-frequency spectrometer*. Phys. Rev. **C64**, 054311 (2001).
- [Lun2003] D. Lunney, J. M. Pearson, and C. Thibault. *Recent trends in the determination of nuclear masses*. Review of Modern Physics **75** (2003).
- [Mar1967] L. Marton. *Methods of experimental Physics: Atomic sources and detectors*. Academic Press (1967).
- [McD1973] E. W. McDaniel and E. W. Mason. *The mobility and diffusion of ions in gases*. Wiley (1973).
- [Mor2003a] K. Morita et al. *Study of decays of $^{127}110$ and $^{272}111$ produced with $^{208}\text{Pb}(^{64}\text{Ni},n)$ and $^{209}\text{Bi}(^{64}\text{Ni},n)$ reactions*. In *Tours Symposium on Nuclear Physics V, Tours*, pages 13–20 (2003).
- [Mor2003b] D. J. Morrissey, B. M. Sherrill, M. Steiner, A. Stolz, and I. Wiedenhofer. *Commissioning the A1900 projectile fragment separator*. Nucl. Instr. and Meth. **B204**, 90–96 (2003).
- [Muk2004] M. Mukherjee, A. Kellerbauer, D. Beck, K. Blaum, G. Bollen, F. Carrel, P. Delahaye, J. Dilling, S. George, C. Guénaut, F. Herfurth, A. Herlert, H.-J. Kluge, U. Köster, D. Lunney, S. Schwarz, L. Schweikhard, and C. Yazidjian. *The mass of ^{22}Mg* . Phys. Rev. Lett. **93**, 150801 (2004).
- [Mün1992] G. Münzenberg. *The separation techniques for secondary beams*. Nucl. Instr. and Meth. **B70**, 265–275 (1992).
-

- [Nie2001] A. Nieminen, J. Huikari, A. Jokinen, J. Äystö, P. Campbell, and E. C. A. Cochrane. *Beam cooler for low-energy radioactive ions*. Nucl. Instr. and Meth. **A469**, 244–253 (2001).
- [Nol1974] J. A. Nolen, Jr. G. Hamilton, E. Kashy, and I. D. Proctor. *Measuring nuclear excitation energies and Q -values with a cyclotron-magnetic spectrograph system*. Nucl. Instr. and Meth. **115**, 189–196 (1974).
- [Org2004] Yu. Ts. Organessian et al. *Experiments on the synthesis of element 115 in the reaction $^{243}\text{Am}(^{48}\text{Ca},xn)^{291-x}115$* . Phys. Rev. **C69**, 021601 (2004).
- [Orm1995] W. E. Ormand and B. A. Brown. *Isospin-mixing corrections for fp -shell Fermi transitions*. Phys. Rev. **C52**, 2455–2459 (1995).
- [Pau1953] W. Paul and H. Steinwedel. *Ein neues Massenspektrometer ohne Magnetfeld*. Z. Naturforschung **8a**, 448–450 (1953).
- [Pau1989] W. Paul. *Electromagnetic traps for charged and neutral particles*. Review of Modern Physics **62**, 531–540 (1989).
- [Rad1997] T. Radon, Th. Kerscher, B. Schlitt, K. Beckert, T. Beha, F. Bosch, H. Eickhoff, B. Franzke, Y. Fujita, H. Geissel, M. Hausmann, H. Irnich, H. C. Jung, O. Klepper, H.-J. Kluge, C. Kozhuharov, G. Kraus, K. E. G. Löbner, G. Münzenberg, Yu. Novikov, F. Nickel, F. Nolden, Z. Patyk, H. Reich, C. Scheidenberger, W. Schwab, M. Steck, K. Sümmerer, and H. Wollnik. *Schottky mass measurements of cooled proton-rich nuclei at the GSI experimental storage ring*. Phys. Rev. Lett. **78**, 4701–4704 (1997).
- [Rau2004] C. Rauth, C. Geppert, R. Horn, J. Lassen, P. Bricault, and K. Wendt. *First laser ions at an off-line mass separator of the ISAC facility at TRIUMF*. Nucl. Instr. and Meth. **B215**, 268–277 (2004).
- [RH1997] H. Raimbault-Hartmann, D. Beck, G. Bollen, M. König, H.-J. Kluge, E. Schark, J. Stein, S. Schwarz, and J. Szerypo. *A cylindrical Penning trap for capture, mass selective cooling, and bunching of radioactive ion beams*. Nucl. Instr. and Meth. **B126**, 387–382 (1997).
- [Roo2004] J. Van Roosbroeck, C. Guénaut, G. Audi, D. Beck, K. Blaum, G. Bollen, J. Cederkall, P. Delahaye, A. De Maesschalck, H. De Witte, D. Fedorov, V. N. Fedoseyev, S. Franchoo, H. O. U. Fynbo, M. Gorska, F. Herfurth, K. Heyde, M. Huyse, A. Kellerbauer, H.-J. Kluge, U. Köster, K. Kruglov, D. Lunney, V. I. Mishin, W. F. Mueller, Sz. Nagy, S. Schwarz, L. Schweikhard, N. A. Smirnova, K. Van de Vel, P. Van Duppen, A. Van Dyck, W. B. Walters, L. Weissman, and C. Yazidjian. *Unambiguous identification of three β -decaying isomers in ^{70}Cu* . Phys. Rev. Lett. **92**, 11250 (2004).
-

-
- [Sar2000] F. Sarazin, H. Savajols, W. Mittig, F. Nowacki, N. A. Orr, Z. Ren, P. Roussel-Chomaz, G. Auger, D. Baiborodin, A. V. Belozyorov, C. Borcea, E. Caurier, Z. Dlouhý, A. Gillibert, A. S. Lalleman, M. Lewitowicz, S. M. Lukyanov, F. de Oliveira, Y. E. Penionzhkevich, D. Ridikas, H. Sakurai, O. Tarasov, and A. de Vismes. *Shape co-existence and the $N=28$ shell closure far from stability*. Phys. Rev. Lett. **84**, 5062–5065 (2000).
- [Sav1991] G. Savard, St. Becker, G. Bollen, H.-J. Kluge, R. B. Moore, Th. Otto, L. Schweikhard, H. Stolzenberg, and U. Wiess. *A new cooling technique for heavy ions in a Penning trap*. Phys. Lett. **A158**, 247–252 (1991).
- [Sav2004] G. Savard, J. A. Clark, F. Buchinger, J. E. Crawford, S. Gulick, J. C. Hardy, A. A. Hecht, V. E. Jacob, J. K. P. Lee, A. F. Levand, B. F. Lundgren, N. D. Scielzo, K. S. Sharma, I. Tanihata, I. S. Towner, W. Trimble, J. C. Wang, and Z. Zhou. *Q -value of the superallowed decay of ^{22}Mg and the calibration of the $^{21}\text{Na}(p,\gamma)$ experiment*. Phys. Rev. **C** (2004), in print.
- [Sch1981] P. B. Schwinberg, Jr. R. S. Van Dyck, and H. G. Dehmelt. *Trapping and thermalization of positrons for Geonium spectroscopy*. Phys. Lett. **A81**, 119–120 (1981).
- [Sch1999] S. Schwarz. *Manipulation radioaktiver Ionenstrahlen mit Hilfe einer Paulfalle und direkte Massenmessungen an neutronenarmen Quecksilberisotopen mit dem ISOLTRAP-Experiment*. PhD thesis, Johannes Gutenberg University, Mainz (1999), ISBN 3-8288-0735-6.
- [Sch2002] C. Scheidenberger, G. Bollen, F. Herfurth, A. Kellerbauer, H.-J. Kluge, M. Koizumi, S. Schwarz, and L. Schweikhard. *Production and trapping of carbon clusters for absolute mass measurements at ISOLTRAP*. Nucl. Phys. **A701**, 574c–578c (2002).
- [Sch2004a] S. Schwarz (2004), Michigan State University, private communication.
- [Sch2004b] L. Schweikhard, K. Blaum, A. Herlert, and G. Marx. *Atomic clusters and ion cyclotron resonance mass spectrometry - a fruitful combination*. Eur. J. Mass Spectrom. (2004), submitted.
- [Sci2003] B. Sciascia and the KLOE collaboration. *KLOE prospects and preliminary results for K_{13} decay measurements*. In P. Ball, J. Flynn, P. Kluit, and A. Stocchi (eds.), *Workshop on the CKM unitarity triangle Second meeting, IPPP Durham*, volume eConf C0304052, page WG607 (2003).
-

- [Sha1991] K. S. Sharma, E. Hagberg, G. R. Dyck, J. C. Hardy, V. T. Koslowsky, H. Schmeing, R. C. Barber, S. Yuan, W. Perry, and M. Watson. *Masses of $^{103,104,105}\text{In}$ and $^{72,73}\text{Br}$* . Phys. Rev. **C44**, 2439–2444 (1991).
- [She2003] A. Sher et al. *High statistics measurement of the $K^+ \rightarrow \pi^0 e^+ \nu(K_{e3}^+)$ branching ratio*. Phys. Rev. Lett. **91**, 261802 (2003).
- [Shr1978] R. E. Shrock and Ling-L. Wang. *New, generalized Cabibbo fit and application to quark mixing angles in the sequential Weinberg-Salam model*. Phys. Rev. Lett. **41**, 1692–1695 (1978).
- [Smi2000] N. A. Smirnova and A. Coc. *$^{21}\text{Na}(p, \gamma)^{22}\text{Mg}$ thermonuclear rate for ^{22}Na production in novae*. Phys. Rev. **C62**, 0458031–0458035 (2000).
- [Thi1975] C. Thibault, R. Klapisch, C. Rigaud, A. M. Poskanzer, R. Prieels, L. Lessard, and W. Reisdorf. *Direct measurement of the masses of ^{11}Li and $^{26-32}\text{Na}$ with an on-line mass separator*. Phys. Rev. **C12**, 644–657 (1975).
- [Tow2002] I. S. Towner and J. C. Hardy. *Calculated corrections to superallowed Fermi β decay: new evaluation of the nuclear-structure-dependent terms*. Phys. Rev. **C66**, 035501 (2002).
- [Tow2003] I. S. Towner and J. C. Hardy. *The evaluation of V_{ud} , experiment and theory*. J. Phys. **G29**, 197–211 (2003).
- [Tow2004] I. S. Towner and J. C. Hardy (2004), TRIUMF Vancouver, private communication.
- [Vie1986] D. J. Vieira, J. M. Wouters, K. Vaziri, R. H. Kraus, H. Wollnik, G. W. Butler, F. K. Wohn, and A. H. Wapstra. *Direct measurement of neutron-rich light nuclei near $N = 20$* . Phys. Rev. Lett. **57**, 3253–3256 (1986).
- [Wap2003] A. H. Wapstra, G. Audi, and C. Thibault. *The 2003 atomic mass evaluation*. Nucl. Phys. **A729**, 129–337 (2003).
- [Wen2002] K. Wendt (2002), Johannes Gutenberg University, private communication.
- [Wen2003] F. Wenander, J. Lettry, and M. Lindroos. *Transverse emittance investigation of the ISOLDE target-ion sources*. Nucl. Instr. and Meth. **B204**, 261–266 (2003).
- [Wen2004] K. Wendt, K. Blaum, K. Brück, Ch. Geppert, H.-J. Kluge, M. Mukherjee, G. Passler, S. Schwarz, S. Sirotzky, and K. Wies. *A highly selective laser ion source for bunched, low emittance beam release*. Nucl. Phys. **A** (2004), in print.
-

- [Wie1986a] M. Wiescher, J. Görres, F.-K. Thielemann, and H. Ritter. *Explosive hydrogen burning in novae*. *Astron. Astrophys.* **160**, 56–72 (1986).
- [Wie1986b] M. Wiescher and K. Langanke. *The proton capture reactions on ^{21}Na and ^{22}Na under hydrogen burning conditions*. *Z. Phys.* **A325**, 309–315 (1986).
- [Wie2004] K. Wies. PhD thesis, Johannes Gutenberg University, Mainz (2004), in preparation.
- [Win1975] D. J. Wineland and H. G. Dehmelt. *Principles of the stored ion calorimeter*. *Journal of Applied Physics* **46**, 919–930 (1975).
- [Wou1987] J. M. Wouters, D. J. Vieira, H. Wollnik, G. W. Butler, Jr. R. H. Kraus, and K. Vaziri. *The Time-Of-Flight Isochronous (TOFI) spectrometer for direct mass measurements of exotic light nuclei*. *Nucl. Instr. and Meth.* **B26**, 286–293 (1987).
- [Wou1988] J. M. Wouters, R. H. Kraus, D. J. Vieira, G. W. Butler, and K. E. G. Löbner. *Direct mass-measurements of the neutron-rich light isotopes of Lithium through Fluorine*. *Z. Phys.* **A331**, 229–233 (1988).
- [Yaz2004] C. Yazidjian. PhD thesis, University of Caen, France (2004), in preparation.
-

Acknowledgement

My first and foremost gratitude goes to my supervisor Prof. H.-J.Kluge for his scientific, financial, and moral support all along the course of this work. It is he who opened the opportunity to work and know more than one experiment, namely the SHIPTRAP at GSI, the ISOLTRAP at CERN, and the LIST at Mainz. Though geographically they are far apart but trap techniques provided common ground as well as opened further prospects for trap assisted technical developments to come.

I am thankful to Prof. B. P. Das for introducing me to the field of ion trapping and its applicability to fundamental physics studies.

I would like to specially thank K. Blaum for his unconditional support starting from the LIST collaboration until the proof reading of the thesis. He made himself always available whenever needed which made things moving smooth and fast.

Behind a successful work lies a vibrant team. So is the case of ISOLTRAP as well as SHIPTRAP. I am thankful to my former colleagues G. Marx, D. Rodríguez, G. Sikler, and C. Weber at SHIPTRAP for providing a friendly and exciting working atmosphere which is being efficiently carried along till date by present colleagues M. Block, A. Chaudhuri, S. Rahaman, C. Rauth, and W. Quint. I am happy to be a part of the big SHIPTRAP collaboration, which is composed of people with diverse professional expertise.

To be thankful may be not enough to convey my gratitude towards the ISOLTRAP team which has been the front runner in the world in high precision mass measurements on short-live radioactive ions since mid-90's. I am grateful to be a part and contributor to the development of that group presently comprising of K. Blaum, A. Herlert, C. Yazidjian and many other collaborators who form the large ISOLTRAP collaboration.

It has been my pleasure to work with F. Herfurth on many different occasions namely, the cluster source and transfer section design, the mass evaluation, and finally partial proof reading. With respect to the data evaluation, I would like to thank Y. Lutvinov and C. Kozhuharov for many fruitful discussions. I. S. Towner and J. C. Hardy deserves special mention for calculating the statistical rate factor f for our measurement on the superallowed β -decay of ^{22}Mg . I am thankful to A. Kellerbauer for having communicated with I. S. Towner in this regard. It is my pleasure to convey my gratitude to M. Block, also for partial proof reading of the thesis.

Though life outside the experiment was very little for the last three years, but nevertheless it was enjoyable vastly due to unforgettable friendship that I have. To mention only a few names are my "makarash" teammates, T. Beier, R. Palit, S. Mandal, U. D. Paramanik, S. Chatterjee, and lately A. Chaudhari. I am specially grateful to the friendship that I had with Adriana from whom I learnt more about the alien culture (for me).

I am sorry for not mentioned all the names explicitly who have made the work a success. In particular, I would like to show my gratitude towards the GSI workshop, the technology laboratory, the ion source group, and the target laboratory for fulfilling all my demands quoted - “needed yesterday”.

Last in order but first in preference is my gratitude towards my parents and sister’s family who despite large distance kept comforting all the time and wishing for my success. I dedicate this work to them.